

Siren Grasmo

# Effect of Surface Treatment and Preheating Temperature on Compound Casting of Aluminium Alloy A356 onto 6060 Inserts

Master's thesis in Chemical Engineering and Biotechnology

Supervisor: Yanjun Li, Aina Opsal Bakke

June 2019



Siren Grasmø

# Effect of Surface Treatment and Preheating Temperature on Compound Casting of Aluminium Alloy A356 onto 6060 Inserts

Master's thesis in Chemical Engineering and Biotechnology  
Supervisor: Yanjun Li, Aina Opsal Bakke  
June 2019

Norwegian University of Science and Technology  
Faculty of Natural Sciences  
Department of Materials Science and Engineering

 **NTNU**  
Norwegian University of  
Science and Technology



## Abstract

Reduction of vehicle weight is an important field of study for the automotive industry, as this would decrease fuel consumption and result in both economic and environmental benefits.

Compound casting is the casting of a liquid material onto a solid structure of another. By casting a light-metal onto a stronger structure, the required strength of a component could be achieved while reducing the overall weight. Aluminium is a well-suited metal used in the automotive industry, but the natural oxide layer is a challenge during compound casting. Wettability of aluminium on  $\text{Al}_2\text{O}_3$  is poor, and the formation of a reaction zone between the insert and cast aluminium is inhibited by the oxide layer.

In this thesis, the aluminium alloys A356 and 6060 were joined through a compound casting process. The effects of preheating temperatures and zincate treatment on the inserts were studied separately in three experiments. Experiment 1 tested if bonding could be achieved with zinc coated inserts. Experiment 2 studied the effect of preheating either the insert or mould on the formation of gaps between the insert and cast aluminium. Experiment 3 tested whether high preheating temperatures for the insert and mould could result in bonding. Both pipes and rods used as inserts. The interface structure of all the compound casting samples were characterised by study in a scanning electron microscope. Stress simulations for the compound cast parts were performed with the software StaMiSim.

In the first experiment, mould filling and solidification was simulated in SutCast to decide preheating temperatures prior to casting. A zinc layer was applied to the inserts by different coating procedures to get different thicknesses. The quality of the zinc layer was not high enough to prevent reoxidation of the aluminium surface. Zinc was detected as a diffusion layer in 6060 by EDS analysis, and bonding was not achieved. The application process of the zinc layer should be further improved before the effect of the thickness can be studied.

For the second experiment, preheating was done for either the insert or mould. One was kept at room temperature, while the other was preheated to  $600^\circ\text{C}$ . The intended temperature difference was reduced due to heat transfer as the insert was placed inside the mould. Similar areas of possible melting of the insert surface and cracks along the interface was observed in both series.

The third experiment was performed at high preheating temperatures, with rods or pipes as inserts. Despite no surface treatment of the inserts, successful bonding was achieved on the inside of the pipes. Along the rods and outside of the pipes, cracks formed along the interface or through eutectic silicon in the cast aluminium. This resulted in weak compound cast parts, despite bonding between A356 and 6060 being achieved.

## Sammendrag

For bilindustrien er det viktig å studere ulike metoder for å redusere kjøretøyvekt, da dette reduserer bensinforbruk, noe som vil ha både økonomiske og miljømessige fordeler.

Hybridstøpning er å støpe et flytende materiale på en fast overflate. Ved å støpe et lettvektig metall på en sterkere komponent, kan kravene til styrke bli overholdt, samtidig som den samlede vekten blir redusert. Aluminium er et velegnet metall for bildeler, men det naturlige oksidlaget på overfaten er en utfordring ved hybridstøpning. Overflatefukting av aluminium på  $\text{Al}_2\text{O}_3$  er dårlig, og diffunderingen hindres av oksidlaget.

I denne studien ble aluminiumlegeringen A356 forsøkt faststøpt på en innsats av 6060 ved hybridstøpning. I tre separate eksperimenter ble effekten av sinkbehandling på innsatsene samt forvarming av innsatsene og formen studert. Eksperiment 1 testet om sinkbehandling ville føre til sammenføyning. Eksperiment 2 undersøkte effekten av forvarming av enten innsatsen eller formen på sprekkdannelsen mellom innsatsen og støpelegeringen. Eksperiment 3 studerte om høy forvarming av innsats of form kunne resultere i sammenføyning. Innsatser formet som både staver og rør ble brukt. Alle prøvene ble studert gjennom et skanningelektronmikroskop, og simulering av spenningsfelt i prøvene ble utført med programvaren StaMiSim.

I det første eksperimentet ble fylling av støpeform og størkning simulert i SutCast før støpning for å fastsette formvarmingstemperaturene. Ulike metoder for påføring av sinklaget ble brukt for å få ulike tykkelser. Sinklaget hadde ikke god nok kvalitet til å forhindre reokidering av aluminiumsoverflaten. Sinken ble funnet som et diffusjonslag i 6060 ved EDS-analyse, og sammenføyning ble ikke oppnådd. Påføringsmetoden må forbedres for å kunne studere effekten av tykkelsen til sinklaget.

I det andre eksperimentet ble det variert om innsatsen eller støpeformen ble forvarmet. Den ene ble holdt på romtemperatur mens den andre ble forvarmet til  $600^\circ\text{C}$ . Den planlagte temperaturforskjellen ble redusert pga. varmeoverføring da innsatsen ble plassert i formen. Områder med mulig smelting av innsatsoverflaten og sprekker langs grensesjiktet ble observert i begge seriene.

Det tredje eksperimentet ble utført med høye forvarmingstemperaturer og med staver eller rør som innsatser. Selv uten overflatebehandling ble suksessfull binding oppnådd på innsiden av rørene. Langs stavene og utsiden av rørene ble det dannet sprekker langs grensesjiktene eller gjennom den eutektisk silisiumen i A356. Dette resulterte i en svak hybridstøpt del, til tross for at binding mellom A356 og 6060 ble oppnådd.

## Preface

First of all, I would like to thank my supervisor Aina Opsal Bakke, for invaluable help with all aspects of this thesis, and for being available anytime.

This thesis has been part of the "AluLean" project, a collaboration with Chassix Norway AS, the Institute for Energy Technology (IFE), the University of Agder (UiA) and SINTEF Materials and Chemistry in Trondheim. I would like to thank all members of the project, including; From Chassix, Jan Ove Løland, for bringing me into the AluLean project, and Reza Babaei, for teaching me and always helping me with SutCast; Dag Mortensen at IFE, for running simulations with StaMiSim; my supervisor Yanjun Li, for introducing me to casting and helping me improve my work.

I especially want to thank my dad, Geir Grasmø, for inspiration, support and guidance both academically and emotionally my entire life. My mom, Inger and sisters Line and Eirin, have always been supportive, and especially helped me through the final weeks. I want to thank my boyfriend, Petter Rostrup, for being there for me every day, and for all the food.

Surface treatment of the inserts was done by John Erik Lein at Sintef Materials and Chemistry in Trondheim. Lastly, I want to thank Yingda Yu at NTNU for help at the EM-lab.





# Contents

<b>Abstract</b>	<b>I</b>
<b>Sammendrag</b>	<b>II</b>
<b>Preface</b>	<b>III</b>
<b>List of Figures</b>	<b>VII</b>
<b>List of Tables</b>	<b>VIII</b>
<b>1 Introduction</b>	<b>1</b>
<b>2 Theory</b>	<b>3</b>
2.1 Compound Casting . . . . .	3
2.2 Metallurgical Bonding and Intermetallic Phases . . . . .	3
2.3 Wettability . . . . .	4
2.4 Material Properties . . . . .	4
2.4.1 A356 Alloy . . . . .	5
2.4.2 6060 Alloy . . . . .	6
2.4.3 The Oxide Layer . . . . .	6
2.5 Coating . . . . .	7
2.5.1 Zincate treatment . . . . .	7
2.6 Scanning Electron Microscopy . . . . .	8
2.6.1 Energy Dispersive X-ray Spectroscopy . . . . .	8
2.7 Simulation . . . . .	9
<b>3 Experimental</b>	<b>11</b>
3.1 Insert Preparation . . . . .	11
3.1.1 Zinc Coating . . . . .	11
3.2 Compound Casting . . . . .	12
3.3 SEM Sample Preparation . . . . .	13
3.4 Simulations . . . . .	14
<b>4 Results</b>	<b>15</b>
4.1 Zinc Coated Inserts . . . . .	15
4.2 Simulation in SutCast . . . . .	15
4.2.1 Zinc Layer Thickness . . . . .	16
4.2.2 Series 1-1: Zinc Treatment for 30 s without Applied Current . . . . .	17
4.2.3 Series 1-2: Zinc Treatment for 8 s with Applied Current . . . . .	20
4.2.4 Series 1-3: Zinc Treatment for 15 s with Applied Current . . . . .	24
4.3 Preheated Mould or Insert . . . . .	27
4.3.1 Series 2-1: Preheated Insert . . . . .	27
4.3.2 Series 2-2: Preheated Mould . . . . .	30
4.4 High Preheating Temperature . . . . .	34

4.4.1	Series 3-1: Pipe Inserts . . . . .	34
4.4.2	Series 3-2: Rod Inserts . . . . .	38
4.5	Simulation in StaMiSim . . . . .	41
<b>5</b>	<b>Discussion</b>	<b>43</b>
5.1	Effect of Zinc Coating . . . . .	43
5.2	Preheating of Mould or Insert . . . . .	45
5.3	Effect of High Temperature . . . . .	46
<b>6</b>	<b>Conclusions</b>	<b>49</b>
	<b>References</b>	<b>53</b>
	<b>Appendix A</b>	<b>55</b>
	<b>Appendix B</b>	<b>57</b>
	<b>Appendix C</b>	<b>77</b>
	<b>Appendix D</b>	<b>83</b>

## List of Figures

1	Illustration of the wetting angle. . . . .	4
2	Al-Si binary phase diagram. . . . .	6
3	Formation of characteristic x-ray. . . . .	9
4	Current and time for one cycle of the zincate treatment for parallel 2 and 3. . . . .	11
5	Graphite mould used for gravity casting. . . . .	12
6	Cutting pattern of cast samples. . . . .	14
7	Simulation of mould filling as the melt reaches the insert. . . . .	15
8	Simulation of mould filling up to the studied surface. . . . .	16
9	Simulation of completed mould filling. . . . .	16
10	EDS mapping of zinc layer on pipe from Series 1-1. . . . .	17
11	Image of Sample 3 after sample preparation. . . . .	17
12	Micrograph of the gap in Sample 2. . . . .	18
13	Line scan across cracks along the interface in Sample 3. . . . .	19
14	Locally bonded area in Sample 3. . . . .	20
15	Image of Sample 4 after sample preparation. . . . .	21
16	Line scan across locally bonded area in Sample 5 . . . . .	22
17	Micrograph showing locally bonded areas in the gap of Sample 4. . . . .	23
18	Line scan across cracked area along the interface in Sample 6. . . . .	24
19	Image of Sample 7 after sample preparation. . . . .	25
20	Micrograph of Sample 7, showing cracks along the interface. . . . .	25
21	Line scan across cracks along the interface in Sample 8. . . . .	26
22	Image of Sample 11 after sample preparation. . . . .	27
23	Line scan across the interface in Sample 11. . . . .	28
24	Micrograph of the interface in Sample 12. . . . .	29
25	Micrograph of residual bonding in Sample 12. . . . .	30
26	Image of Sample 14 after sample preparation. . . . .	30
27	Micrograph of possible local bonding over the gap in Sample 14. . . . .	31
28	Micrograph showing cracks in both 6060 and A356 along the interface in Sample 13. . . . .	32
29	Line scan across the interface in Sample 13. . . . .	33
30	Cracked area along the interface in Sample 15. . . . .	34
31	Image of Sample 16 after sample preparation. . . . .	35
32	Optical image of the gaps and bonded areas along the pipe insert in Sample 16. . . . .	35
33	Line scan across local bonding on the outer side of the pipe in Sample 16. . . . .	36
34	Micrograph of Sample 17, showing a narrow gap through eutectic silicon in the cast aluminium. . . . .	37
35	Micrograph of bonded area inside the pipe, taken of Sample 17. . . . .	38
36	Image of Sample 20 after sample preparation. . . . .	39
37	Micrograph of the gap going through eutectic silicon in Sample 21. . . . .	39
38	Micrograph of Sample 19, showing the gap formed in the cast aluminium. . . . .	40
39	Micrograph of locally bonded area in Sample 19. . . . .	40
40	Simulation results showing solid fraction in Series 3-1. . . . .	41
41	Simulation results for first principal stress in Sample 3-2. . . . .	41
42	Simulation results for air gaps in Sample 3-2. . . . .	42

## List of Tables

1	Alloying element composition in A356 [11]. . . . .	5
2	Composition of alloying elements in aluminium alloy 6060 [14]. . . . .	6
3	Placements of thermocouples during casting. . . . .	13
4	Coating parameters for the series in Experiment 1. . . . .	15
5	Series description for Experiment 2. . . . .	27
6	Series description for Experiment 3. . . . .	34

# 1 Introduction

The issue of global warming is increasing, with the transportation sector being a large contributor [1]. An effective way to decrease emission from this sector, is by decreasing vehicle weight. This will reduce the amount of fuel consumed, thus also the emission into the environment. The benefit of weight reduction is also evident for electric cars, as a decrease in weight will increase the driving range [2].

Steel is known to have high strength and durability, and is therefore commonly used in the automotive industry. As steel has high density, replacing it with different lighter materials is of great interest. This has led to an increased use of light materials, such as aluminium and magnesium [3].

Aluminium alloys can achieve a combination of strength and ductility that is suitable for use in the automotive industry. In addition, they have the advantage of being light-weight. There are still certain components with strength requirements exceeding that of aluminium alloys, making it difficult to fully replace steel. To reduce the overall weight of a component, while maintaining required strength, compound casting can be used. Compound casting is casting of liquid metal onto a solid structure. Thus a light-weight metal can be cast onto a stronger extrusion profile.

In order to obtain a strong and durable compound cast part, there must be continuous metallurgical bonding between the two materials [4]. This is achieved by the formation of a reaction zone due to diffused alloying elements. A significant challenge when joining aluminium with another material is the natural oxide layer, which forms spontaneously on the aluminium surface when in contact with oxygen.  $\text{Al}_2\text{O}_3$  has a much higher melting temperature compared to industrial casting temperatures, and is thus thermodynamically stable during casting. The oxide layer is present on both liquid and solid aluminium, acting as a barrier that prevents formation of a diffusion zone between the alloys.

There have been extensive studies on how to achieve metallurgical bonding despite the oxide layer. A promising method is to remove the aluminium oxide layer on the inserts, while applying a reactive zinc coating [3]. Bonding in aluminium-aluminium compound castings have been achieved by high pressure die casting and zincate treatment of the insert [4]. There are still challenges related to the oxide layer, and the technology must be developed further before compound casting can be used industrially.

In this project, three experiments have been conducted, where bonding between two aluminium alloys has been studied. A356 was cast onto 6060 inserts, using various surface treatments and preheating temperatures.

A preliminary project was done as part of the course TMT4500 Materials Technology, Specialization Project. Then, a flux coating was applied to inserts to remove the oxide layer and achieve bonding. As results showed that the flux coating did not improve bonding between the alloys, another coating was tested in this thesis. Inserts were coated with zinc in the first experiment.

In the preliminary project, a gap was observed between the insert and cast alloy. This was likely caused by shrinkage during solidification, and was thus to be further studied in the second and third experiment in this thesis. In the second experiment, either the insert or mould was preheated while the other was kept at room temperature. Different inserts were used when casting at high

temperatures during the third experiment. Both the mould and insert were preheated, and kept at an elevated temperature for a fixed time after pouring.

Cast samples were studied in a scanning electron microscope to determine if proper bonding was achieved. The area along the A356-6060 interface was imaged and analysed by energy dispersive x-ray spectroscopy.

The simulation tool SutCast was used prior to casting to determine the process parameters. Another simulation software, StaMiSim, was used for stress analysis.

## 2 Theory

### 2.1 Compound Casting

The principle of a casting process is that a liquid metal is poured into a mould cavity to obtain the mould shape during solidification. Compound casting is similar, except that a solid component is placed into the mould prior to pouring [3]. Compound casting, also known as hybrid casting, is therefore the joining of dissimilar metals by casting one metal onto a solid structure of another.

Through the compound casting process, complex structures can easily be produced without additional joining steps. This makes compound casting better suited for mass production compared to other joining methods, as an extra production step would be both time-consuming and expensive. An additional advantage of compound casting, is that both the solid structure and the cast metal will contribute to the overall properties of the component [3]. Multi-material components can thus be designed to have a combination of properties suited for the conditions in which the component will be used. Weight reduction of cast parts due to compound casting of light-weight metals are especially interesting for the automotive industry. This technique is already being used for production of certain parts of the chassis, but further study is needed [3]. Different casting methods have been used when studying compound casting, such as gravity-, squeeze-, investment- and high pressure die casting. Compound casting of aluminium with various metals have been studied, mainly steel and copper, but also the joining of wrought and cast aluminium alloys.

### 2.2 Metallurgical Bonding and Intermetallic Phases

In order to achieve a strong bond between two different metals in a compound casting, formation of a metallurgical bond through a reaction zone is necessary. This zone is a volume along the interface, where the alloying elements of one metal have diffused into the matrix of the other [4]. The driving force in diffusion is the concentration gradient, making atoms move from a region with higher concentration of the specific element to lower concentration regions. The equation for steady-state diffusion in one direction is

$$J = -D \frac{dC}{dx} \quad (1)$$

where  $J$  is the diffusion flux in  $\text{atoms}/\text{m}^2 \cdot \text{s}$ ,  $D$  is the diffusion coefficient in  $\text{m}^2/\text{s}$  and  $\frac{dC}{dx}$  is the concentration gradient in  $\text{atoms}/\text{m}^4$ . The diffusion coefficient varies with different matrix- and diffusing elements, and increases with increasing temperature [5].

The diffusion coefficient is higher in liquids than solids. During compound casting, liquid metal will react with the surface of the solid insert. A reaction zone between the two alloys, which may contain intermetallic phases, is formed by the diffused atoms. Such phases can be brittle and cause cracks at the interface. It is therefore important to know what intermetallic phases might form when joining two metals. This depends on alloy composition and temperature [6]. When joining two aluminium alloys, some possible intermetallic phases are  $\text{Mg}_2\text{Si}$ ,  $\text{Al}_2\text{CuMg}$ ,  $\text{Zn}_2\text{Mg}$ ,  $\text{Al}_3\text{FeSi}$  and  $\text{Al}_8\text{FeMg}_3\text{Si}_6$  [4] [7]. Such phases can also be found in the alloys, and few intermetallic phases are generally formed in the reaction zone between two aluminium alloys.

### 2.3 Wettability

During casting, the liquid and solid materials should maintain contact to allow a diffusion layer to form evenly. The concept of how well a liquid spreads and covers a solid surface is called wetting [5].

A common way of testing wettability is a sessile drop method, where a liquid drop is placed onto a surface and the contact angle between the droplet and surface is measured [8]. This angle,  $\theta$ , is called the wetting angle, and is shown in Figure 1. Wettability increases with decreasing wetting angle, where an angle below  $90^\circ$  indicates good wetting.

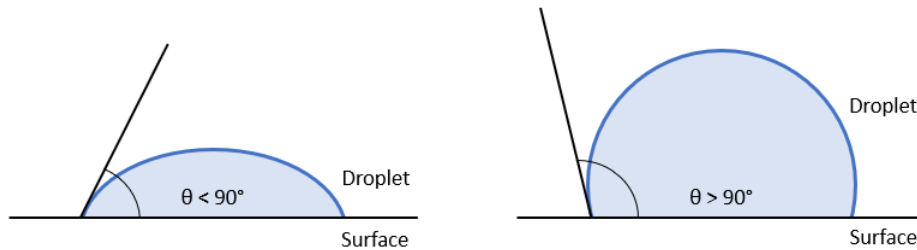


Figure 1: Illustration of the wetting angle,  $\theta$ , based on a figure in [5]. The left side shows good wetting, while the right side shows poor wetting.

Wetting is improved at elevated temperatures. Surface tension and viscosity both decrease with increasing temperature, resulting in a lower wetting angle [9].

### 2.4 Material Properties

Material selection is important when designing a component, as material properties can vary greatly. Aluminium alloys have a wide range of applications and are important metals within the automotive industry, where a combination of strength, formability and machineability is essential.

Aluminium alloys are categorised in two ways, based on whether the alloy is cast or wrought, and whether it is heat-treatable or not [6]. Cast alloys have good flowability of the melt and low temperature of solidification. The strength is due to alloying elements, and cast alloys are therefore often highly alloyed. Strengthening mechanisms for wrought alloys are deformation hardening and solid solution hardening. Wrought alloys should thus be ductile and are generally low alloyed. Both cast and wrought aluminium alloys could be heat-treatable. Heat-treatable alloys experience precipitation hardening. The alloy is heated to above solidus then quenched, resulting in supersaturated alloying elements being frozen in the aluminium matrix. As the alloy is held at an elevated temperature, hardening particles are precipitated. Non-heat-treatable alloys do not receive a strength contribution from this procedure. A requisite for precipitation hardening is that the solubility of the alloying element decreases significantly with decreasing temperatures.

The aluminium alloys used in this project are A356 and 6060, as cast metal and inserts respectively.



### 2.4.1 A356 Alloy

The A356 alloy is a heat-treatable cast alloy. Its good castability is mainly due to the small solidification temperature range. This small range improves feeding to potential pores by reducing the dendrite arm spacing. A longer dendrite arm length would trap the liquid during solidification, resulting in cavities.

During solidification, the shrinkage of aluminium is 6% [6]. This must be compensated for during casting, especially when designing the mould. By controlling the solidification direction and avoiding turbulence in the melt, cavities can be avoided. Generally, the cavities formed due to shrinkage are elongated and branched, while gas pores are spherical [10]. Pores are mainly due to the high  $H_2$  content in the melt. The linear thermal expansion coefficient for A356 is  $21 \mu\text{m}/\text{m}\cdot\text{K}$  [11].

Alloying elements also improve properties for compound casting. The composition of A356 is listed in Table 1 [11].

Table 1: Alloying element composition in A356 [11].

Element	Si	Fe	Cu	Mn	Mg	Zn	Ti	Other
wt%	6.5-7.5	$\leq 0.6$	$\leq 0.25$	$\leq 0.35$	0.2-0.45	$\leq 0.35$	$\leq 0.25$	$\leq 0.15$

Silicon is the main alloying element in A356, and is present both as particles and in solid solution. The viscosity of aluminium-silicon alloy melt is low, which improves flowability of the melt and thus form-filling during casting. Another important property of silicon, is that it expands during solidification, as opposed to aluminium and other alloying elements. Shrinkage can lead to cavities, which increase the risk of cracks forming and growing until fracture. The expansion of silicon compensates for this, and will therefore reduce the formation of cavities. Advantages due to silicon are most efficient close to the eutectic composition. As can be seen in Figure 2, this is 12.6 wt% Si. However, due to their combination of strength and ductility, hypoeutectic alloys are often used [6]. Silicon and magnesium present in the alloy reduces the melting temperature of the alloy, resulting in more time for bonding to be achieved [12]. The presence of magnesium can decrease surface tension in the aluminium melt, and magnesium can react with  $\text{Al}_2\text{O}_3$  [12]. Both factors improve wetting.

Aluminium-silicon binary alloys are not heat-treatable without additional alloying elements. In the A356 alloy, age hardening is possible by formation of precipitates such as  $\theta - \text{Al}_2\text{Cu}$ ,  $\beta' - \text{Mg}_2\text{Si}$  and  $\beta'' - \text{AlMgSi}$  [6].

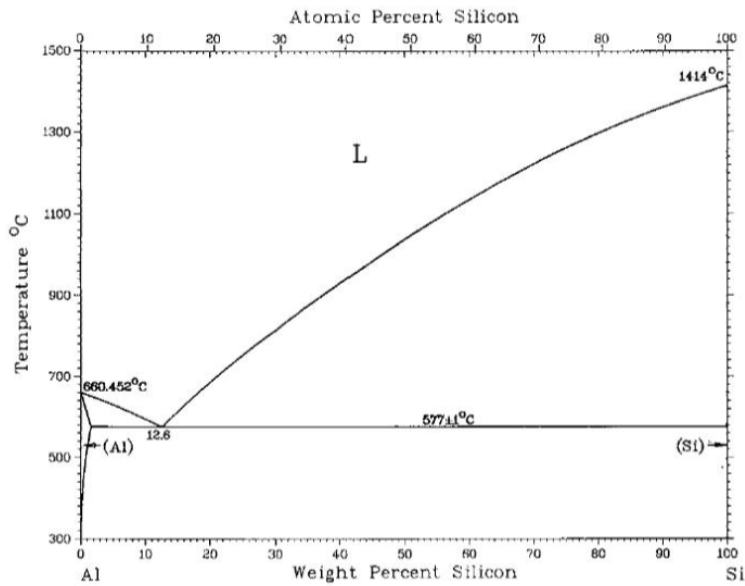


Figure 2: Al-Si binary phase diagram [13].

## 2.4.2 6060 Alloy

6060 aluminium alloy is a heat-treatable wrought alloy. The alloy has medium strength and very good corrosion resistance. Its alloying elements are shown in Table 2 [14].

Table 2: Composition of alloying elements in aluminium alloy 6060 [14].

Element	Si	Fe	Cu	Mn	Mg	Cr	Zn	Ti	Other
wt%	0.3-0.6	0.1-0.3	≤ 0.1	≤ 0.1	0.35-0.6	≤ 0.05	≤ 0.15	≤ 0.1	≤ 0.15

6060 contains the same alloying elements as A356, but less of all except magnesium. This alloy also contains a trace level of chromium.

Magnesium contributes positively to heat-treatment of the 6060 alloy, as age hardening is improved by formation of MgSi precipitates. Both manganese and chromium act as grain refiners when added to an Al-Si-Mg-alloy, while the addition of copper increases strength [6].

The amount of silicon is relatively low, but the properties mentioned for A356 still apply. The linear thermal expansion coefficient for 6060 is 23  $\mu\text{m}/\text{m}\cdot\text{K}$  [14]. This is higher compared to A356, and the 6060 alloy will thus shrink more during cooling.

## 2.4.3 The Oxide Layer

A natural oxide layer of  $\text{Al}_2\text{O}_3$  forms spontaneously on the aluminium surface when in contact with oxygen. This layer has a melting temperature of 2054  $^\circ\text{C}$  [15], which is more than three times as high as standard industrial casting temperatures of aluminium alloys. This oxide layer is thermodynamically stable during the casting process. Wetting of aluminium on  $\text{Al}_2\text{O}_3$ , though improving with

increasing temperature, is poor at casting temperatures [16]. An oxide layer will prevent diffusion of elements into the alloy, thus also preventing formation of a metallurgical bond. Removal of the oxide layer is especially important when joining two aluminium alloys, as oxide layers are present on both the solid insert and liquid front.

Oxide removal can be done through different methods. Sandblasting is a process in which sand particles are propelled onto a surface by compressed air [17]. The oxide layer is thus cleaned and roughened before further treatment, improving wettability [12]. Silica sand is often used, due to its relatively uniform grain size [18]. Pickling is when the oxide is removed through a chemical reaction. The solution applied to the surface is normally acidic [19].

## 2.5 Coating

Various coatings have been used to handle the oxide layer, either for removal or replacement.

Flux coatings are used to remove the oxide layer during the casting process [20]. The applied flux melts when sufficiently heated by the liquid cast metal. Reaction between the flux and aluminium oxide begins once the flux starts melting, dissolving the oxide layer. Removal of the oxide layer is thus dependant on successful melting of the flux. Residual flux and  $\text{Al}_2\text{O}_3$  at the interface would inhibit bonding. Some flux coatings have been documented to form stable phases by reacting with magnesium in an aluminium alloy [20]. Such reactions with other substances consume the flux, and less is then available to dissolve the aluminium oxide.

Metallic coatings are studied as a way to replace the oxide layer with a protective metal layer, thus preventing reoxidation of the aluminium surface. Various metals have been tested as coatings for aluminium, including nickel, copper, gallium and zinc [21] [22].

### 2.5.1 Zincate treatment

Compared to other metals, zinc has a low melting temperature of 420 °C and high solubility in aluminium at elevated temperatures, making it a well-suited coating material for aluminium inserts [23]. Wetting on the insert surface is also improved, as aluminium has better wettability on zinc than on aluminium oxide [24]. The zinc layer will melt during casting, and either become a part of the reaction zone or dissolve into the aluminium. The most common zincate treatment is to apply the coating by the so-called zincate process, which is often followed by galvanising [25].

The zincate process consists of two parallel chemical reactions. One to remove the oxide layer and one to deposit zinc onto the aluminium surface [4]. The  $\text{Al}_2\text{O}_3$  is removed by etching, while zinc is deposited through a redox reaction. During the redox reaction, aluminium is oxidised and dissolved, while zinc anions are reduced to form a metallic layer. The zincate process results in a thin zinc layer, typically  $< 1 \mu\text{m}$ , which prevents reoxidation. In an experiment by Papis et al., it was found that such a layer was too thin, as it dissolved into the melt during casting [4]. The zinc layer thickness was thus increased by galvanisation to 5 - 10  $\mu\text{m}$ . A thicker zinc layer can improve bonding, but may result in increased formation of brittle intermetallic phases [23].

Many studies have been done to improve the zincate treatment method, and aluminium-aluminium compound castings have been successfully manufactured. High pressure die casting was used by

Rübner et al. in 2011, with a combination of the zincate process and galvanisation [26]. The zinc layer reportedly reacted during casting, and the zinc distribution varied over the transition zone. Thus a variation in microstructure was also observed. The reaction zone thickness increased with increasing thickness of the initial zinc layer. A similar zincate treatment was used by Liu et al. for a squeeze casting experiment [27]. The thickness of the zinc layer was varied, from 300-500 nm to 5  $\mu\text{m}$  and 10  $\mu\text{m}$ . Metallic bonding was achieved for samples with 5  $\mu\text{m}$  and 10  $\mu\text{m}$  thick zinc coating. The tensile strength did not vary much between these samples. Zinc coated samples achieved bonding at a preheating temperature of 250°C, pouring at 700°C and 30 MPa applied pressure. It was found that increasing applied pressure could improve tensile strength and hardness, due to reduction of defects, microstructure refinement and decreased amounts of eutectic silicon.

## 2.6 Scanning Electron Microscopy

A scanning electron microscope (SEM) is an important tool, as high resolution images can be taken and the microscope is compatible with equipment suitable for studying microstructure. Resolution in an optical microscope is restricted by the wavelength of the incident light beam, and the maximum magnification is around 1000x. Because the wavelength of the electron beam is so small, the resolution in SEM is instead restricted by electron optical aberrations. The resolution of a scanning electron microscope is approximately 1 nm [28].

In an SEM, a beam of primary electrons is emitted from the electron gun and focused by a series of lenses before hitting the sample surface. Here, electrons interact with the material by elastic and inelastic scattering. Depending on how the primary electrons interact with the material, different types of electrons are emitted and detected by their respective detectors.

Primary electrons travel relatively far into the sample, before being elastically scattered and emitted as backscattered electrons. These are used for Z- and channeling contrast. Z-contrast, known as atomic number contrast, results in an image where phases with different mean atomic numbers can be distinguished. A higher atomic number implies that the atom is larger, and thus more likely to be hit by a primary electron and produce a backscattered electron. Phases with higher mean atomic number will then emit more backscattered electrons, which causes the detected signal to increase and the phases to appear brighter in the image. As grains have different crystal orientations, some will backscatter more electrons and the increased intensity will result in a brighter grain in the image. This is called channeling contrast or grain contrast [28].

Secondary electrons are ionization products, generated by either primary electrons entering the sample or backscattered electrons leaving. The energy of secondary electrons is lower compared to backscattered electrons, and they are used when imaging topography of a sample surface [28].

### 2.6.1 Energy Dispersive X-ray Spectroscopy

Energy dispersive x-ray spectroscopy (EDS) is used in SEM to determine the elements present in a sample area. An x-ray is generated when an electron is de-excited to fill a vacancy created by an inelastically scattered lower-shell electron, as shown in Figure 3 [28].

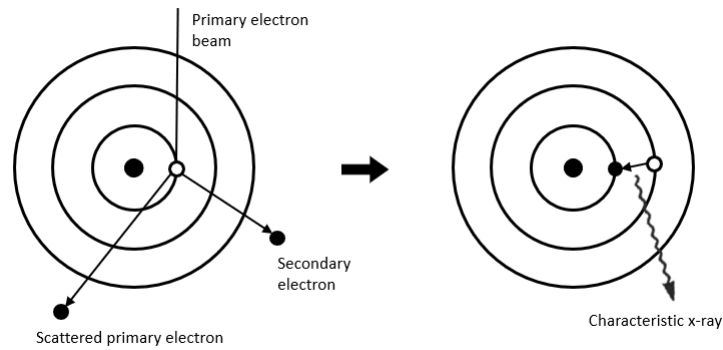


Figure 3: Formation of characteristic x-ray, based on a figure in [28].

The energy of this x-ray is characteristic for both the element and the two shells in which the electron de-excited. Based on the signal count of detected x-rays, a spectrum is created. Energy peaks in the spectrum show the elements detected in the sample area, whereas the relative size of a peak shows the relative amount of the corresponding element.

## 2.7 Simulation

Simulation is a useful tool to analyse the casting process, with benefits such as repeatability and reduction in project cost and time. By simulating an experiment prior to casting, design and process parameters can be optimised, thus avoiding expensive and time-consuming changes during the experiment. Temperature data for the mould, insert and cast material becomes available, and can be useful both when designing an experiment and for comparison.

SutCast is a software that visualises mould filling and solidification by calculating a set of mathematical formulas using the finite difference method [29]. This method simplifies the governing differential equations and boundary conditions by replacing the derivatives with approximate values. These values are expressed as the difference between nodal displacements. Solving the discrete representations results in an approximate solution to the differential equations [30].

The simulation software StaMiSim is developed by the Institute for Energy Technology (IFE), and also uses the finite element method. Calculations of solid fraction, stresses in a sample and air gap formation during solidification can be solved with this software [31].



### 3 Experimental

#### 3.1 Insert Preparation

Inserts of 6060 extrusion profiles were cut to a length of approximately 100 mm in a Struers Labotom-5 with a 10S25 blade. Both rods and pipes had an outer diameter of 10 mm, with the pipes having a wall thickness of 1 mm.

All non-coated inserts were ground with 1200 grit prior to casting.

##### 3.1.1 Zinc Coating

Zinc coating was applied to a total of twelve pipes through three different procedures. First, all pipes were degreased in an electrolytic solution containing 13 g/L Riddine 1803. The pipes were dipped for 60 s at 65°C, before then being cleaned in spring water followed by distilled water.

The same solution was used for all three different coating procedures. 150 g/L NaOH and 20 g/L ZnO were mixed with water to a total of 4500 mL. The temperature of the solution was held within the range of 30-35 °C during dipping.

The first parallel was dipped in zincate solution for 30 s, with no current applied. The coated pipes were then dipped in a beaker with spring water before being cleaned with distilled water and air dried.

An alternating current was applied during both the second and third parallel. A zinc coated steel plate was the initial anode, and the aluminium pipe was the initial cathode. Alternating the current results in the pipe alternating between being the cathode and anode. This can be seen in Figure 4, which shows the current during one cycle. A voltmeter connected to the power source measured a voltage of 6.9 mV during the surface treatment.

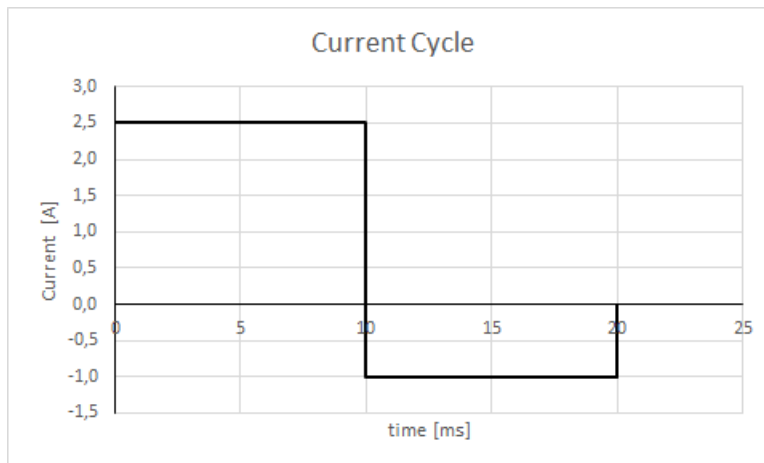


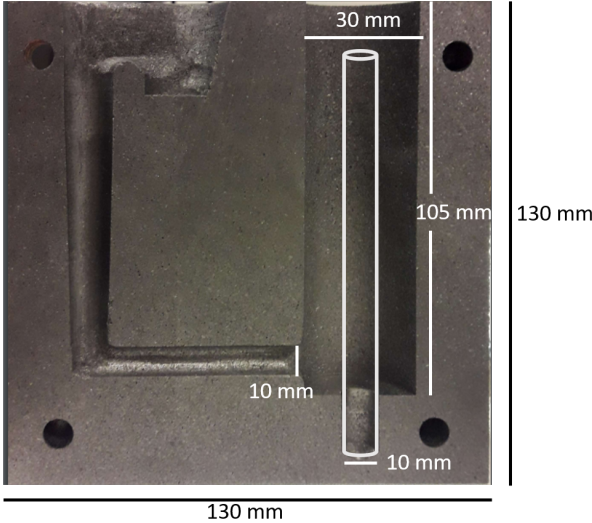
Figure 4: Current and time for one cycle of the zincate treatment for parallel 2 and 3.

After dipping, the pipes were immersed in a beaker with spring water before being cleaned with

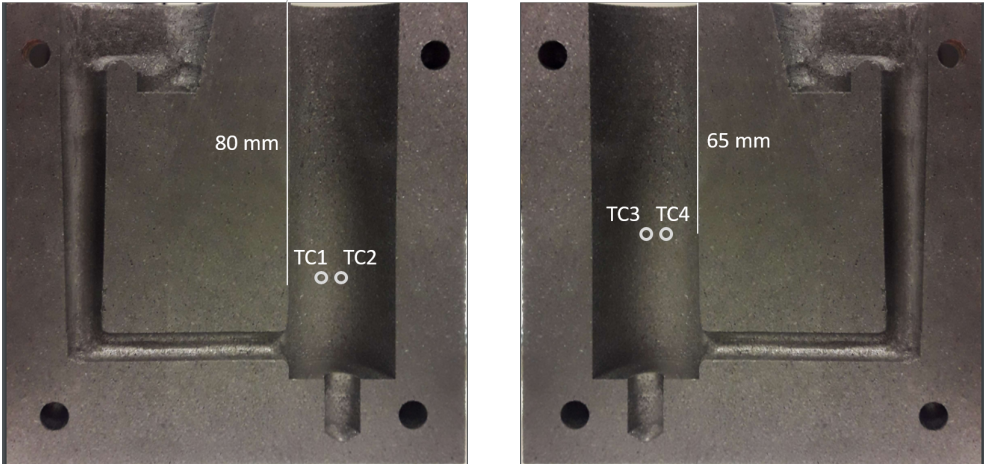
distilled water and air dried. In the second parallel, dipping time was 8 s, which equals 400 cycles. The third parallel had a dipping time of 15 s, corresponding to 750 cycles.

### 3.2 Compound Casting

Figure 5 shows the graphite mould used for gravity casting, with placements of the inserts and thermocouples drawn in. Placement of all thermocouples are also described in Table 3.



(a) Mould illustrating insert placement and measurements.



(b) Mould with illustrated thermocouple placements.

Figure 5: Graphite mould used for gravity casting.



Table 3: Placements of thermocouples during casting.

Thermocouple	Distance from top [mm]	Placement
TC1	80	Mould wall
TC2	80	Cavity/A356
TC3	65	Mould wall
TC4	65	Cavity/A356
TC5	50	Inside Pipe

The mould, as well as the ceramic pouring ladle, was coated with boron nitride to improve the flow of the melt. The melt was poured at approximately 700°C for all castings. A Nabertherm resistance furnace was used for preheating the mould and inserts.

Three different casting experiments were conducted. In the first experiment, the three series of zinc coated inserts were used. Both the mould and inserts were preheated to 250°C prior to casting. The mould maintained in the open furnace until the part had solidified.

The second experiment was conducted in two series. In the first series, a pipe insert was preheated to 600°C, while the mould was kept at room temperature. Casting was done outside the furnace after placing the hot insert into the mould. For the second series, pipe inserts were kept at room temperature while the mould was preheated to 600°C. The insert was placed in the mould before casting outside the furnace.

Two series were cast for the third experiment. Both series were done by preheating the insert and mould to 600°C. After pouring, the temperature was held at approximately 600°C by closing the furnace for 5 min. The mould was then removed from the furnace, for the part to completely solidify. Different inserts were used for the two series. Pipes were used for the first series, while rods were used for the second.

For all experiments, three samples were cast for each series, resulting in 21 samples.

### 3.3 SEM Sample Preparation

All cast parts were cut with a 10S25 blade on a Struers Labotom-5. As shown in Figure 6, the samples were cut to a thickness of approximately 15 mm. The upper side of the sample was to be studied.

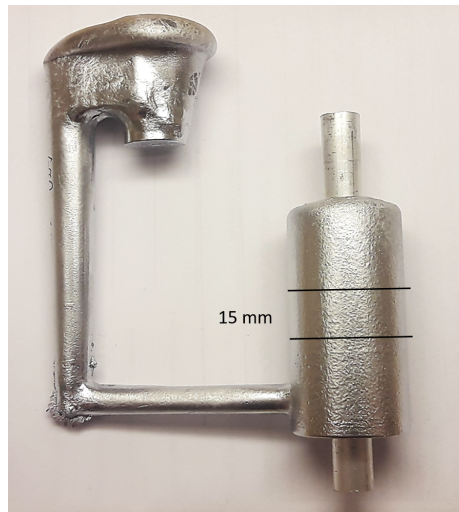


Figure 6: Cutting pattern of cast samples.

After cutting, the samples were ground using 320 grit paper on a Struers RotoPol-31 with RotoForce-4. Automated polishing was then performed with the Struers Tegramin-30, on polishing discs with 9  $\mu\text{m}$ , 3  $\mu\text{m}$  and 0.04  $\mu\text{m}$  grains. After grinding and between each polishing step, the samples were cleaned in a Struers Lavamin by ultrasound and water.

Unused inserts with different zinc treatments were prepared for SEM study of the zinc layer. The pipes were cut to approximately 20 mm in length in a Struers Labotom-5 with a 10S25 blade. The short pipes were then cast in EpoFix resin before being ground, polished and washed according to the previously described procedure.

All samples were studied in a Zeiss Supra 55VP field emission scanning electron microscope. An accelerating voltage of 10 keV and 10 mm working distance was used. Images of the sample surface were taken with both secondary- and backscattered imaging, and the elements present were detected through EDS.

### 3.4 Simulations

Simulations were run in SutCast before casting to find suitable process parameters for Experiment 1. A simple model of the cast part was provided, and the mesh edited in SutCast to describe the insert and mould. The input data used for the simulation can be found in Appendix A.

Solidification temperatures, solid fractions, stresses and air gaps in the compound cast parts were simulated with StaMiSim at IFE.

## 4 Results

### 4.1 Zinc Coated Inserts

The first experiment was conducted in three series, where zinc coated insert were used. Table 4 shows the coating parameters for each series, and the respective samples.

Table 4: Coating parameters for the series in Experiment 1.

Series	Dipping Time [s]	Current Cycles	Samples
1-1	30	-	1, 2, 3
1-2	8	400	4, 5, 6
1-3	15	750	7, 8, 9

The preheating and pouring temperatures were identical for all castings in this experiment, 250°C and 700°C respectively.

### 4.2 Simulation in SutCast

The preheating temperature used in this experiment was decided after simulation of the casting process in SutCast. The following figures show the simulation results, where the insert was heated to above the melting temperature of zinc, 420°C.

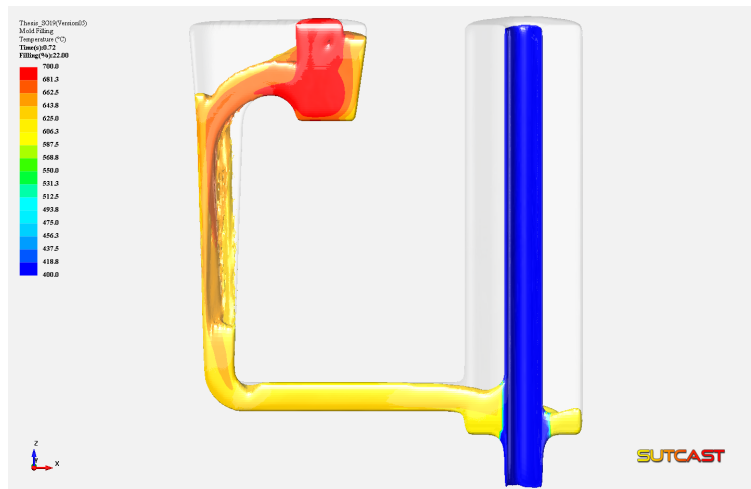


Figure 7: SutCast simulation results showing mould filling as the melt reaches the insert. The temperature at the insert surface increases immediately.

Figure 9 shows that when the filling was complete, the temperature of the melt would theoretically be below solidus for A356. Form filling would thus not have been completed, which was experienced during casting.

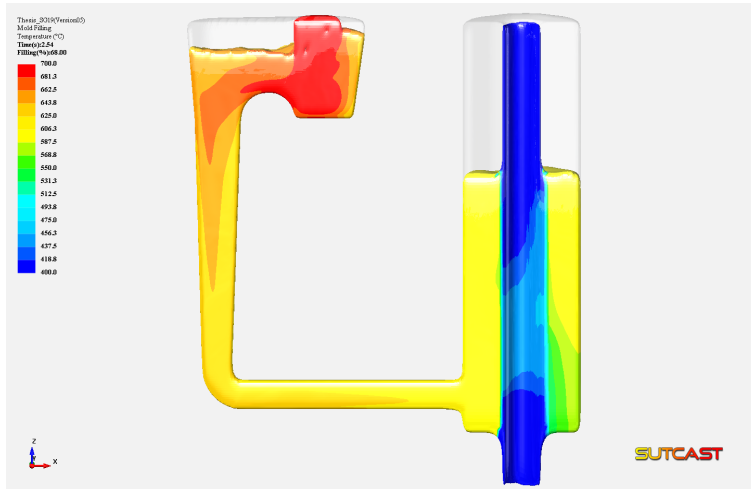


Figure 8: SutCast simulation results showing mould filling up to the studied surface. The pipe has now heated to above the melting temperature of zinc on the side opposite to the inlet.

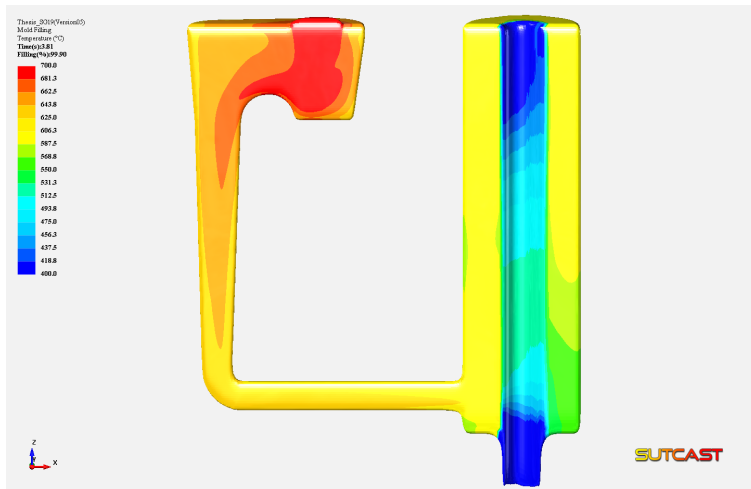


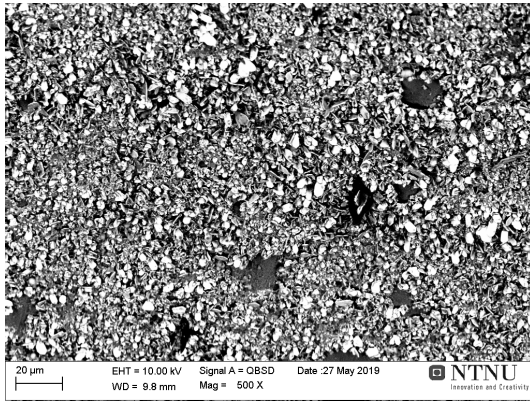
Figure 9: SutCast simulation results showing completed mould filling. The temperature exceeded the melting temperatures for zinc in most parts of the pipe.

#### 4.2.1 Zinc Layer Thickness

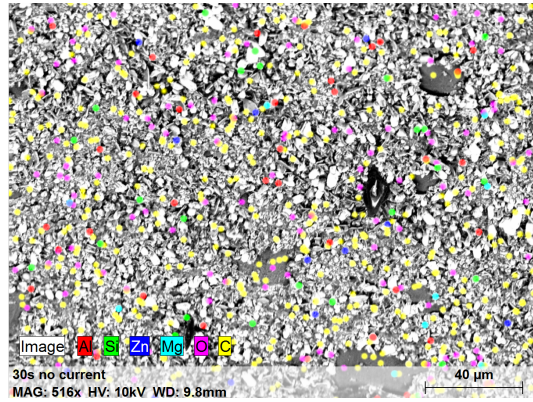
In order to determine the appearance of the zinc coating on the pipes, one pipe from each coating treatment was examined prior to casting.

During the surface treatment of Series 1-1, it was observed that barely any reaction occurred until the pipe had been in the solution for 10-15 s, at which point bubbles became visible.

The zinc layer surface at the outer side of a pipe from Series 1-1 was micrographed and analysed with EDS mapping, and the result is shown in Figure 10.



(a) Zinc coated surface of pipe from Series 1-1.



(b) EDS mapping results.

Figure 10: Zinc layer on outer surface of pipe from Series 1-1. Mapping results show mostly carbon and oxygen was detected.

Only small amounts of zinc were detected, as well as aluminium and other alloying elements. The EDS mapping mostly detected carbon and oxygen. The zinc layers was not observed when studying the pipe directly from above, and the thickness could thus not be accurately measured.

#### 4.2.2 Series 1-1: Zinc Treatment for 30 s without Applied Current

Sample 1 was not studied, as the insert loosened during sample preparation, suggesting no bonding.

Figure 11 shows the surface of Sample 3, with a gap visible between the insert and cast aluminium. Multiple pores, due to gas and turbulence in the melt, are also visible.

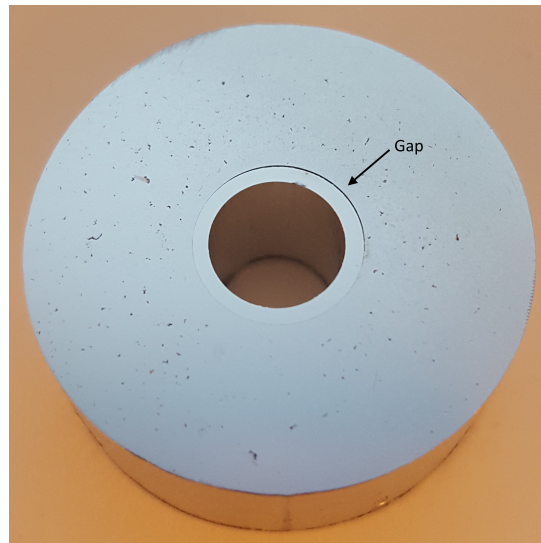


Figure 11: Surface of Sample 3, with a visible gap between the insert and cast aluminium.

The gap seen in Figure 11 is visible around the entire insert when studied with SEM. The thickness of the gap varied from 20  $\mu\text{m}$  to 100  $\mu\text{m}$ , but was approximately 40  $\mu\text{m}$  on average. Such a gap between the insert and cast aluminium can be seen in Figure 12.

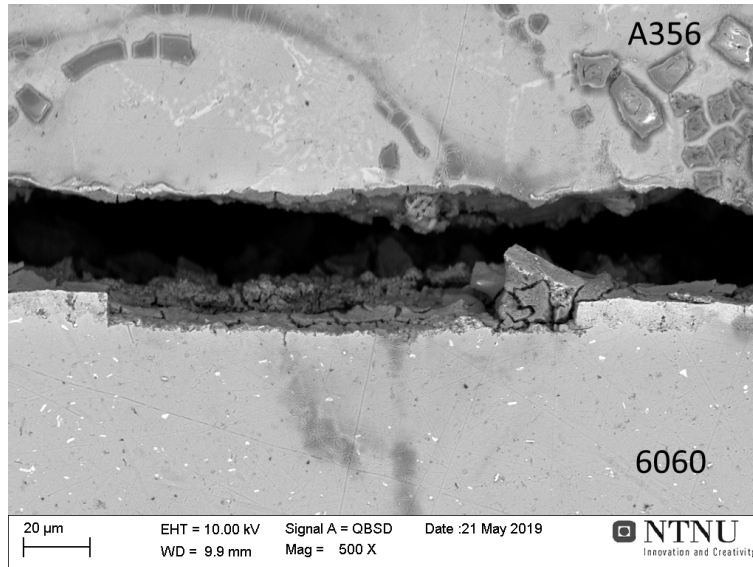
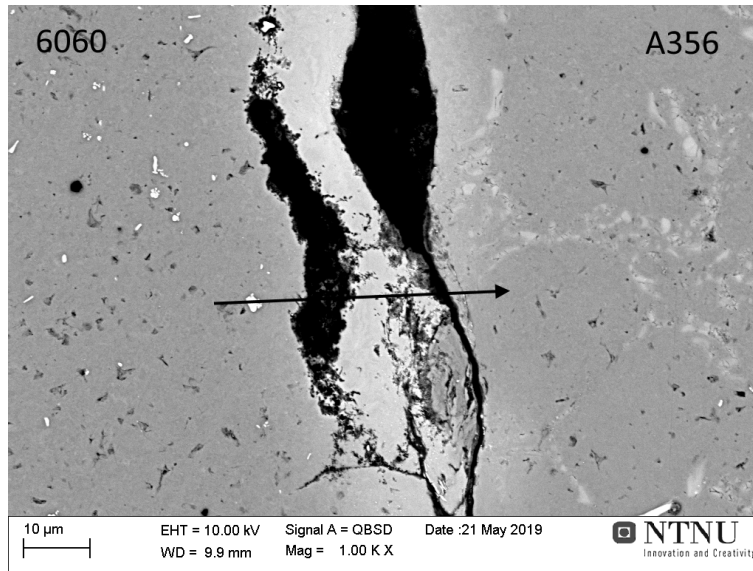
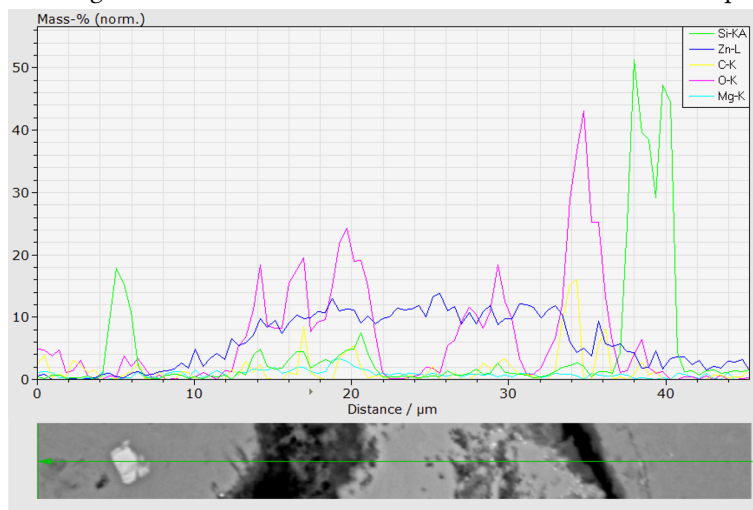


Figure 12: Micrograph showing the gap between the insert and cast aluminium in Sample 2.

Some areas along the insert suggested that there had been bonding before the gap formed. Examples of this were found on both samples in the series, and are shown from Sample 3 in Figure 13 and 14. A line scan was performed along the arrow in Figure 13.



(a) Cracks along the interface. The arrow indicates where a line scan was performed.



(b) Line scan showing alloying elements detected in the aluminium.

Figure 13: Micrograph showing cracks between the A356 and 6060 in Sample 3.

Aluminium was detected along the entire line scan. As can be seen in Figure 13, a gap between the insert and cast aluminium, though narrow in some places, was continuous through the area. Another crack formed parallel to the continuous gap, most likely in the 6060 alloy, as low amounts of silicon was detected in the area between the two cracks. Bright contrast in this area suggests zinc is present, which is supported by the line scan. Oxygen and some carbon were detected over cracked areas. The widest crack studied by the line scan also contained increased amounts of silicon and magnesium.

An area of possible local bonding is shown in Figure 14. The overall gap is wider here than in Figure 13, and the area that might have bonded is larger.

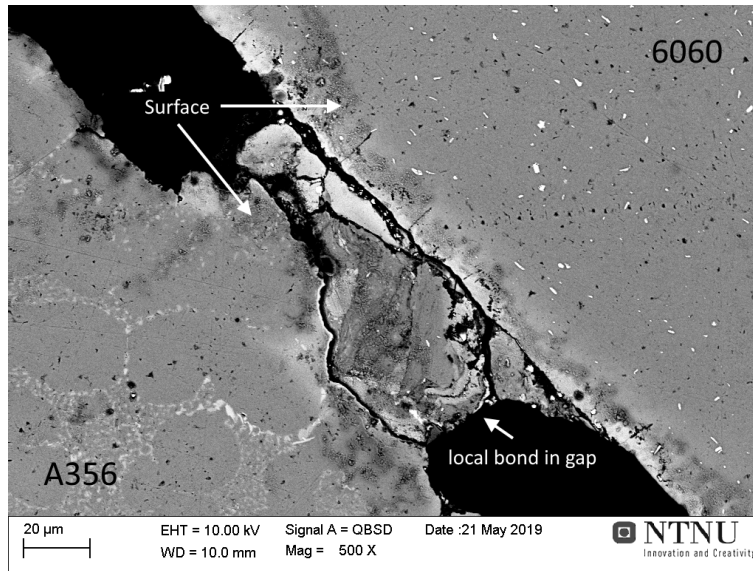


Figure 14: Micrograph of Sample 3. The local bond is further down into the gap compared to the surface areas, and visually separated by thin black contrast.

The local bond was studied in an optical microscope, and determined to be located approximately 6 μm down into the gap. What appears to be dark contrast cracks in Figure 14 is the surface edge.

The bright contrast at the surface indicates the presence of zinc, and is confirmed by a line scan in Appendix B. The zinc is present in both 6060 and A356. High amounts of silicon on the local bond suggest this is A356.

#### 4.2.3 Series 1-2: Zinc Treatment for 8 s with Applied Current

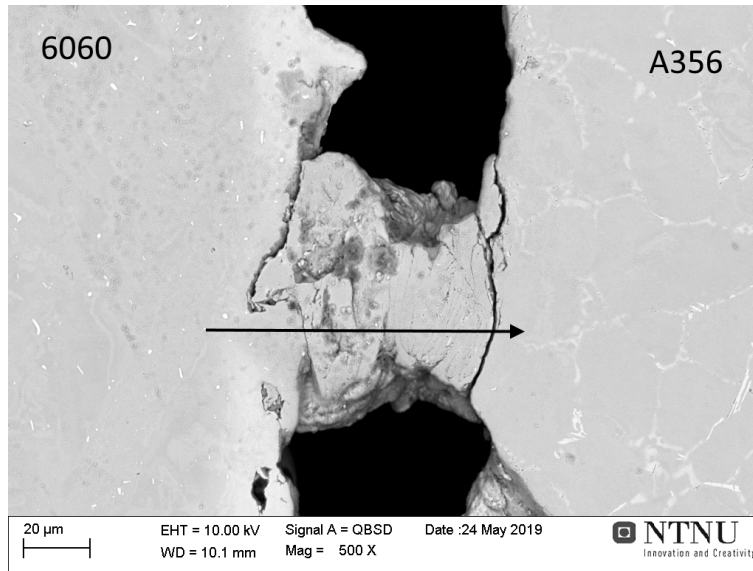
A gap between the insert and cast aluminium can be seen in Figure 15, as well as pores formed during casting.



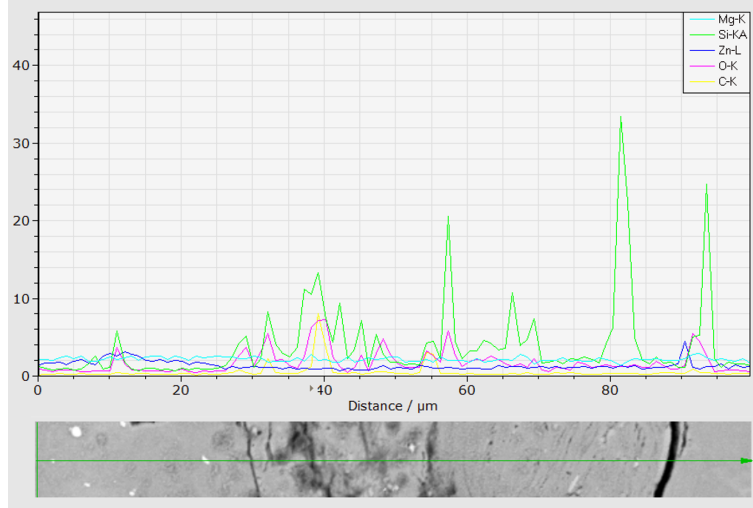


Figure 15: Surface of Sample 4, with a visible gap between the insert and cast aluminium.

In this series, the gap width varied, with the widest part in general measuring approximately 40  $\mu\text{m}$ . Such a wide gap can be seen on one side of the insert in Figure 15. The other side appears to show bonding, but with study in SEM it was observed that the gap was continuous along the insert interface. No bonding was observed in any sample for this series, but local areas suggested that there had been bonding prior to solidification. Figure 16 shows one such area in Sample 5.



(a) Locally bonded area in Sample 5. The arrow indicates where a line scan was performed.



(b) Line scan showing alloying elements detected in the aluminium.

Figure 16: Micrograph showing residual bonding in the gap between 6060 and A356.

The remainder of local bonding seen in Figure 16a was found in the area in Figure 15 where the gap is visible. As the gap likely formed due to shrinkage, only cracks along the interface of this area formed, indicating some bonding was achieved. A line scan across the area showed higher amounts of zinc in 6060 compared to the locally bonded area, suggesting no diffusion of zinc into the cast aluminium. Oxygen was detected at the cracks. The interface between A356 and 6060 is found in the line scan to be where the silicon content drops and the amount of detected zinc increases.

Figure 17 shows a relatively wide gap with two similarly bonded areas in Sample 4.

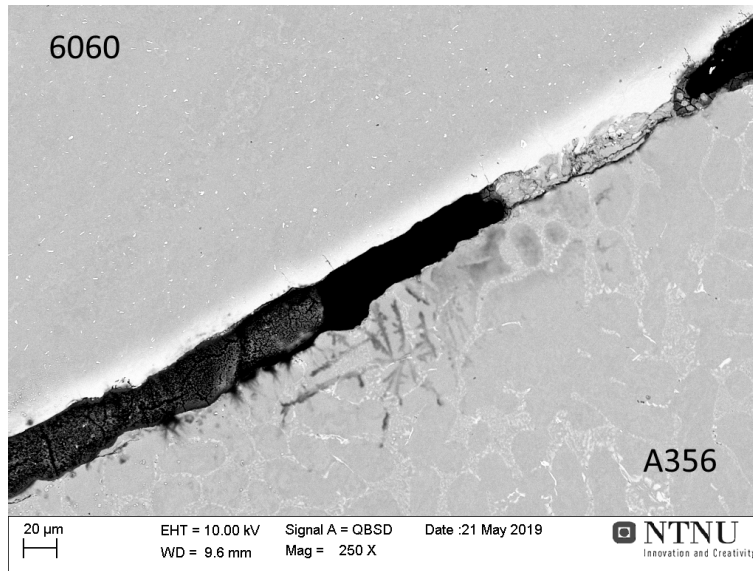
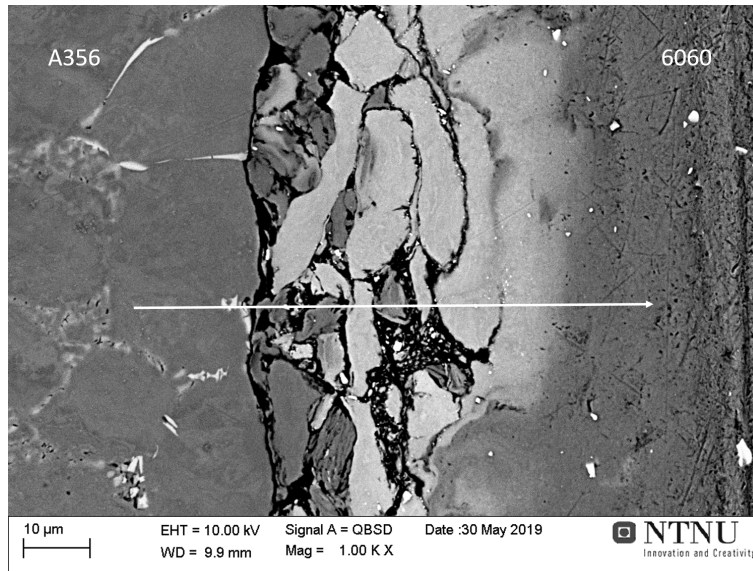
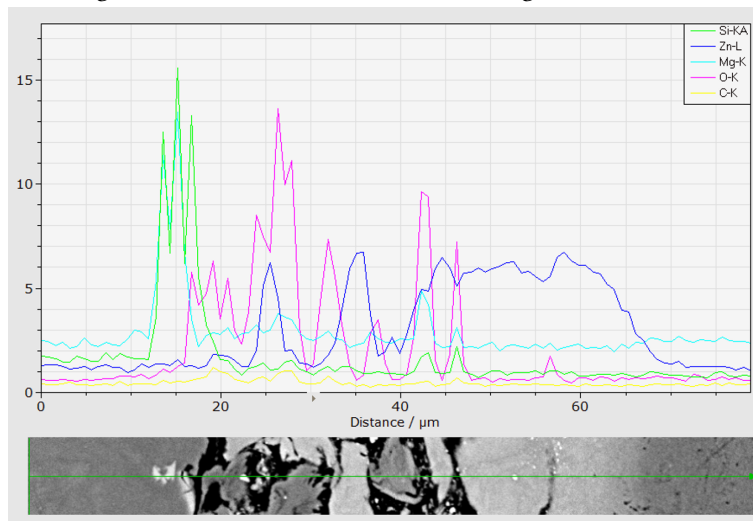


Figure 17: Micrograph showing locally bonded areas in the gap of Sample 4.

No bond remained after cooling, as cracks formed along the insert and cast aluminium sides of the local bonds. Areas like this were found in all samples in the series. A bright contrast, indicating zinc, can be seen along the whole insert edge. This can be seen more clearly in Figure 18, which shows a cracked area along the interface in Sample 6.



(a) Cracked area along the interface, with an arrow indicating where a line scan was performed.



(b) Line scan showing alloying elements detected in the aluminium.

Figure 18: Micrograph showing cracks in the area between A356 and 6060 in Sample 6.

The figure shows an area where the insert surface most likely melted, but no bonding was achieved. Increased amounts of zinc in 6060 can be seen as bright contrast in Figure 18. This is useful to distinguish the two alloys in the cracked area. The white phase at the A356 edge is shown to contain high amounts of silicon and magnesium. Spikes in the oxygen content is seen at the cracks.

#### 4.2.4 Series 1-3: Zinc Treatment for 15 s with Applied Current

The insert of Sample 9 also loosened during sample preparation, and was thus not studied further.

Figure 19 shows the studied surface of Sample 7. A gap is visible between the insert and cast aluminium, though not as large as in the previous series.

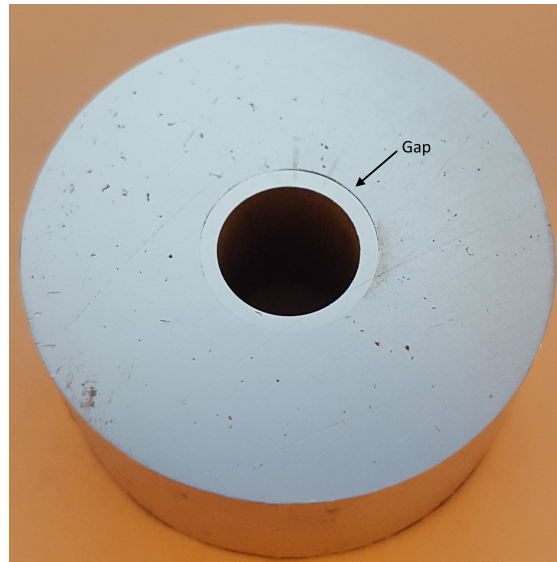


Figure 19: Surface of Sample 7, with visible gaps between the insert and cast aluminium.

In Figure 19, bonding appears to have formed across from the visible gap. By closer examination in the SEM, cracks were found throughout the interface suggesting poor bonding. This is shown in Figure 20.

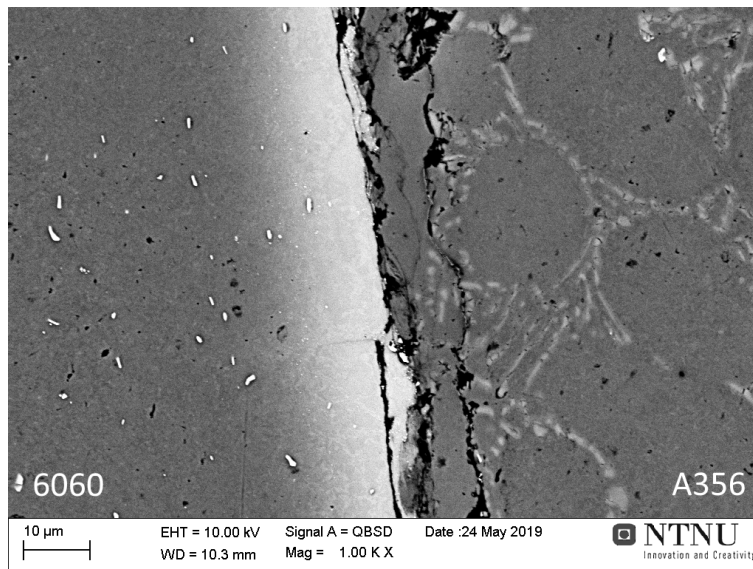
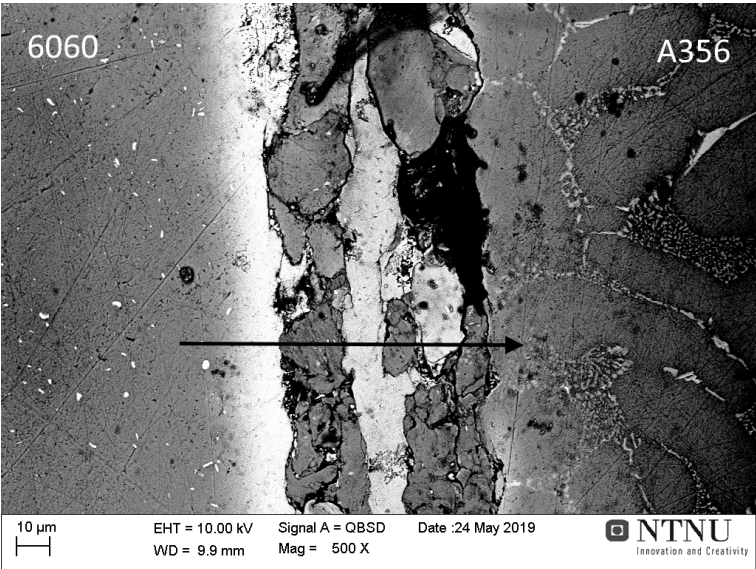


Figure 20: Micrograph of Sample 7, showing cracks along the interface.

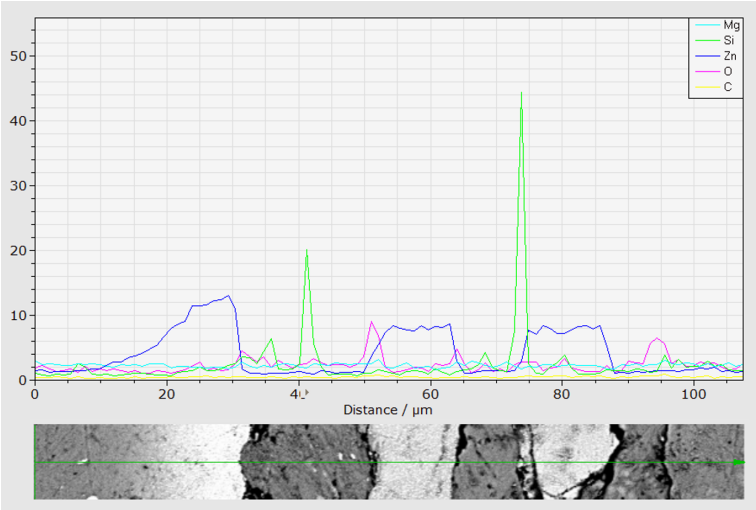
The bright contrast along the insert interface shows how the zinc diffused into the 6060 aluminium during preheating. The thickness of the zinc diffusion layer is 10-15 µm. Increased amounts of zinc

were not detected in the cast aluminium. Cracks are mainly in the A356, especially in and along the eutectic silicon phase. Some cracks also cut through the zinc-rich part of the insert.

Figure 21 also shows an area where the aluminium has cracked along the insert interface. A line scan was performed over the transition zone between the bulk 6060 and A356.



(a) Cracks along the interface. The arrow indicates where a line scan was performed.



(b) Line scan showing alloying elements detected in the aluminium.

Figure 21: Micrograph showing cracks between the 6060 and A356 in Sample 8.

The composition variation over the line scan can also be seen as varying contrast in the micrograph. A zinc diffusion layer can be seen along the 6060 interface, but areas in the transition zone are also shown to contain zinc. The increase in oxygen across the line scan corresponds to cracks in Figure 21a, where an oxide layer is expected to be present. Increased amounts of zinc and silicon alternate in the layers over the line scan. Bright areas, containing higher amounts of zinc, is believed to be

6060. Areas with higher amounts of silicon are dark, and are believed to be A356. The oxide layer would have kept the two alloys separate during casting. It is also possible for zinc to have dissolved into the cast aluminium, and the transition layer only consisting of A356.

### 4.3 Preheated Mould or Insert

In this experiment, casting was conducted using different preheating of the mould and pipe inserts. One was kept at room temperature, while the other was preheated to 600°C. The difference between the two series is summarised in Table 5.

Table 5: Series description for Experiment 2.

Series	Preheating	Samples
2-1	Insert	10, 11, 12
2-2	Mould	13, 14, 15

#### 4.3.1 Series 2-1: Preheated Insert

The surface of Sample 11 is shown in Figure 22. There is a relatively thin, but still visible gap between the insert and cast aluminium.

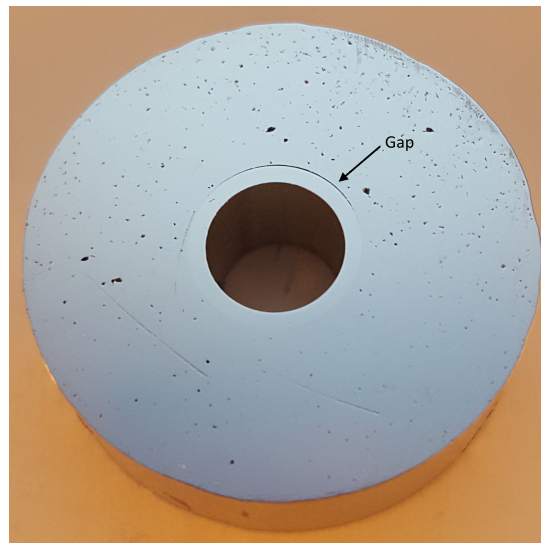
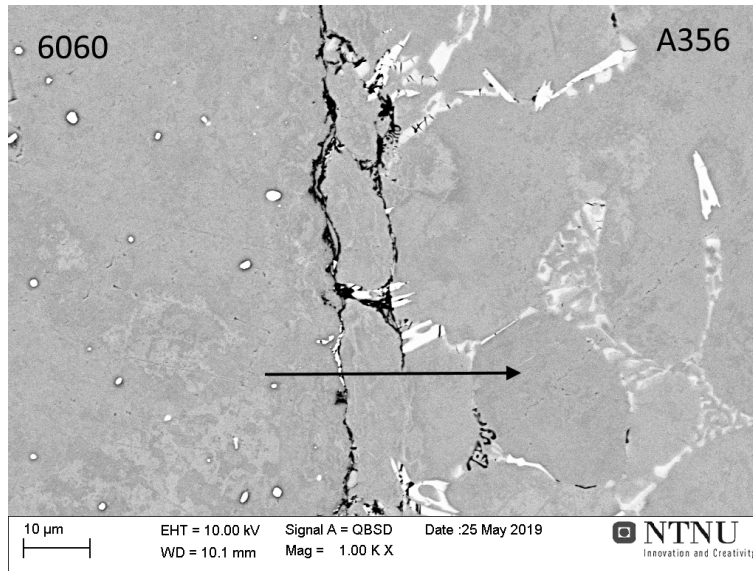
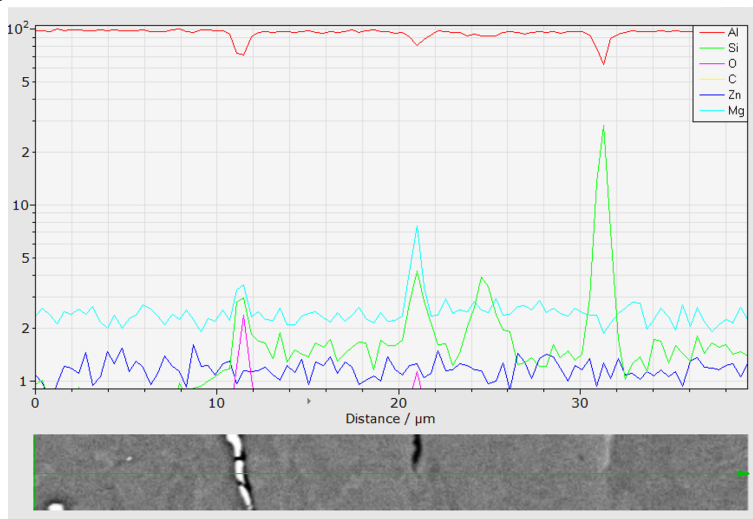


Figure 22: Surface of Sample 11, with visible gaps between the insert and cast aluminium.

A line scan was performed over an area with multiple cracks in the interface. Both the cracked area and line scan are shown in Figure 23.



(a) Cracks along eutectic silicon at the interface. The arrow indicates where a line scan was performed.



(b) Line scan showing detected elements. The y-axis is logarithmic.

Figure 23: Micrograph of Sample 11, showing cracks along eutectic silicon at the interface and in the cast aluminium.

A crack follows the interface, as part of the continuous gap along the entire insert. In this area, the narrow crack is in the eutectic silicon in A356. Some also branch into the cast aluminium. An increase in silicon over a crack can be seen in the line scan. The amount of silicon also indicates where the interface between 6060 and A356 is. Peaks in the magnesium content across the line scan corresponds to cracks as well.

In the area shown in Figure 23, the surface of the hot insert appears to have melted during casting, due to cracks forming along the eutectic silicon as opposed to at a well defined interface. This suggests some local bonding was achieved before cracks formed during cooling.



This does not appear to have happened in an area shown in Figure 24, where a continuous crack can be seen along the insert in Sample 12.

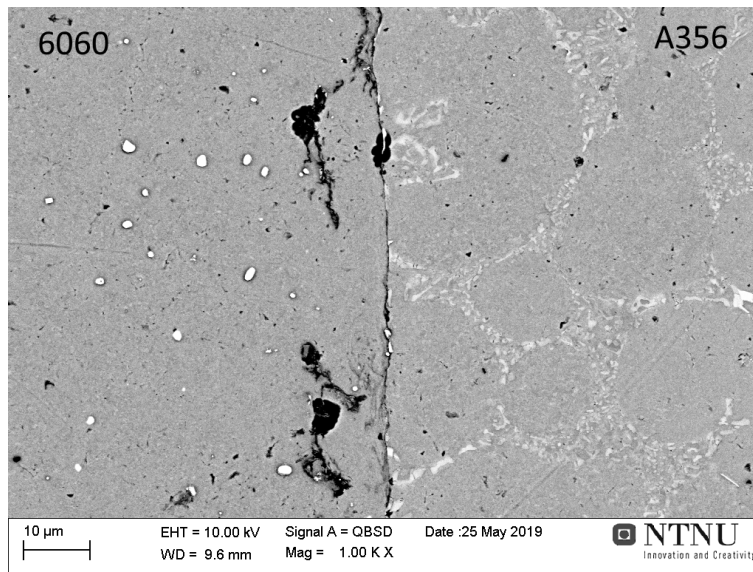


Figure 24: Micrograph of the interface in Sample 12.

Though the crack along the interface is only approximately 0.3 µm, no signs of bonding between the insert and cast aluminium are shown in Figure 24.

The bright particles in the 6060 aluminium was determined by EDS spot analysis to be a ternary AlFeSi phase. Results from the EDS spot analysis can be found in Appendix B, and indicate the visible precipitates in 6060 are Al<sub>5</sub>FeSi. The analysed particle was found in Sample 11, and is assumed representative for all inserts.

Figure 25 shows a local area where A356 remained in contact with the insert after solidification.

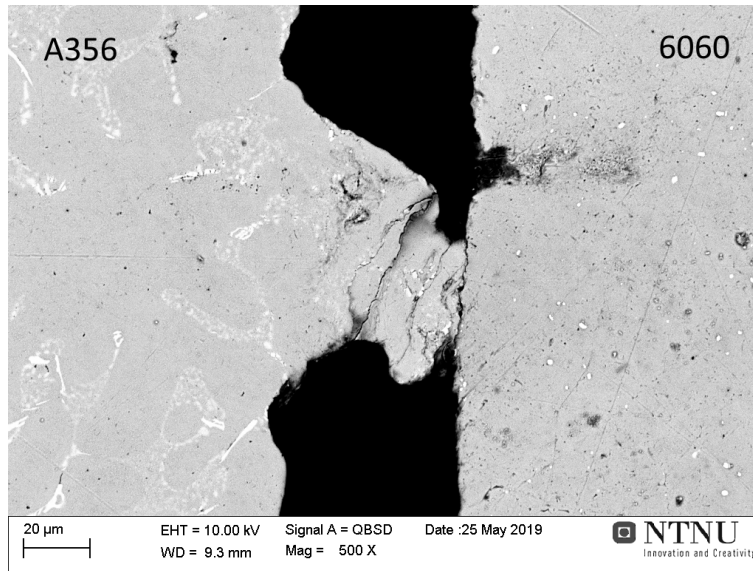


Figure 25: Local area of residual A356 over the gap in Sample 12.

The amount of silicon along a line scan, shown in Appendix B, suggests that the locally boned area consists of A356. Eutectic silicon and AlFeSi particles can be seen in the A356 and 6060 respectively.

#### 4.3.2 Series 2-2: Preheated Mould

Samples in this series were cast after preheating the mould. The flowability of the melt improved noticeably compared to Series 2-1. Figure 26 shows the surface of Sample 14. The visible gap is wider compared to Sample 11, but also shorter.

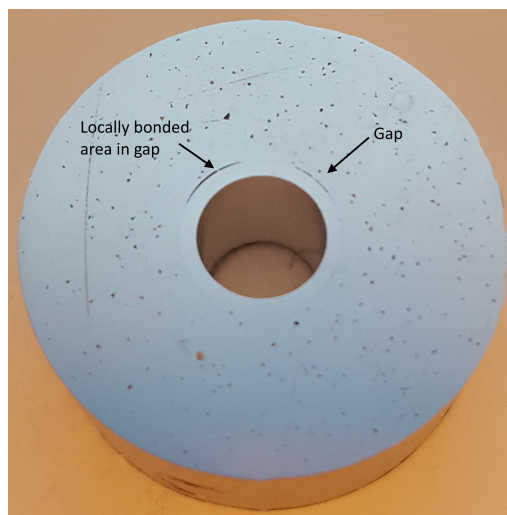


Figure 26: Surface of Sample 14. An area of local bonding can be seen in the gap.

A small area of local bonding can be seen in the wide gap, and a micrograph of this local area is shown in Figure 27.

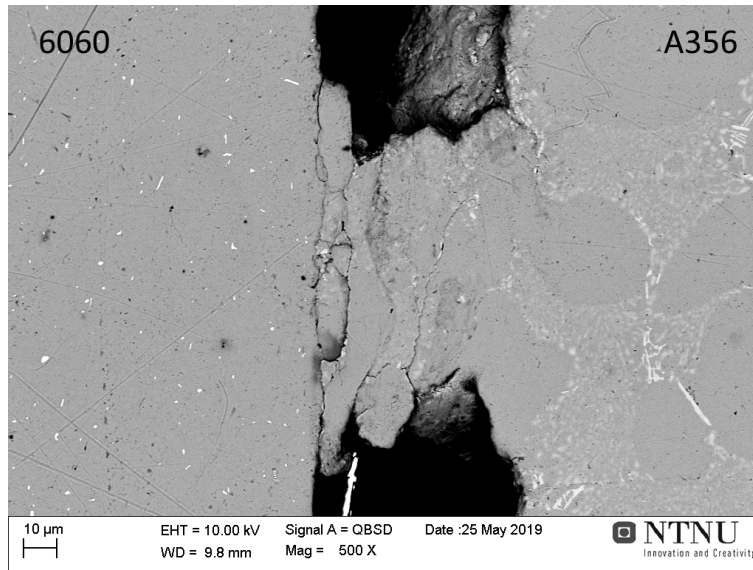


Figure 27: Micrograph of possible local bonding over the gap in Sample 14.

As in Figure 25, the local bonding area in Figure 27 is between gaps with width of approximately 60 μm. A line scan across the locally bonded area was performed, and can be found in Appendix B. Increased amounts of detected silicon indicate the local area is A356, and the cracks are mainly along the eutectic silicon. Oxygen was detected in the cracks along the insert, which could suggest that there is an oxide layer remaining on the surface.

An area where the gap is only approximately 3 μm is shown in Figure 28.

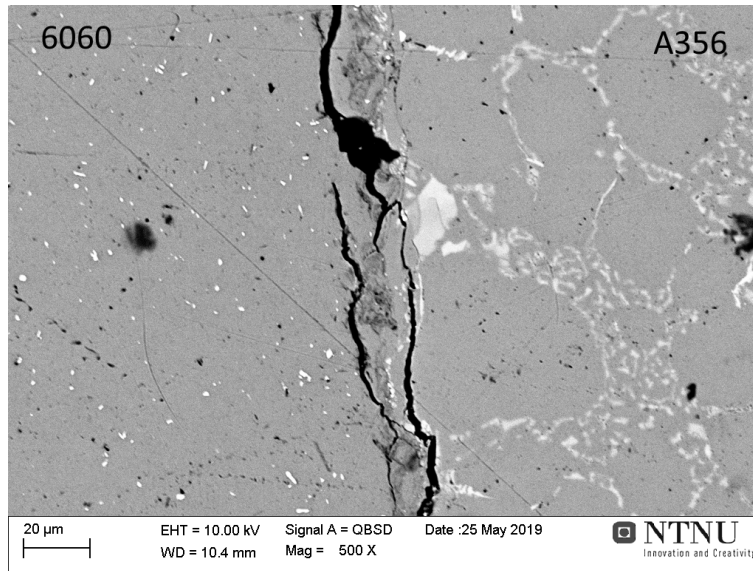
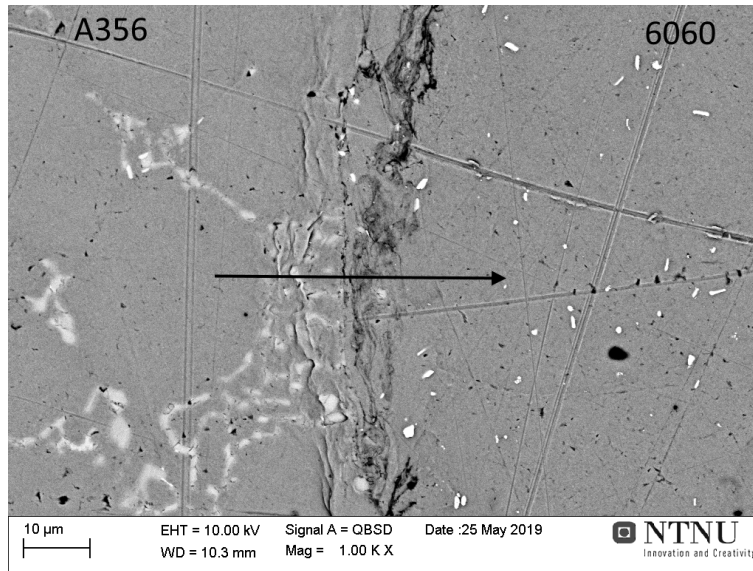


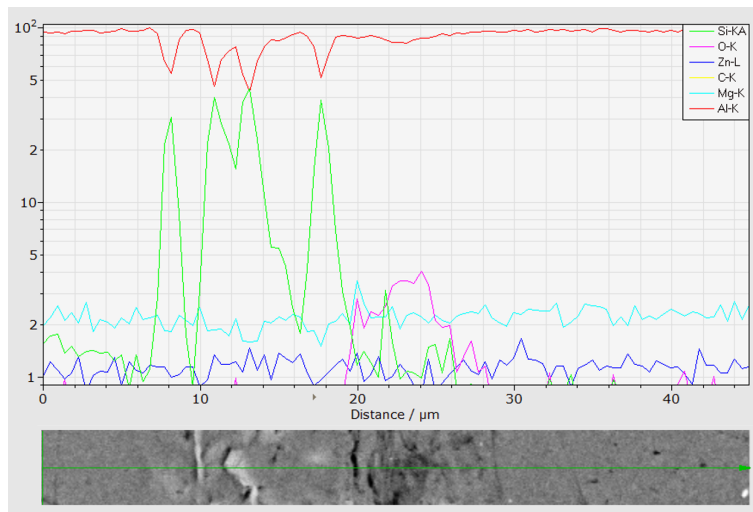
Figure 28: Micrograph showing cracks in both 6060 and A356 along the interface in Sample 13.

Here, the gap not only follows the insert interface, but cracks branch out into the A356. As seen in other areas, cracks in the A356 follow the eutectic silicon. Cracks formed along the interface, most likely as a result of shrinkage, though some melting of the insert is possible. Some bonding was likely achieved before crack propagation.

Another area in Sample 13 with possible melting of the insert, is shown in Figure 29.



(a) Some cracks along an area where the insert likely melted. The arrow indicates where a line scan was performed.



(b) Line scan showing detected elements. The y-axis is logarithmic.

Figure 29: Micrograph of Sample 13, where a line scan was performed across the interface.

No distinct gap is visible along the interface, though there is some cracking in the eutectic silicon. A line scan was performed over the area, indicated by the arrow in Figure 29. The silicon content is higher in A356 compared to 6060, and peaks at the eutectic phase. The drop in detected silicon over an area with increased oxygen indicate where the interface between A356 and 6060 is. The amount of magnesium is relatively constant over the studied area, with one peak at a crack.

Along the interface in Sample 15, the area shown in Figure 30 was found.

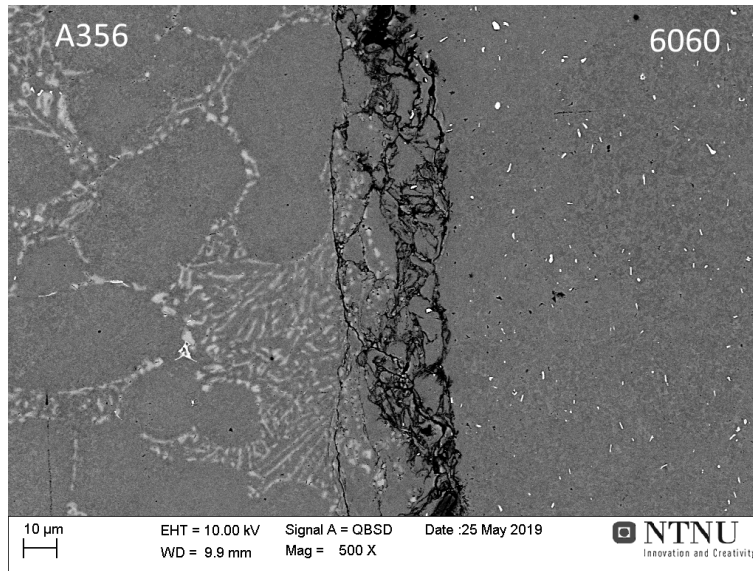


Figure 30: Cracked area along the interface in Sample 15.

The insert interface shows several small cracks in this area, suggesting melting of the insert before cracking as the metal pulled away during solidification. Similarly, cracks can be seen in the A356, both at the interface and approximately 15  $\mu\text{m}$  into the cast part. A line scan across the interface can be found in Appendix B. The magnesium content is slightly higher in 6060 than A356 according to the line scan. Increased amounts of oxygen are present in the cracks.

#### 4.4 High Preheating Temperature

This experiment was conducted with preheating of both insert and mould to 600°C, followed by five minutes holding time in the furnace. Different 6060 insert shapes were used, as described in Table 6.

Table 6: Series description for Experiment 3.

Series	Insert	Samples
3-1	Pipe	16, 17, 18
3-2	Rod	19, 20, 21

##### 4.4.1 Series 3-1: Pipe Inserts

Pipes were used in this series, and for all three samples the A356 melted through the pipe at the inlet. The pipe in Sample 17 was separated during casting, where the upper half was displaced by the melt flow. Large cracks along the inner side of the pipe can be seen in Figure 31. Such cracks did not form in Sample 17 and 18.

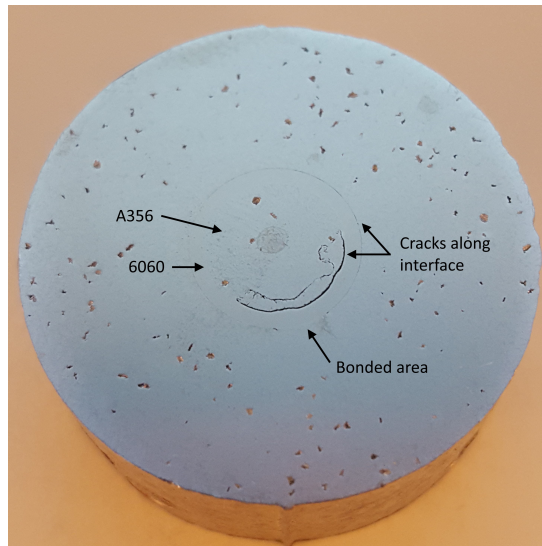


Figure 31: Surface of Sample 16. Cracks formed along the inside of the pipe, and an area where bonding was achieved is indicated.

An optical image, Figure 32, was taken of the area where large cracks formed in the A356.

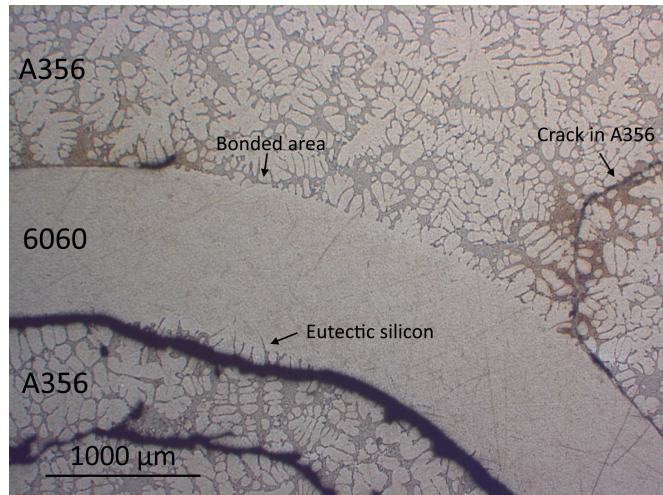
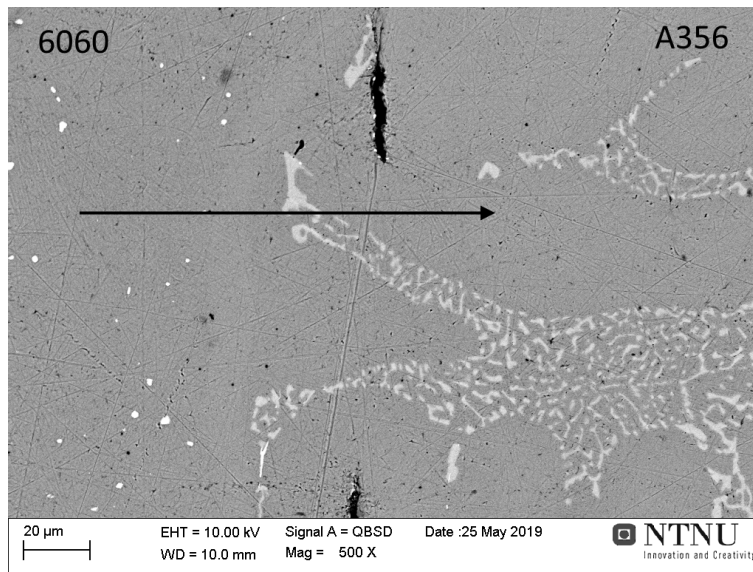


Figure 32: Optical image of the gaps and bonded areas along the pipe insert in Sample 16.

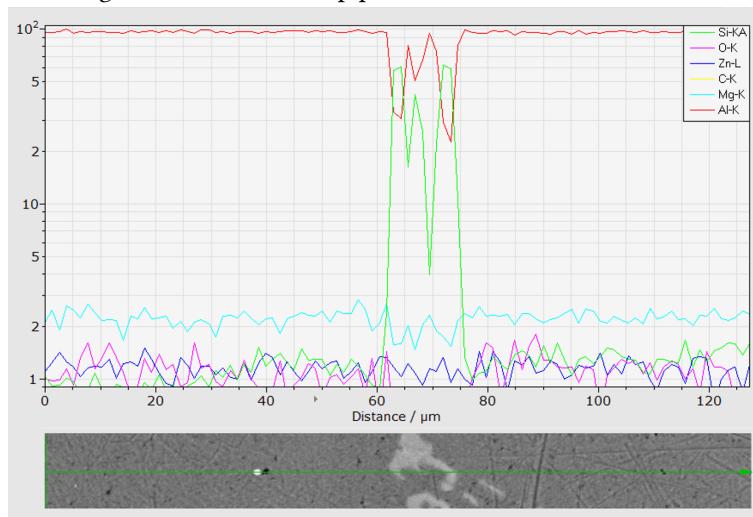
Bonding was achieved along the inside of the pipe for all samples, except along the crack shown in Figure 32. Cavities inside the pipe likely formed during solidification, as the A356 shrank. A local area of bonding can also be seen in the optical image, where the crack cuts through the A356 instead of along the insert.

Opposite to this, on the outer side of the pipe, a relatively long area has achieved bonding. The gap on both sides of this area either branches into the A356 or stops. This was the largest area of bonding observed in all samples, at almost 3 mm.

Along the outside of the pipe, a gap is visible everywhere except the large area shown in Figure 32, and a local area shown in Figure 33. The arrow shows where a line scan was performed.



(a) Locally bonded area along the outer side of the pipe. The arrow indicates where a line scan was performed.



(b) Line scan showing detected elements. The y-axis is logarithmic.

Figure 33: Micrograph of Sample 16, showing local bonding on the outer side of the pipe.

This local area has a 100  $\mu\text{m}$  thick area with no gap, where bonding was successful. During casting, the insert surface most likely melted and bonding was achieved, before cracks formed in the eutectic silicon during cooling.

As shown by the gradual decrease in the line scan, silicon diffused approximately 20  $\mu\text{m}$  into the 6060. The amount of magnesium detected over the bond was continuous, with a slight decrease at the eutectic silicon. In addition, some oxygen was detected over the bond.



Cracks were continuous along the outer interface of the pipe in Sample 17 and 18. These were generally narrow, approximately 6  $\mu\text{m}$  at the widest, and mainly followed the insert. As seen in Figure 34, cracks also formed in the A356. This suggests bonding prior to fracture in the eutectic silicon.

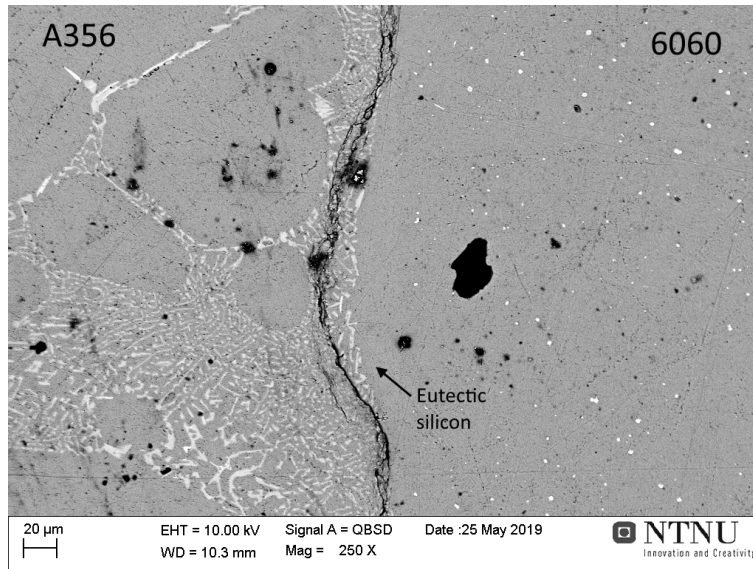


Figure 34: Micrograph of Sample 17, showing a narrow gap through eutectic silicon in the cast aluminium.

The gap divides the eutectic silicon, possibly due to silicon expanding while aluminium shrinks during solidification. This would lead to stresses in the area, resulting in fracture. Aluminium melt with higher amounts of alloying elements, i.e eutectic silicon, is the last to solidify. Thus, stronger bonding might have formed before the eutectic silicon solidified.

Bonding was achieved on the inside of all pipes in this series, and an example of such an area can be seen in Figure 35. The only exception was cracks in Sample 16, as was shown in Figure 32.

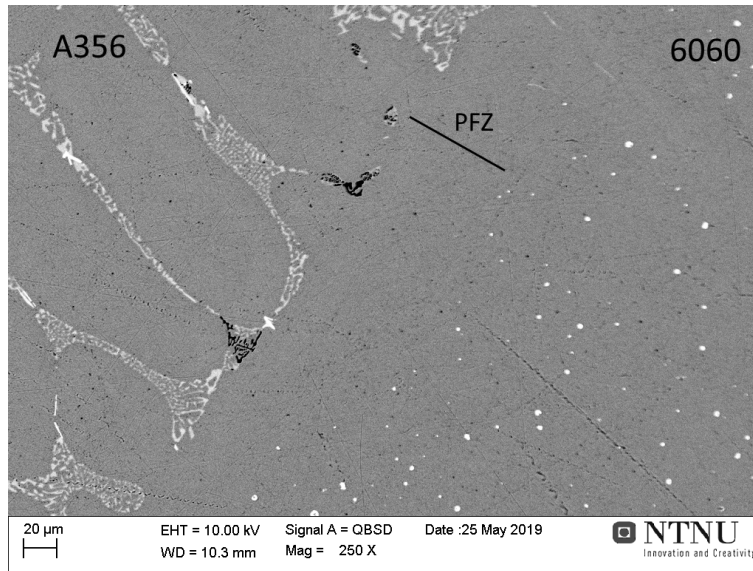


Figure 35: Micrograph of bonded area inside the pipe, taken from Sample 17. Between the insert and cast aluminium is a precipitation free zone.

The insert surface likely melted before bonding was achieved. Figure 35 shows an approximately 80 µm wide area between the A356 and 6060 with no visible phases. A line scan was performed over a similar reaction zone, with results in Appendix B. The amounts of detected silicon decreases from A356 to 6060 across the line. Precipitation free zones mainly form due to the liquid aluminium solidifying too rapidly for precipitates to form.

As 6060 has higher thermal expansion compared to A356, the insert does not shrink away from the cast aluminium on the inside of the pipe to the same degree on the outside. Bonding on the inside of the pipe is thus expected to be achieved more easily compared to on the outside.

#### 4.4.2 Series 3-2: Rod Inserts

Rods were used for this series, as can be seen in Figure 36. Large pores, due to slower solidification, are visible on the surface of Sample 20.

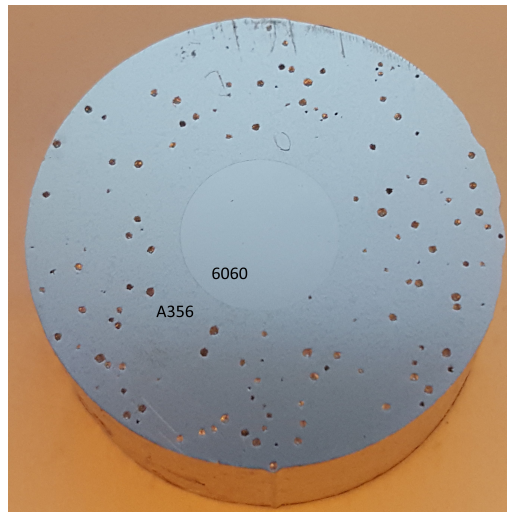


Figure 36: Surface of Sample 20, with no visible gap between the insert and cast aluminium.

Though not visible in the image, a gap is present between the insert and cast aluminium. It is generally narrow, varying from approximately 1  $\mu\text{m}$  to 15  $\mu\text{m}$ . Mainly, the gap follows the insert surface, but is in some areas observed to cut through the A356. This is shown in Figure 37.

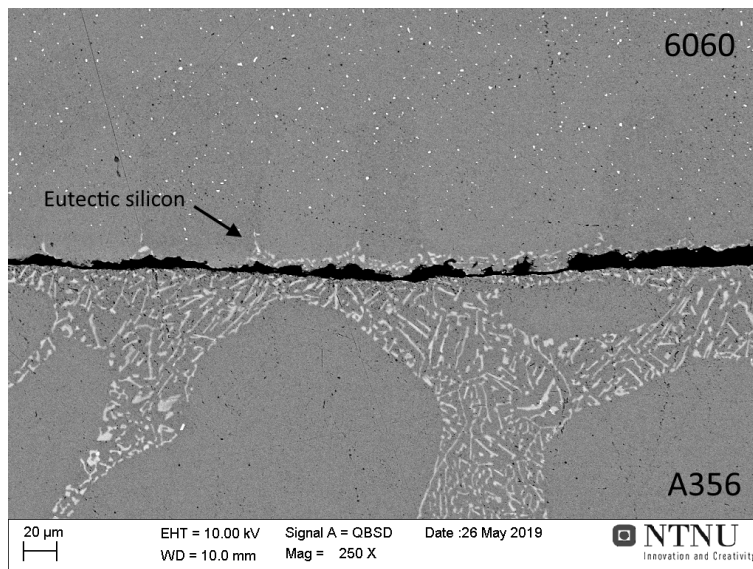


Figure 37: Micrograph of the gap going through eutectic silicon in Sample 21.

The precipitation free zone in Figure 34 is not uniform, as was previously observed in the bonded area in Series 3-1. Bonding was successful between A356 and 6060, but shrinkage caused fracture in the eutectic silicon. This also happened along an area in Sample 19, shown in Figure 38.

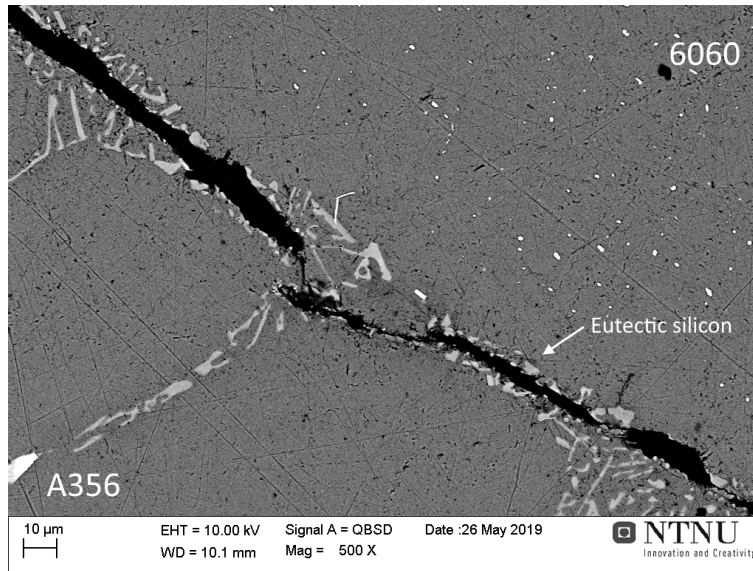


Figure 38: Micrograph of Sample 19, showing the gap formed in the cast aluminium.

A precipitation free zone of approximately 20 µm can be seen between the two alloys, where bonding was successful. Shrinkage caused fracture in the eutectic silicon, resulting in the approximately 10 µm wide gap.

All samples in the series had one or two local areas of bonding. One of these is shown in Figure 39.

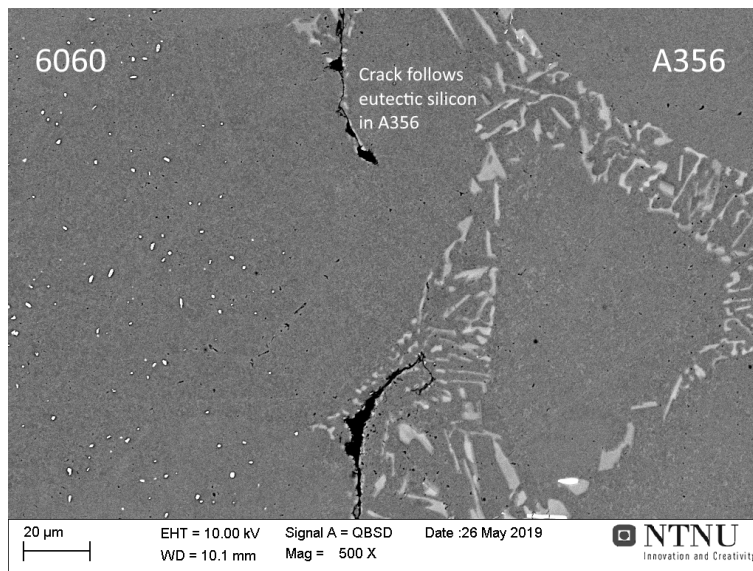


Figure 39: Micrograph of locally bonded area in Sample 19. The cracks follow the eutectic silicon.

The cracks on both side of the bonded area follow the eutectic silicon in A356. The precipitation free zone is approximately 20 µm wide in this area as well.

## 4.5 Simulation in StaMiSim

Results for simulations with the software StaMiSim were provided by IFE. Temperature, solid fraction, principal stresses and air gaps during solidification were simulated. Visualisations of the results are presented in Appendix D.

For Series 3-1, the simulation of solid fraction during casting revealed melting of the pipe. Figure 40 shows the solid fraction at 10 s and 30 s.

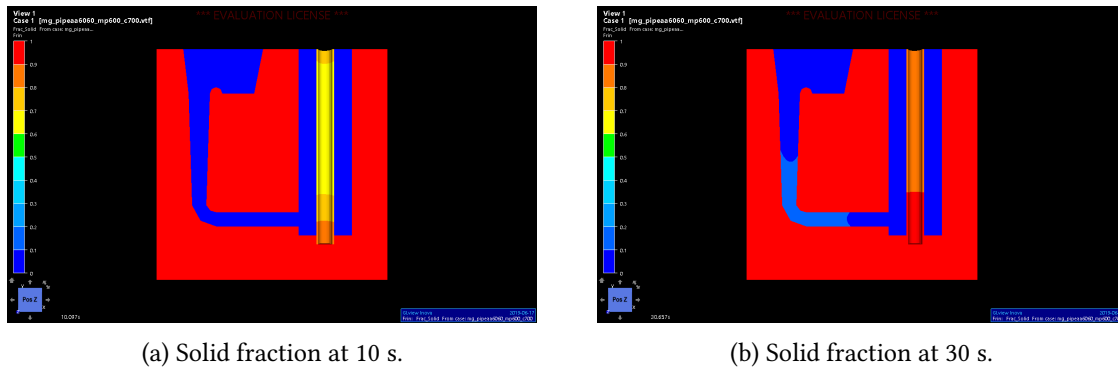


Figure 40: Simulation results showing solid fraction in Series 3-1. The pipe melted within 10 s, and had become solid again within 30 s.

The lowest solid fraction, at 10 s, was 0.6 - 0.7 for the pipe. Some melting was also seen for the rod in Series 3-2, as the simulation revealed a solid fraction of 0.8 - 0.9 after 10 s.

Results for the principal stress and air gap in Series 3-2 are shown in Figure 41 and 42 respectively.

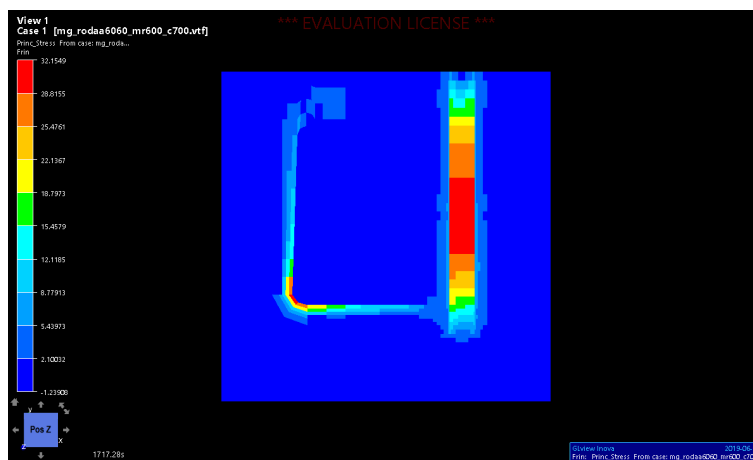


Figure 41: Simulation results for first principal stress in Sample 3-2 after 28.5 min.

The figures show a correlation between the high principal stress and where air gaps will form. The stress was observed to increase over time, with a maximum after 28.5 min. This was thus also the maximum for the air gap simulation.

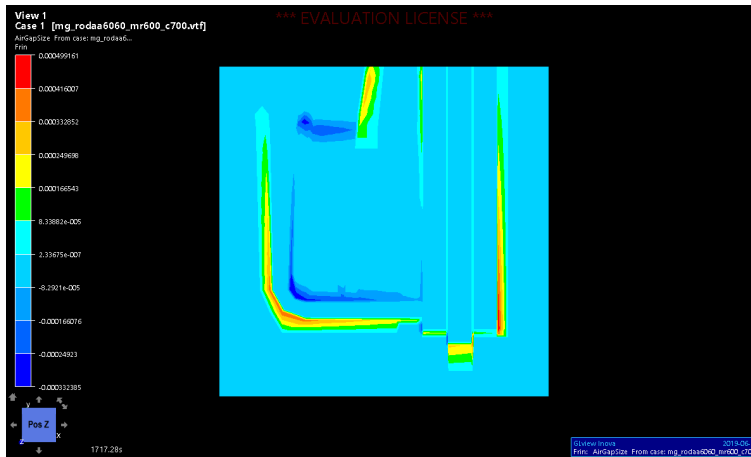


Figure 42: Simulation results for air gaps in Sample 3-2 after 28.5 min.

Another noteworthy observation from the solid fraction simulations was the direction of solidification, which started at the mould walls and completed along the insert in all cases shown in Appendix D.

## 5 Discussion

In this thesis, the effect of zinc coating and various preheating temperatures of the mould and 6060 aluminium inserts on the metallic bonding of compound casting between A356 and 6060 was studied. The experiments were chosen as continuations of the specialisation project in the course TMT4500.

Multiple pores are visible on the sample surfaces. Turbulent flow during mould filling could entrap air and oxides in the melt, leading to pores and cavities after solidification. Entrapment of air in the gating was captured by the mould filling simulation in SutCast, and can be seen in Figure 7. In addition, shrinkage of the aluminium upon cooling can increase the size of the pores. More pores are observed in the samples with higher process temperatures. Improved flowability increases turbulence and thus the amount of oxides entrapped in the melt. Altering the mould design or use of inert gases, such as argon, in the mould or melt can reduce pores. However, pore reduction is not crucial for the results in this thesis.

Due to solid aluminium occupying less space than the liquid, a cavity will form in the last volume to solidify inside a cast part. Gaps between the insert and cast aluminium were observed in most samples by visual inspection without a microscope. The formation of such gaps is also due to the shrinkage of aluminium during solidification. A356 will solidify at the mould walls and insert first, due to the temperature difference. It is then pulled away by the solidifying melt. This was seen in simulations with StaMiSim. Thermal expansion in solid state also contribute to gap formation and growth, as 6060 has a higher thermal expansion coefficient compared to A356. The insert will expand as it is heated, but shrink more than the cast aluminium during cooling. The gap will thus be broadened. Bonding must be strong enough to withstand the shrinkage, otherwise cracks will form.

All images showing sample surfaces were taken from the direction of flow into the mould cavity. In all samples where a wide gap was visible, this was located on the opposite side of the inlet. The large cracks along the inside of the pipe in Sample 16 were located at the same side as the inlet.

The three experiments conducted as part of this thesis will be further discussed separately.

### 5.1 Effect of Zinc Coating

Before casting, the preheating temperature for Experiment 1 was decided after simulation of the casting process. Process data used for simulation was approximate, due to lack of accurate heat transfer coefficients for the mould. The results were thus also approximate, and only used as a guide when deciding the preheating temperature.

Three series were cast with zinc coated inserts. Different parameters were used during the coating process, to get various zinc layer thicknesses. It is believed that the zinc layer in Series 1-1 was the thinnest and Series 1-3 thickest based on the process parameters. However, due to the poor bonding, this could not be verified. In previous studies, it was observed that a zinc layer thickness of less than 1  $\mu\text{m}$  was insufficient to achieve bonding, and a thickness of 5-10  $\mu\text{m}$  is therefore commonly used [4]. To determine the thickness of the zinc layers in this experiment, an unused pipe from each coating procedure was studied in SEM with EDS. When studying the edge of the pipe surface directly from

above, no distinct zinc layer was observed. This suggests that only a thin layer, with less than 5  $\mu\text{m}$  thickness, had been applied. The sample was then tilted and the coated outer side of the pipe was micrographed. This was shown for Series 1-1 in Figure 10. The coating surface is uneven, with visible impurities. Dark contrast is believed to be holes in the coating layer. EDS mapping of the zinc layer showed mainly carbon and oxygen, but also small amounts of aluminium, silicon, zinc and magnesium. This suggests that the surface is not completely covered by the zinc layer, thus not protecting the aluminium from reoxidising. Micrographs and EDS mapping showed similar results for the pipes that were zinc treated with applied current. Successful bonding with a thin zinc layer,  $\leq 1 \mu\text{m}$ , was reported by Koerner et al [23]. The importance of a sound bonding between the zinc layer and oxide-free aluminium surface was emphasised, and the zincate treatment was performed twice to improve coverage. Therefore, the coating process in these experiments should be optimised in order to obtain a uniform zinc layer that covers the complete aluminum surface.

After casting, zinc was detected continuously in the 6060 alloy along the interface for all studied samples in this experiment. Most likely, the zinc diffused into the 6060 during preheating, leaving less zinc at the surface to dissolve in the A356. This would leave the aluminium surface vulnerable to reoxidation, and thus obstruct bonding. The zinc layer being washed away by, or melting and dissolving into, the aluminium melt during casting is also possible, but few areas with zinc detected in the A356 were observed. EDS line scans were performed at the inner side of pipes used for casting, one for each series. This side of the pipes had not been in contact with A356, so the zinc layer could not have been washed away by, or dissolved into, the melt. The line scans detected zinc as an approximately 20  $\mu\text{m}$  wide diffusion zone in the 6060. Such a zone was not observed for the unused pipes. The effect of preheating on the zinc layer should be studied further, to understand if preheating of coated inserts should be avoided. Thermal data obtained from thermocouples during casting show the temperature inside the pipe was above the melting temperature of zinc for approximately 30 s. The graphs can be found in Appendix C. Any zinc remaining on the surface would then have dissolved into the melt. Bonding was expected to be improved with increasing thickness of the zinc layer. Results from this experiment show no such correlation, as no proper bonding was achieved for any of the series. Gaps between the insert and cast aluminium were seen when looking at the sample surfaces without a microscope. Areas of interest were found with SEM in all samples though, and were similar regardless of coating procedure.

Areas where the cast aluminium remained in contact with the insert, indicate local bonding that likely was broken upon solidification due to shrinkage. These locally bonded areas might have formed as a result of variations in the zinc coating or oxide layer. It was also in these areas that zinc was detected in the A356 alloy. This was shown in Figure 14. Remaining coating on the insert surface in this area could have lead to local bonding. As the cast aluminium shrank during cooling, the local bond likely would have broken, but zinc remain at the A356 surface. No intermetallic phases containing zinc were observed in either A356 or 6060.

Figure 18 and 21 show areas with multiple cracks along the interface. However, the contrast in the micrographs suggests that no bonding occurred in these areas. Parts of the insert appears to have detached and settled in the A356. The temperature graph shows that the mould temperature during casting did not reach solidus for 6060 aluminium, at 610°C. Thus melting of the insert is unlikely.



## 5.2 Preheating of Mould or Insert

To further understand the shrinkage of the cast aluminium in the mould, casting was done with a large temperature difference between the insert and mould. One was kept at room temperature, while the other was preheated to 600°C. Due to the mould design, reassembly of the mould was required when placing the insert. This was done in approximately two minutes. When the hot insert was placed in the relatively cold mould, the insert started to cool. No significant increase in the mould temperature was detected by the thermocouples before pouring, as can be seen in the temperature graph for Series 2-1 in Appendix B. When the hot mould was removed from the furnace and the relatively cold insert placed inside, the temperature dropped approximately 150°C according to the temperature graph for Series 2-2, also in Appendix B. It is assumed that the pipe was heated by the mould before pouring. Thus the temperature difference between the insert and mould was not as high as desired. For a greater effect, a new mould should be designed where placement of the insert is easier.

Without preheating of the mould, the mould walls are the coldest surface and it is therefore expected that solidification would start there. Thus, it is possible to achieve a more directional solidification towards the insert, which would allow for contact between the insert and cast metal to remain for a longer period of time. This could increase chances of bonding, and it was therefore expected to observe better bonding or a thinner gap when only the insert was preheated. Solidus for the 6060 alloy is 610°C, which is just above the preheating temperature. The aforementioned factors would improve bonding at the interface, but no preheating of the mould resulted in low overall process temperatures. Flowability of A356 was reduced significantly, with form filling being worst for Series 2-1. Lower process temperatures also increase the solidification rate, reducing bonding time. The insert expands more when preheated to a higher temperature, and thus shrinks more when cooled.

For Series 2-2, the gap was expected to be wider compared to Series 2-1. As the melt filled the mould cavity, solidification likely started at the insert, as this was the coldest surface. The A356 would then shrink towards the mould walls as remaining melt solidified. Any bonding would have had to form prior to this initial gap formation. By comparing the temperature data, it can be seen that the process temperature was higher for Series 2-2 compared to Series 2-1. Flowability of the melt improved greatly, and solidification should be slower due to higher temperatures. Slower solidification grants more time for bonding and potentially melting of the insert surface. The insert would have been heated after placement in the mould, but not necessarily enough for the surface to be melted by the liquid aluminium during casting. This could not be verified, as temperature data for the pipes were not recorded. However, areas along the interface appeared to have melted, as shown in Figure 28, 29 and 30, suggesting the temperature exceeded 610°C in certain areas. Heating of the insert to approximately the same temperature as in Series 2-1 results in approximately the same shrinkage effect of solid 6060 during cooling.

The results differed less than expected between the two series. This was likely due to the mould assembly causing a reduction in the temperature difference, both between the insert and mould and the two series. Wide gaps were observed in both series. The gap in Series 2-1 was generally longer, while the widest gap was observed in Series 2-2.

Successful bonding was not expected for this experiment, nor was it observed. There had been no surface treatment of the inserts to handle the oxide layer, and the process temperatures were low. The purpose of this experiment was not to achieve bonding, but to study the effect of preheating the

insert and mould.

### 5.3 Effect of High Temperature

Different inserts were used during casting at preheating temperatures of 600°C, and the mould remained in the furnace for five minutes after filling. Only rods were used in the preliminary project, and it was suggested to also use pipes for further work. The effect of the difference in shrinkage between A356 and 6060 should be less when using a pipe, as it has less mass compared to a rod. Also, heat transfer should be slower through the pipe due to the relative mass.

Once the melt reached the pipes during pouring, it melted through and filled the pipes with aluminium. Due to issues with the temperature logger for the thermocouples, no temperature data was recorded until the mould was removed from the furnace, and the temperature during mould filling was thus not obtained. However, due to the inserts melting, the temperature must have been above the 6060 liquidus, 660°C. The surface on the inside of the pipes likely also melted, and successful bonding was observed on the inside of all inserts in Series 3-1. With A356 on the inside of 6060 pipes, the effect of differing thermal expansion coefficients is reduced. Upon solidification the pipe will likely contract, thus separating it from the cast aluminium surfaces. On the outside of the pipe, the alloys will thus shrink in opposite directions. The cast aluminium inside the pipe will shrink less than the pipe itself, which should result in less tension at the interface. Heat transfer is slower for the melt inside the pipe, and it will solidify slowly. Less shrinkage and slower solidification are factors likely improving bonding on the inside of the pipes.

Bonding on the inside of the pipes was achieved without surface treatment of the inserts. No distinct oxide layer was detected by the line scan over the bonded area, results of which are found in Appendix B. Oxygen is detected uniformly across the area. The aluminium oxide layer would not have melted, due to its high melting temperature. Though as the insert surface melted, the aluminium oxide likely detached and was distributed in the liquid, thus oxygen remained across the bond.

Through optical- and electron microscopes, successful bonding on the inside of the pipes was observed in all areas except along the large cracks shown in Figure 32. Shrinkage in the cast aluminium trapped on the inside of the pipe would lead to cavities. Variations in the oxide layer might have prevented bonding, thus resulting in gap formation along the interface. Eutectic silicon can be seen on both sides of the gap in Figure 32. As the eutectic silicon is characteristic for the A356 alloy, the observation suggests that bonding formed in this area and that the gap formed during solidification. The bonding in this local area was thus stronger than the eutectic silicon phase through which the crack grew.

A large area on the outside of the pipe in Sample 16 achieved bonding. This was along the side of the insert facing the inlet, where the melt likely washed the insert surface and possibly removed some of the oxide layer.

The interface on the outer side of the pipes in Series 3-1 showed similar results as the interface around the rods in Series 3-2. In Series 3-1, the outer interface was mostly defined by a continuous crack. However, in certain areas the crack propagated through the eutectic silicon in A356, suggesting that there had been a bond between the A356 and 6060 alloy. Multiple examples of this were observed in Series 3-2. Along these areas, bonding between the two alloys was strong, causing stress induced

fracture in the eutectic silicon instead. The cracks at the locally bonded areas clearly follow the eutectic silicon, and do not propagate in the aluminium grains. Propagation of cracks along the eutectic silicon might be due to higher alloyed aluminium melt solidifying at lower temperatures. As can be seen in the Al-Si phase diagram, Figure 2, melt at eutectic composition will be the last to solidify during cooling. An uneven precipitation free zone can be seen between the insert and cast aluminium, where bonding is believed to have formed. Since both A356 and 6060 are heat treatable, heat treatment is necessary to further increase the strength of the compound casting. A systematic study on the microstructure evolution at the interface during solution heat treatment and age hardening treatment is suggested for future work.



## 6 Conclusions

Three different compound casting experiments were conducted as part of this thesis. For the first experiment, a zinc layer was applied to inserts by different coating procedures. The effect of the coating thickness was to be studied. The zinc layer before casting was uneven and reoxidation of the aluminium surface had to be expected. After casting, zinc was detected as a diffusion zone in the 6060. Few areas were observed where zinc had been washed by the melt and dissolved into the A356. The diffusion was likely during the preheating of the insert, and further work would be to study the effect of preheating on the zinc layer. Especially no preheating of the coated insert would be interesting. The results did not vary as much as expected, though the thickness of the zinc layer varied for the different coating procedures. The quality of the coatings were not good enough to achieve sound bonding in any of the samples. The importance of thorough oxide removal and application of a uniform coating became evident in this experiment.

The effect of preheating the insert or mould was studied in Experiment 2. Preheating of either the insert or mould was done, while keeping the other at room temperature. Due to the mould requiring reassembly when placing the insert, the temperature difference between the insert and mould was not as large as planned. Results for the two series were more similar than expected, likely due to this reduced temperature difference. Some melting of the insert surface was observed, but no bonding remained after shrinkage during solidification. To better study the effect of preheating, the mould should be designed with that purpose in mind.

The final experiment was conducted at high preheating and holding temperatures. The inserts in this experiment had not been surface treated, nevertheless, successful bonding was achieved on the inside of the pipes. Aluminium oxide would not have melted at the casting temperatures used in this experiment. As the insert surface melted though, the oxide layer detached and distributed into the melt. Higher tensile stresses on the outside of the pipes caused cracks to form along the interface. Similar areas were observed along the rods as on the outer side of the pipes. Cracks formed along eutectic silicon in the cast aluminium, possibly due to this phase solidifying last. Bonding between the A356 and 6060 was thus originally achieved, but shrinkage caused cracks to form, resulting in weak compound cast parts.

Simulation software was used to describe a theoretical casting process. SutCast was used prior to casting, to determine suitable preheating temperatures for Experiment 1. The process data used was not accurate, and should be improved for further work. The temperature data collected by the thermocouples could be used for calculation of a more accurate heat transfer coefficient in the mould.

Mechanical bonding could be constructed by compound casting, but many problems arise when attempting to achieve metallurgical bonding. The stable oxide layer, shrinkage during solidification and consequent crack propagation must be overcome for two aluminium alloys to be successfully joined by compound casting.



## References

- [1] Jean-Paul Rodrigue. *The geography of transport systems*. eng. London, 2006.
- [2] D. Berjoza and I. Jurgena. 'Effects of change in the weight of electric vehicles on their performance characteristics'. In: *Agronomy Research* 15.1 (2017), pp. 952–963. ISSN: 1406894X.
- [3] Rajender Kumar Tayal et al. 'COMPOUND CASTING - A LITERATURE REVIEW'. In: *Proceedings of the National Conference on Trends and Advances in Mechanical Engineering* (2012), pp. 501–510.
- [4] K.J.M. Papis et al. 'Interface formation in aluminium–aluminium compound casting'. In: *Acta Materialia* 56.13 (2008), pp. 3036–3043. ISSN: 1359-6454.
- [5] William D Callister. *Materials science and engineering*. eng. Hoboken, N.J, 2015.
- [6] Jan Ketil Solberg. *Teknologiske metaller og legeringer*. nor. Trondheim, 2017.
- [7] Nikolay A. Belov, Dmitry G. Eskin and Andrey A. Aksenov. 'Chapter 2 - Alloys of the Al–Mg–Si–Fe System'. In: *Multicomponent Phase Diagrams*. Ed. by Nikolay A. Belov, Dmitry G. Eskin and Andrey A. Aksenov. Oxford: Elsevier, 2005, pp. 47–82. ISBN: 978-0-08-044537-3.
- [8] Vladimir Tsepelev, Vladimir Vyukhin and Arkadi Povodator. 'The Unit for Determining the Density and Surface Tension of Metallic Liquid Alloys, Using the Sessile Drop Method'. In: *Materials Science Forum* 889 (2017), pp. 108–112. ISSN: 02555476.
- [9] Kock-Yee Law and Hong Zhao. *Surface Wetting*. eng. 1st ed. 2016. Springer Verlag, 2016. ISBN: 3319252127.
- [10] Gianni Nicoletto, Radomila Konečná and Stanislava Fintova. 'Characterization of microshrinkage casting defects of Al–Si alloys by X-ray computed tomography and metallography'. In: *International Journal of Fatigue* 41 (2012). Fatigue Design & Material Defects, pp. 39–46. ISSN: 0142-1123.
- [11] MakeItFrom.com. *356.0-F Cast Aluminum*. 2018. URL: <https://www.makeitfrom.com/material-properties/356.0-F-Cast-Aluminum> (visited on 06/12/2018).
- [12] J-H. Zhao et al. 'Joining of arc sprayed coating to substrate by compound casting'. eng. In: *Surface Engineering* 31.1 (2015), pp. 58–63. ISSN: 0267-0844.
- [13] H Baker and H Okamoto. *ASM Handbook. Vol. 3. Alloy Phase Diagrams*. eng. 1992. ISBN: 0871703815.
- [14] MakeItFrom.com. *6060 (AlMgSi, 3.3206, A96060) Aluminum*. 2018. URL: <https://www.makeitfrom.com/material-properties/6060-AlMgSi-3.3206-A96060-Aluminum> (visited on 06/12/2018).

- [15] Allan Blackman. *Aylward and Findlay's SI Chemical Data*. eng. Milton, 2014.
- [16] S Bao et al. 'WETTABILITY OF ALUMINIUM ON ALUMINA'. eng. In: *Metallurgical and Materials Transactions B: Process Metallurgy and Materials Processing Science* 6 (2011), pp. 1358–1366. ISSN: 1543-1916.
- [17] Matthias Schwankl et al. 'The influence of sandblasting on the morphology of electroless deposited zinlayers on aluminum sheets'. In: *Applied Surface Science* 283 (2013), pp. 202–208. ISSN: 0169-4332.
- [18] Esther T. Akinlabi, Enoch Ogunmuyiwa and Stephen A. Akinlabi. *Characterising the Effects of Sand Blasting on Formed Steel Samples*. 2013.
- [19] Stephen F. Rudy. 'Pickling and acid dipping'. In: *Metal Finishing* 100 (2002), pp. 173–179. ISSN: 0026-0576.
- [20] J. Garcia, C. Massoulier and Ph. Faille. 'Brazeability of Aluminum Alloys Containing Magnesium by CAB Process Using Cesium Flux'. In: *Vehicle Thermal Management Systems Conference & Exposition*. SAE International, 2001.
- [21] Jian Feng et al. 'Bonding of Aluminum Alloys in Compound Casting'. In: *Metallurgical and Materials Transactions A* 48.10 (2017), pp. 4632–4644. ISSN: 1543-1940.
- [22] D.O. Flamini, S.B. Saidman and J.B. Bessone. 'Electrodeposition of gallium and zinc onto aluminium. Influence of the electrodeposited metals on the activation process'. In: *Thin Solid Films* 515.20 (2007), pp. 7880–7885. ISSN: 0040-6090.
- [23] Carolin Koerner, Matthias Schwankl and David Himmler. 'Aluminum–aluminum compound castings by electroless deposited zinc layers'. In: *Journal of Materials Processing Technology* 214.5 (2014), pp. 1094–1101. ISSN: 0924-0136.
- [24] Hui Zhang, Yiqing Chen and Alan A. Luo. 'Removing the oxide layer on the A380 substrate of AM60/A380 bimetallic castings by the zincate process followed with galvanizing'. eng. In: *Vacuum* 148 (2018), pp. 127–130. ISSN: 0042-207X.
- [25] Matthias Schwankl, Jonathan Wedler and Carolin Körner. 'Wrought Al - Cast Al compound casting based on zincate treatment for aluminum wrought alloy inserts'. In: *Journal of Materials Processing Technology* 238 (2016), pp. 160–168. ISSN: 0924-0136.
- [26] M. Rübner et al. 'Aluminium–aluminium compound fabrication by high pressure die casting'. In: *Materials Science and Engineering: A* 528.22 (2011), pp. 7024–7029. ISSN: 0921-5093.
- [27] Teng Liu et al. 'An investigation into aluminum–aluminum bimetal fabrication by squeeze casting'. In: *Materials & Design* 68 (2015), pp. 8–17. ISSN: 0261-3069.
- [28] Jarle Hjelen. *Scanning elektron-mikroskopi*. nor. Trondheim, 1989.



- [29] SUTCAST. *Frequently Asked Questions*. 2019. URL: <http://www.sutcast.ca/faq/overview.aspx> (visited on 29/04/2019).
- [30] John O. Dow. 'Lesson 13 - Elements of the Finite Difference Method'. In: *A Unified Approach to the Finite Element Method and Error Analysis Procedures*. San Diego: Academic Press, 1999, pp. 317–349. ISBN: 978-0-12-221440-0.
- [31] D. Mortensen et al. 'Macrosegregation modelling of DC-casting including grain motion and surface exudation'. In: Minerals, Metals and Materials Society, 2014, pp. 867–872. ISBN: 9781118889084.



# Appendix A

This section includes process data for simulations in SutCast.



## SIMULATION INPUT

Project Name: Thesis\_SG19  
 Date: 16.06.2019 22:53:14  
 Description: 1\_Zn, Pipe/mould 250 oC

No	Filling	Solidification
1	Yes	Yes

Saving Data:

From	To	Step	Type
0	100	2	Filling Percent(%)
0	100	1	Solidification Percent(%)
0	200	1	Solidification Time(s)

Materials:

Filling Base Material:A356

No	Name	Material	Initial Temperature (°C)
1	hole	Face Ver	200
2	lid	face up	200
3	pouring	face up	200
4	castpart	A356	700
5	insert	6063	250
6	mould	GraphiteDag	250
7	gate	A356	700

Inlets:

No	Name	Location (mm)	Direction	Type
1	Inlet1	69.93,0.47,131.75	Z-	FillingTime

Filling Time = 4

Options:

Filling Heat is On

Ambient Temperature:200 (°C)

Solidification Stop Type:Solidus

Interfaces:

No	First Object	Second Object	Heat Transfer Coefficient
1	castpart	mould	Graphite-A356
2	gate	castpart	Full Contact
3	gate	mould	Graphite-A356
4	insert	castpart	BASE COATING
5	insert	mould	H13 mold-H13 mold

External Boundary Conditions:

Name	Type	Heat Transfer Coefficient	Environment Temperature (°C)	Constant Temperature (°C)
Left	Convection	Face Ver	200	---
Right	Convection	Face Ver	200	---
Front	Symmetry	---	---	---
Back	Convection	Face Ver	200	---
Bottom	Convection	face down	200	---
Top	Convection	face up	180	---

General Internal BC:

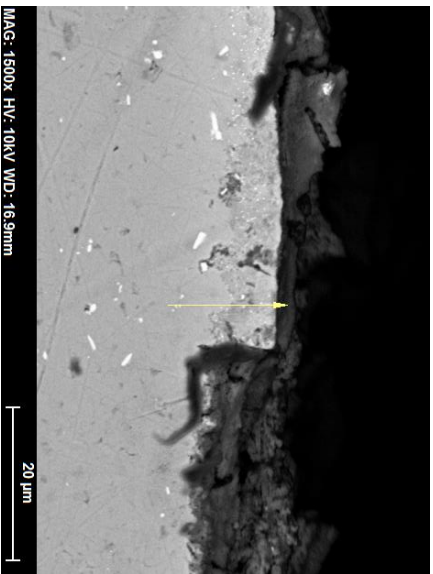
NoSlip



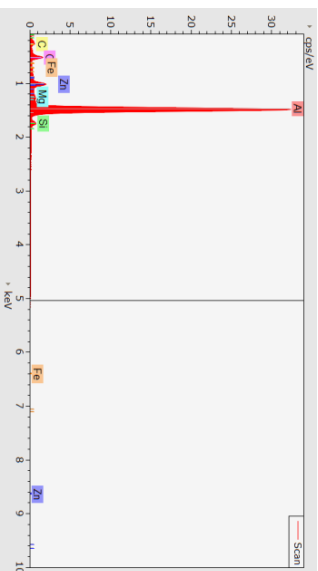
## **Appendix B**

Further details for relevant EDS analyses are included in the following pages.

## Series 1-1, Sample 2



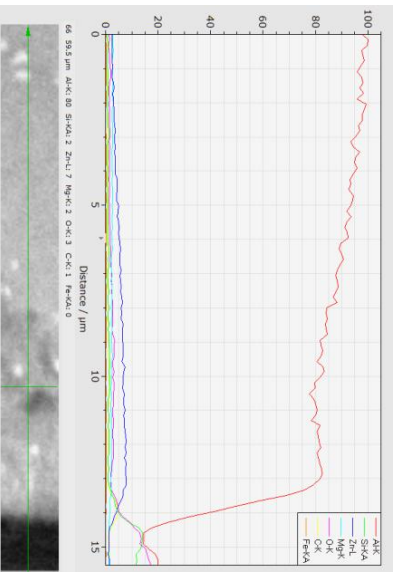
Micrograph with line scan indicated by the arrow



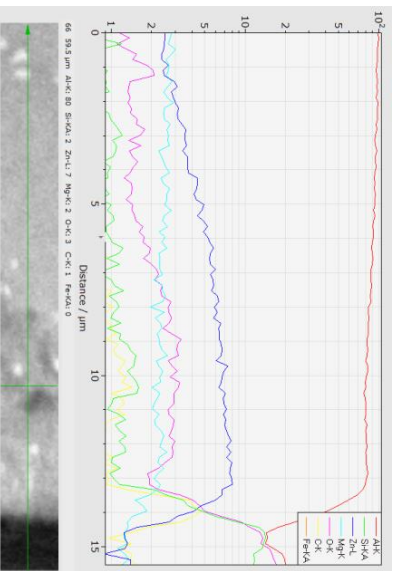
EDS Spectrum

Results table							
Element	AN	Series	Net	Mass C, norm. C	Atom C, Error (1 Sigma)		
			[wt.%]	[wt.%]	[at.%]	[wt.%]	
C	6	K series	22402	8.69	9.12	18.22	1.13
O	8	K series	63212	7.12	7.48	11.22	0.85
Mg	12	K series	27116	1.02	1.07	1.06	0.08
Al	13	K series	1792219	69.22	72.66	64.63	3.12
Si	14	K series	36351	2.60	2.73	2.33	0.13
Fe	26	K series	0	0.00	0.00	0.00	0.00
Zn	30	L series	98816	6.62	6.95	2.55	0.43
<b>Total</b>			<b>95.28</b>	<b>100.00</b>	<b>100.00</b>		

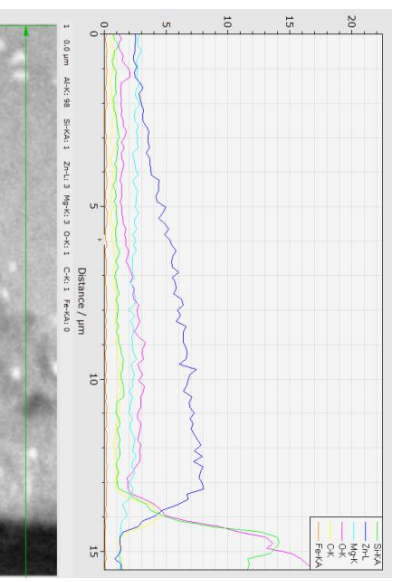
Quantification of spectrum results



EDS line scan results

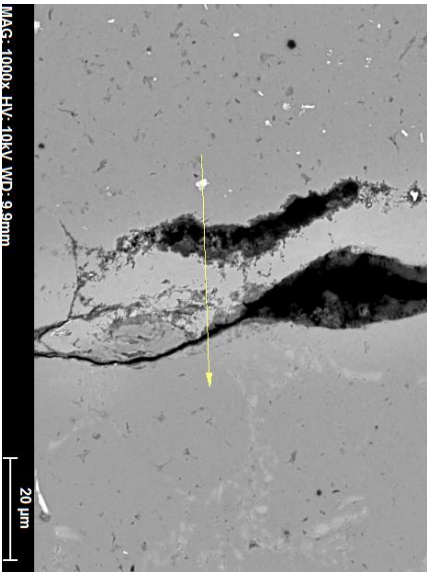


Line scan with logarithmic scale

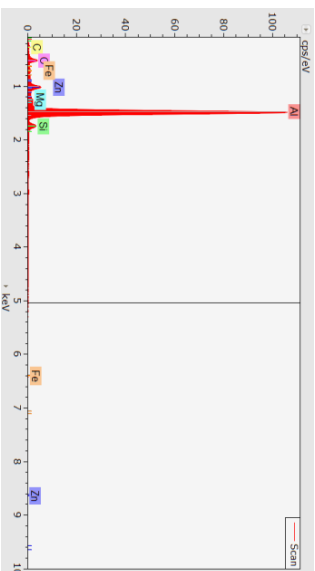


Line scan without aluminium

### Series 1-1, Sample 3



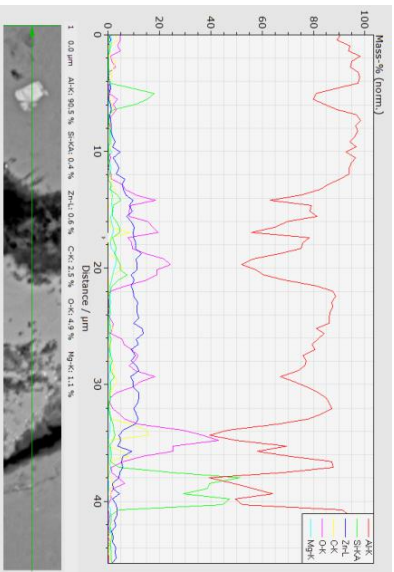
Micrograph with line scan indicated by the arrow



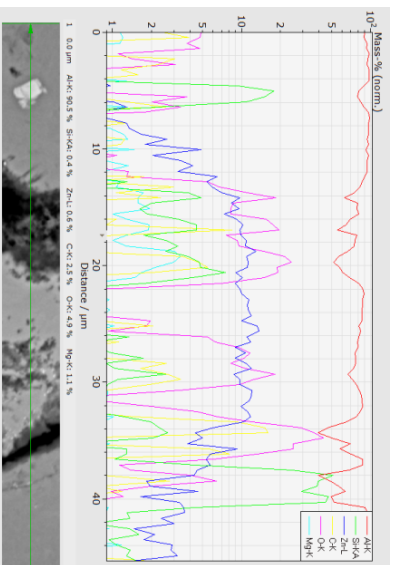
EDS Spectrum

Results table						
Element	AN	Series	Net	Mass C, norm. C, [wt.%]	Atom C, [at.%]	Error (1 Sigma) [wt.%]
C	6	K series	2166	3.51	3.76	8.14
O	8	K series	12420	5.28	5.67	9.20
Mg	12	K series	6535	0.95	1.02	1.09
Al	13	K series	481048	71.57	76.86	74.00
Si	14	K series	15099	4.23	4.54	4.20
Fe	26	K series	554	1.79	1.92	0.89
Zn	30	L series	22096	5.80	6.23	2.48
<b>Total</b>			<b>93.12</b>	<b>100.00</b>	<b>100.00</b>	<b>0.39</b>

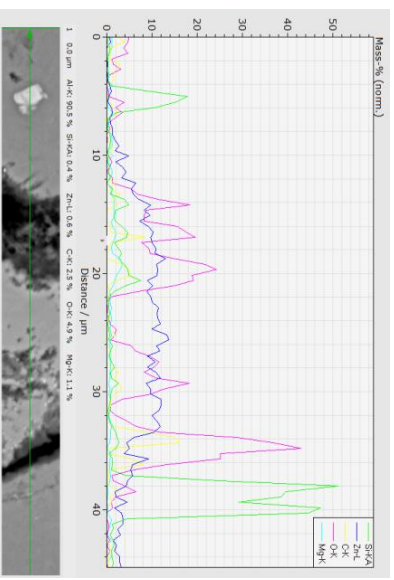
Quantification of spectrum results



EDS line scan results

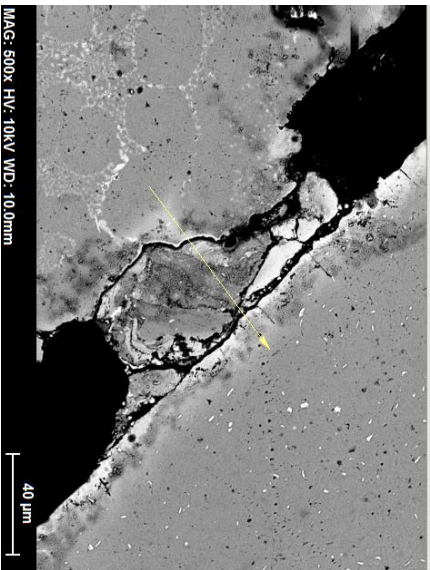


Line scan with logarithmic scale

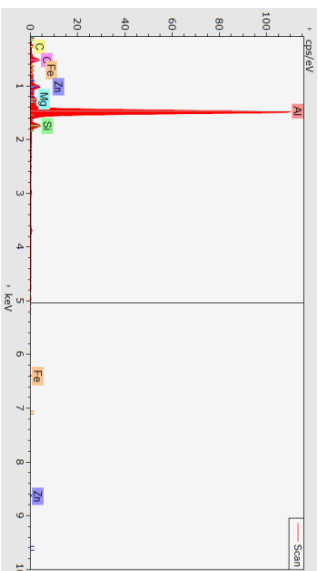


Line scan without aluminium

### Series 1-1, Sample 3



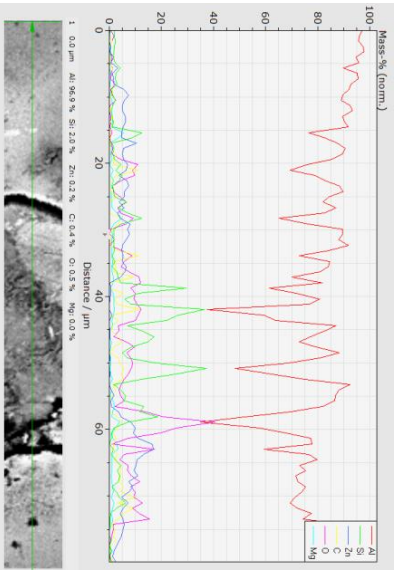
Micrograph with line scan indicated by the arrow



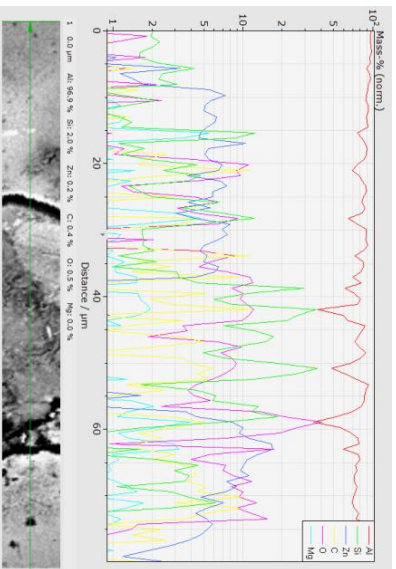
EDS Spectrum

Results table					
Element	AN	Series	Net	Mass C., norm. C. [wt.%]	Atom C., Error (1 Sigma) [at.%]
C	6	K series	2622	4.80	5.25
O	8	K series	10890	5.31	5.81
Mg	12	K series	7385	1.18	1.29
Al	13	K series	425637	70.87	77.50
Si	14	K series	15942	5.08	5.55
Fe	26	K series	83	0.31	0.34
Zn	30	L series	13229	3.90	4.26
<b>Total</b>			<b>91.45</b>	<b>100.00</b>	<b>100.00</b>

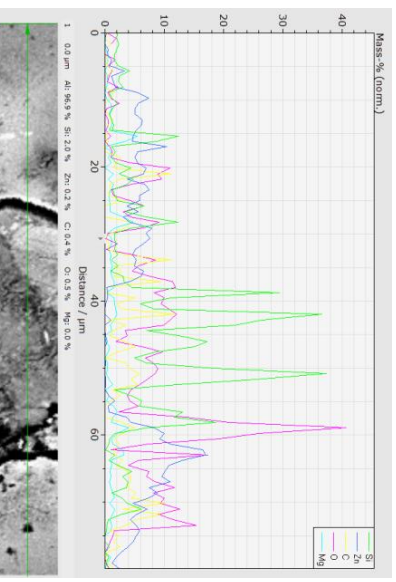
Quantification of spectrum results



EDS line scan results



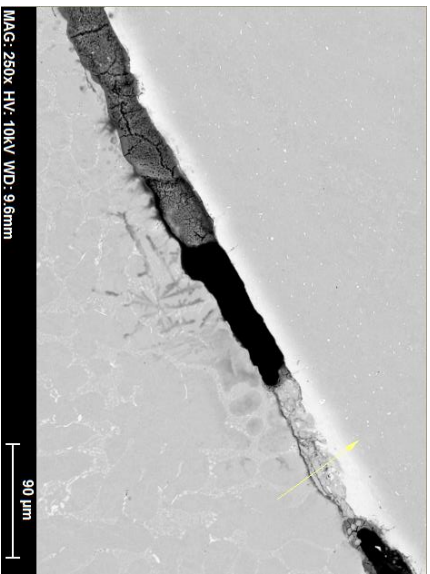
Line scan with logarithmic scale



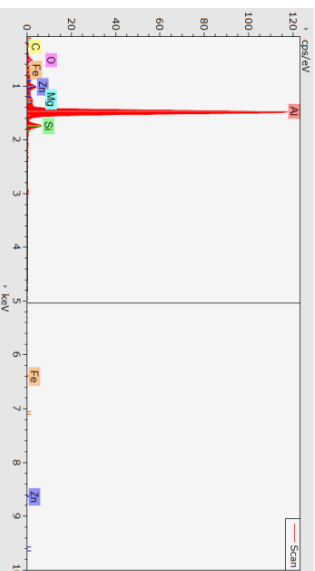
Line scan without aluminium



# Series 1-2, Sample 4



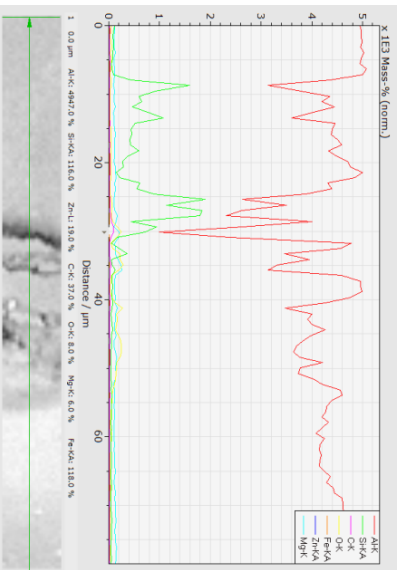
Micrograph with line scan indicated by the arrow



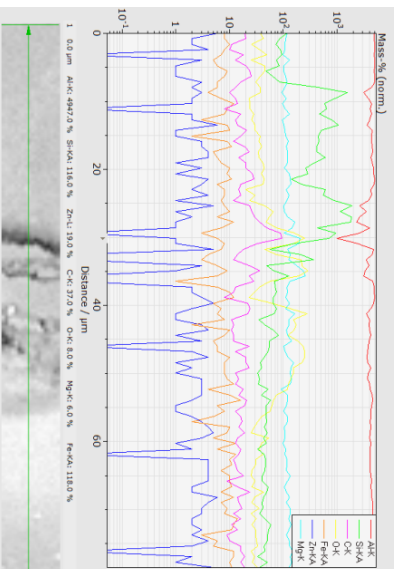
EDS Spectrum

Results table						
Element	AW	Series	Net	Mass C., norm. C. [wt.%]	Atom C. [at.%]	Error (1 Sigma) [wt.%]
C	6	K series	1447	2.90	3.19	0.62
O	8	K series	5210	2.65	2.91	0.44
Mg	12	K series	6107	0.99	1.09	0.08
Al	13	K series	430084	72.94	80.06	3.29
Si	14	K series	23986	7.89	8.66	0.35
Fe	26	K series	0	0.00	0.00	0.00
Zn	30	L series	12550	3.73	4.10	1.64
<b>Total</b>				<b>91.10</b>	<b>100.00</b>	<b>100.00</b>

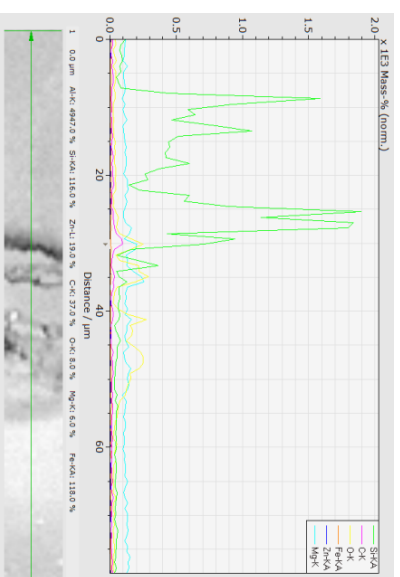
Quantification of spectrum results



EDS line scan results

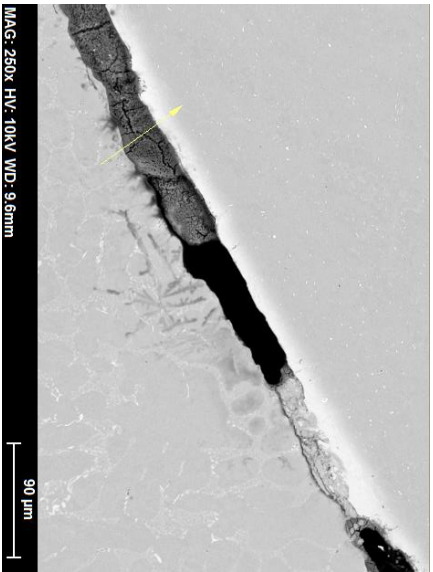


Line scan with logarithmic scale

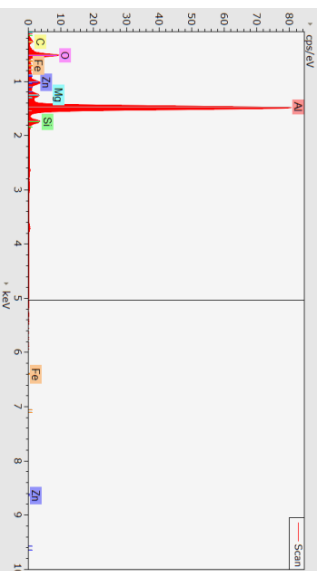


Line scan without aluminium

# Series 1-2, Sample 4



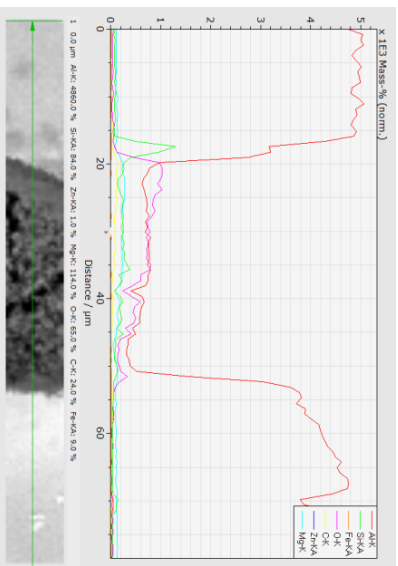
Micrograph with line scan indicated by the arrow



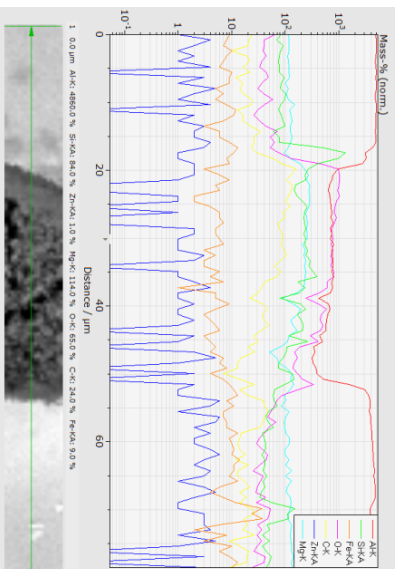
EDS Spectrum

Results table							
Element	AW	Series	Net [wt.%]	Mass C., norm. C. [wt.%]	Atom C., [at.%]	Error (1 Sigma) [wt.%]	
C	6	K series	3475	6.45	7.27	13.97	1.11
O	8	K series	25636	13.74	15.48	22.34	1.74
Mg	12	K series	9724	1.86	2.10	1.99	0.12
Al	13	K series	294945	57.91	65.28	55.85	2.62
Si	14	K series	12546	4.43	4.99	4.10	0.21
Fe	26	K series	71	0.31	0.35	0.14	0.07
Zn	30	L series	11319	4.03	4.54	1.60	0.28
<b>Total</b>			<b>88.72</b>	<b>100.00</b>	<b>100.00</b>		

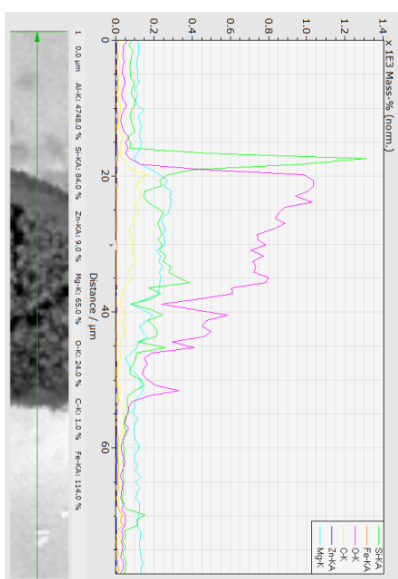
Quantification of spectrum results



EDS line scan results

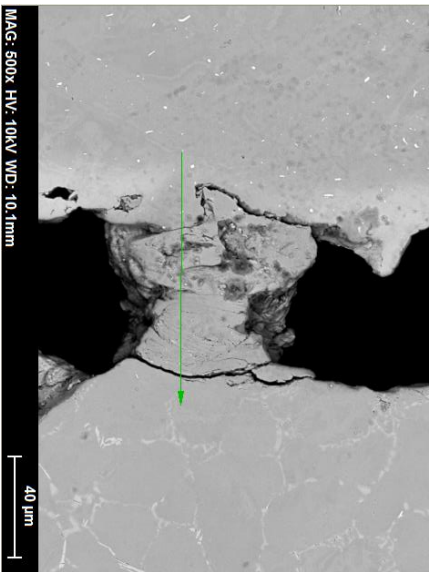


Line scan with logarithmic scale

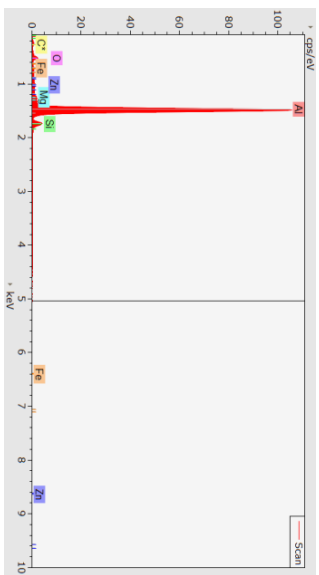


Line scan without aluminium

## Series 1-2, Sample 5



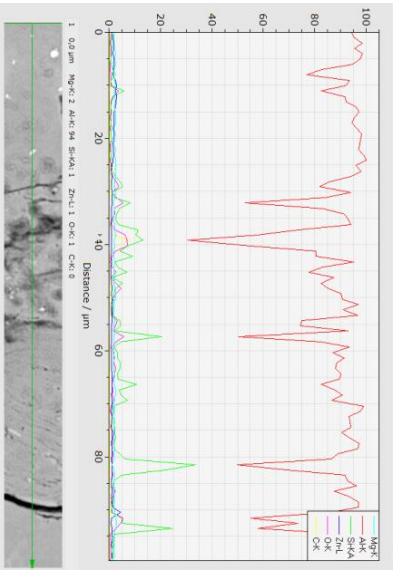
Micrograph with line scan indicated by the arrow



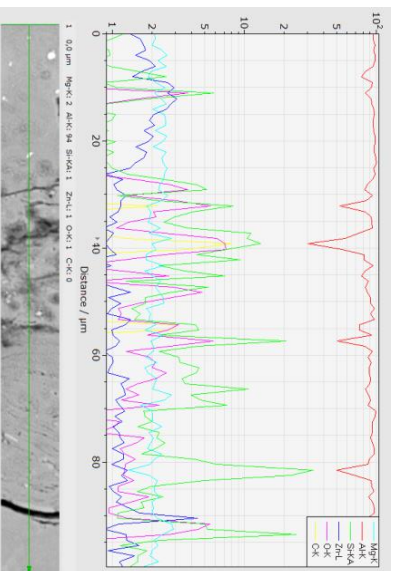
EDS Spectrum

Results table							
Element	AN	Series	Net	Mass C.	norm. C.	Atom C.	Error (1 Sigma)
			[wt.%]	[wt.%]	[at.%]		[wt.%]
C	6	K series	2576	0.00	0.00	0.00	0.54
O	8	K series	7287	3.51	3.83	6.35	0.08
Mg	12	K series	6159	0.95	1.04	1.13	3.60
Al	13	K series	483317	79.75	87.02	85.52	0.29
Si	14	K series	18771	6.25	6.82	6.44	0.07
Fe	26	K series	105	0.39	0.42	0.20	0.08
Zn	30	L series	2676	0.80	0.87	0.35	0.08
<b>Total</b>			<b>91.65</b>	<b>100.00</b>	<b>100.00</b>		

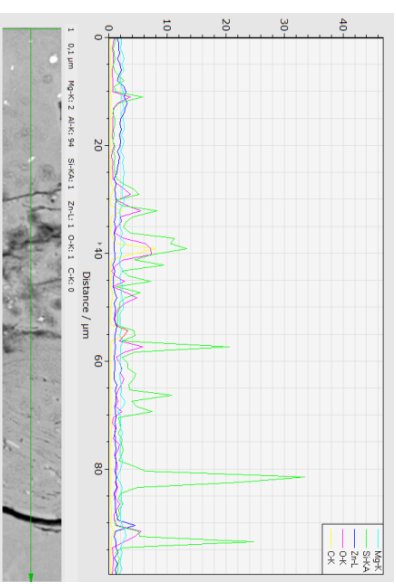
Quantification of spectrum results



EDS line scan results

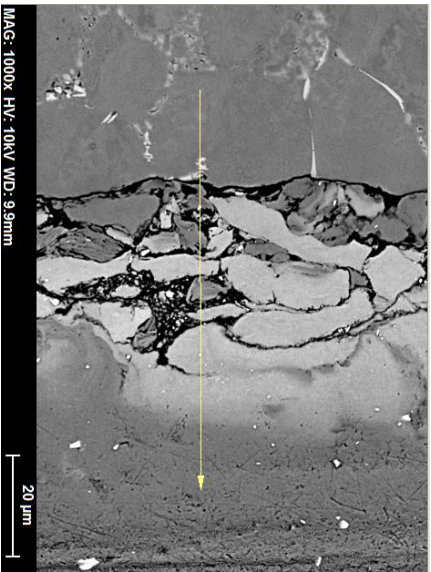


Line scan with logarithmic scale

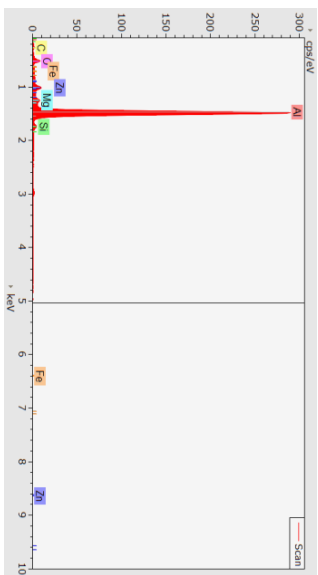


Line scan without aluminium

## Series 1-2, Sample 6



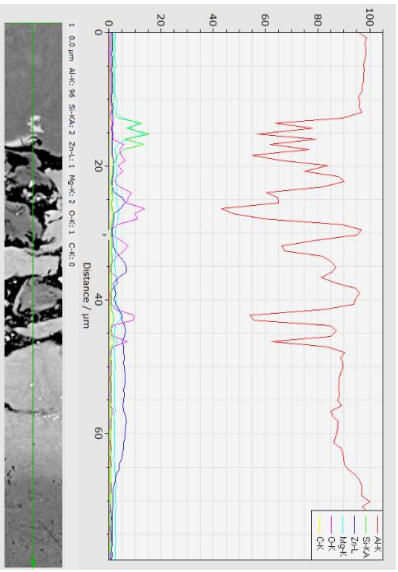
Micrograph with line scan indicated by the arrow



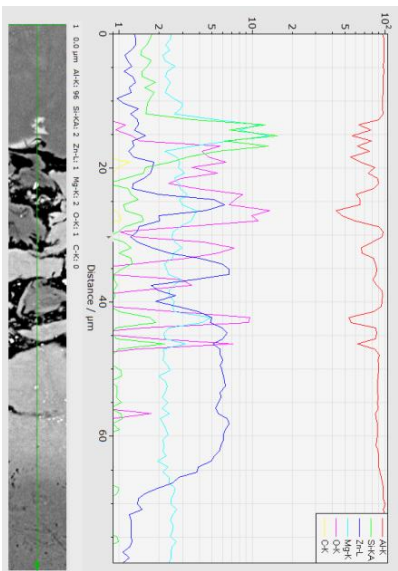
EDS Spectrum

Results table						
Element	AN	Series	Net [wt.%]	norm. C. [wt.%]	Atom C. [at.%]	Error (1 Sigma) [wt.%]
C	6	K series	5570	3.40	3.90	0.55
O	8	K series	26052	4.13	4.73	0.54
Mg	12	K series	27113	1.41	1.62	0.10
Al	13	K series	1329595	72.84	83.42	3.28
Si	14	K series	17117	1.84	2.11	0.10
Fe	26	K series	171	0.21	0.24	0.05
Zn	30	L series	36229	3.49	3.99	1.56
<b>Total</b>			<b>87.32</b>	<b>100.00</b>	<b>100.00</b>	<b>0.24</b>

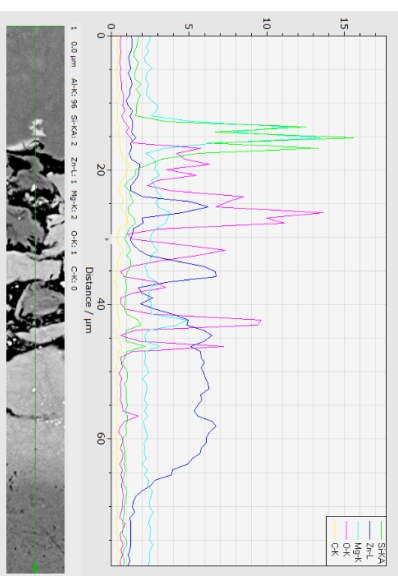
Quantification of spectrum results



EDS line scan results

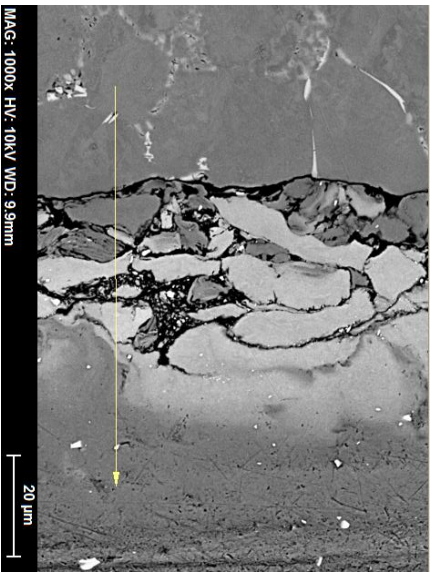


Line scan with logarithmic scale

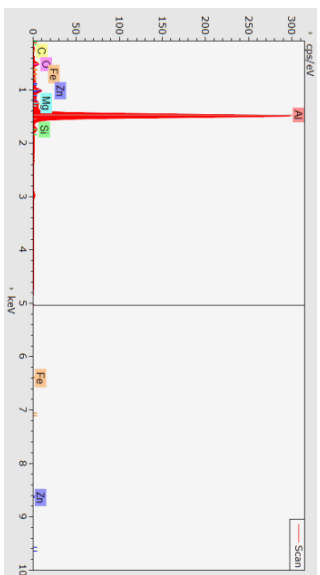


Line scan without aluminium

## Series 1-2, Sample 6



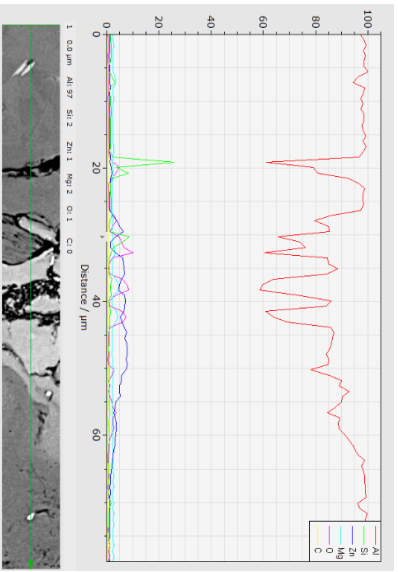
Micrograph with line scan indicated by the arrow



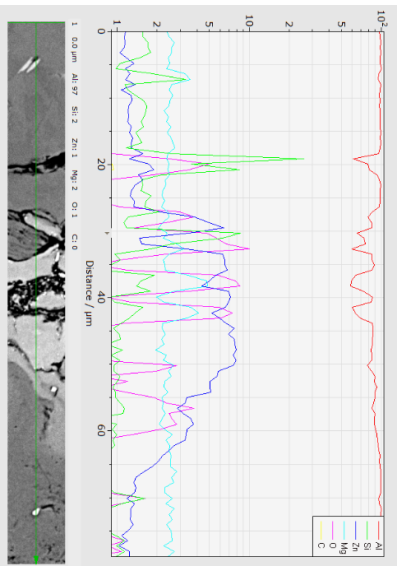
EDS Spectrum

Results table						
Element	AN	Series	Net	Mass C.	norm. C.	Atom C.
			[wt.%]	[wt.%]	[wt.%]	[at.%]
C	6	K series	5204	3.26	3.66	7.85
O	8	K series	20319	3.27	3.67	5.91
Mg	12	K series	21523	1.13	1.27	1.34
Al	13	K series	1379355	75.87	85.28	81.38
Si	14	K series	17165	1.87	2.10	1.93
Fe	26	K series	89	0.11	0.12	0.06
Zn	30	L series	35875	3.46	3.89	1.53
<b>Total</b>			<b>88,96</b>	<b>100.00</b>	<b>100.00</b>	<b>100.00</b>

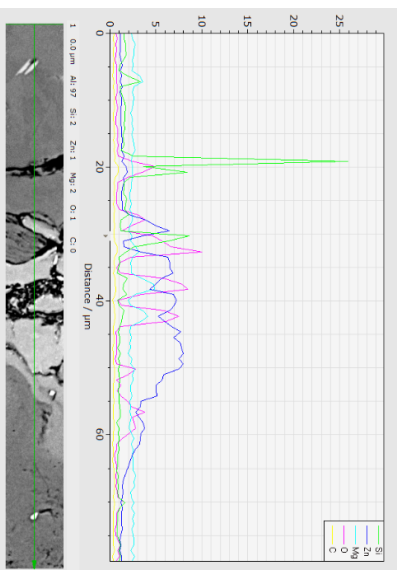
Quantification of spectrum results



EDS line scan results

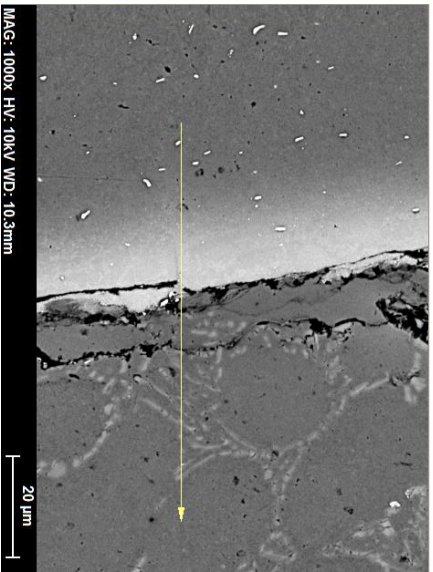


Line scan with logarithmic scale

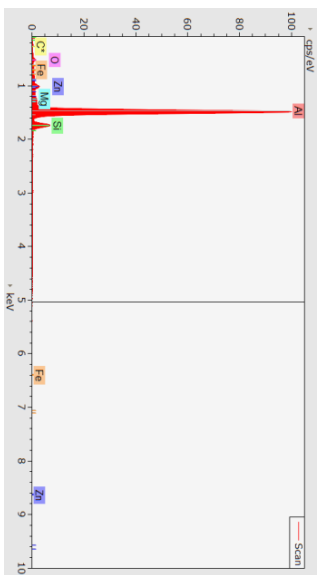


Line scan without aluminium

# Series 1-3, Sample 7



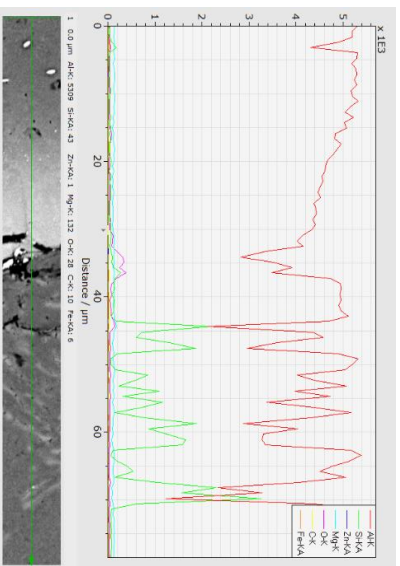
Micrograph with line scan indicated by the arrow



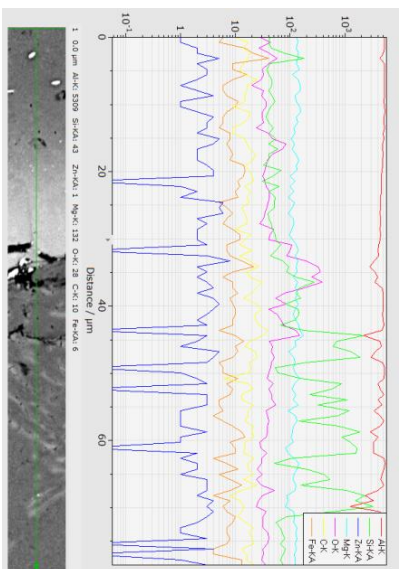
EDS Spectrum

Results table						
Element	AN	Series	Net [wt.%]	Mass C. norm. C. [wt.%]	Atom C. [at.%]	Error (1 Sigma) [wt.%]
C	6	K series	1251	0.00	0.00	0.32
O	8	K series	3538	1.77	1.90	3.23
Mg	12	K series	5798	0.92	0.98	1.10
Al	13	K series	459763	76.78	82.10	82.89
Si	14	K series	33662	11.03	11.80	11.44
Fe	26	K series	0	0.00	0.00	0.00
Zn	30	L series	10242	3.02	3.23	1.34
<b>Total</b>			<b>93.52</b>	<b>100.00</b>	<b>100.00</b>	<b>0.22</b>

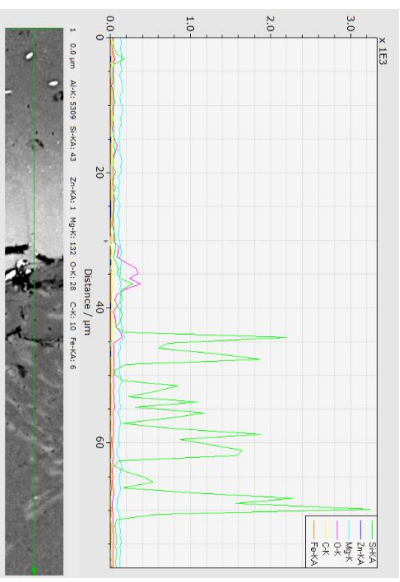
Quantification of spectrum results



EDS line scan results

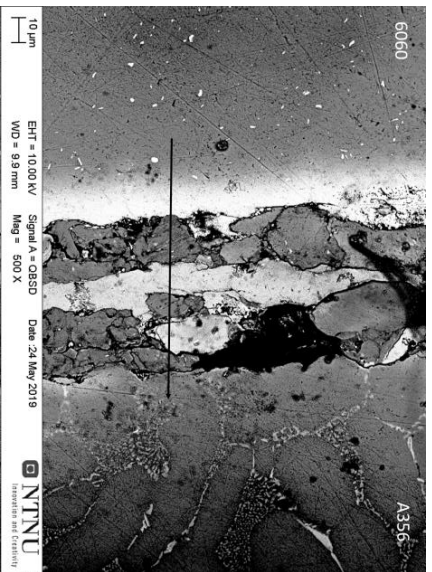


Line scan with logarithmic scale

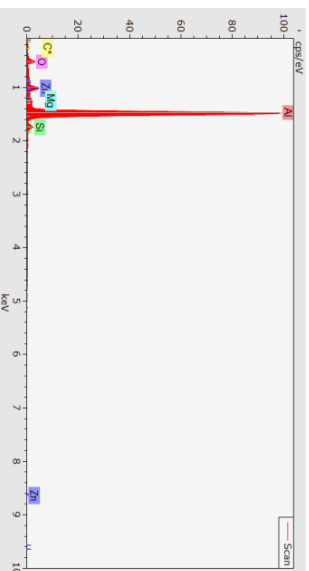


Line scan without aluminium

## Series 1-3, Sample 8



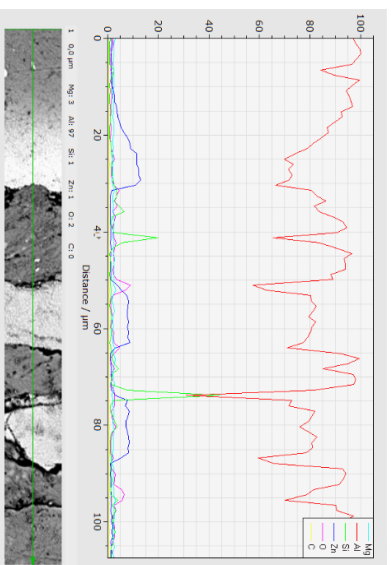
Micrograph with line scan indicated by the arrow



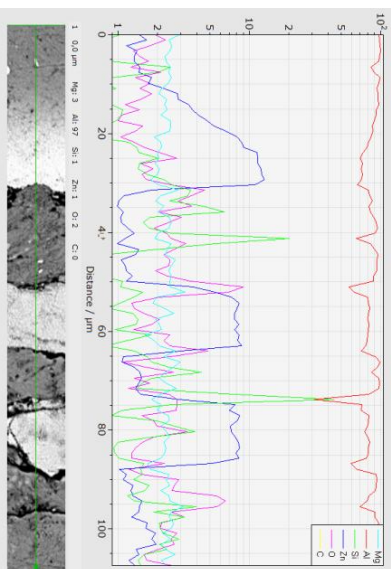
EDS Spectrum

Results table							
Element	AN	Series	Net	Mass C.	norm. C.	Atom C.	Error (1 Sigma)
			[wt. %]	[wt. %]	[at. %]		[wt. %]
Al	13	K series	451948	75.78	84.16	84.08	3.42
O	8	K series	9973	4.71	5.23	8.81	0.68
Si	14	K series	9593	3.13	3.48	3.34	0.16
Zn	30	L series	18438	5.36	5.95	2.45	0.36
Mg	12	K series	6584	1.07	1.18	1.31	0.08
C	6	K series	2033	0.00	0.00	0.00	0.00
<b>Total</b>			<b>90.05</b>	<b>100.00</b>	<b>100.00</b>	<b>100.00</b>	

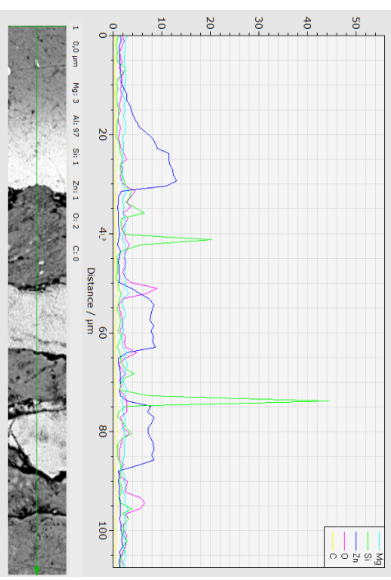
Quantification of spectrum results



EDS line scan results

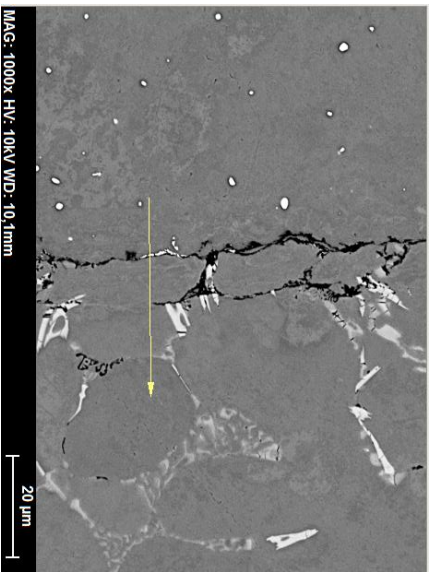


Line scan with logarithmic scale

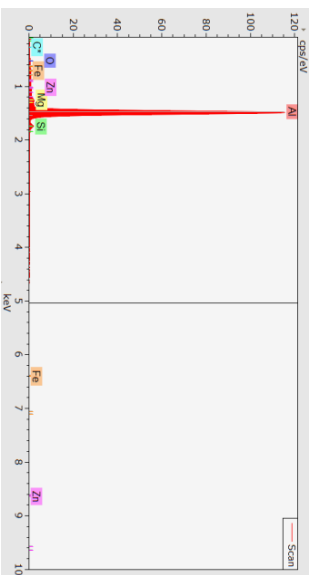


Line scan without aluminium

## Series 2-1, Sample 11



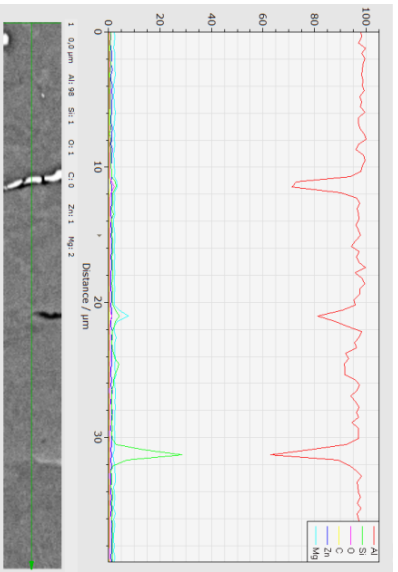
Micrograph with line scan indicated by the arrow



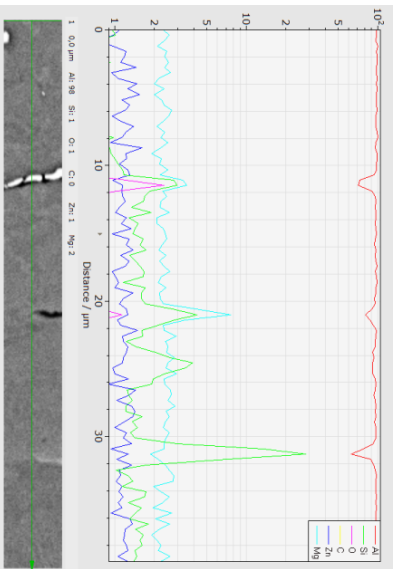
EDS Spectrum

Results table					
Element	AN	Series	Net [wt.%]	Mass C, norm. C, [wt.%]	Atom C, Error (1 Sigma) [at.%]
C	6	K series	1084	0.00	0.00
O	8	K series	1244	0.60	0.66
Mg	12	K series	7795	1.17	1.28
Al	13	K series	529115	86.62	94.44
Si	14	K series	7862	2.69	2.93
Fe	26	K series	59	0.22	0.24
Zn	30	L series	1435	0.42	0.46
<b>Total</b>			<b>91.72</b>	<b>100.00</b>	<b>100.00</b>

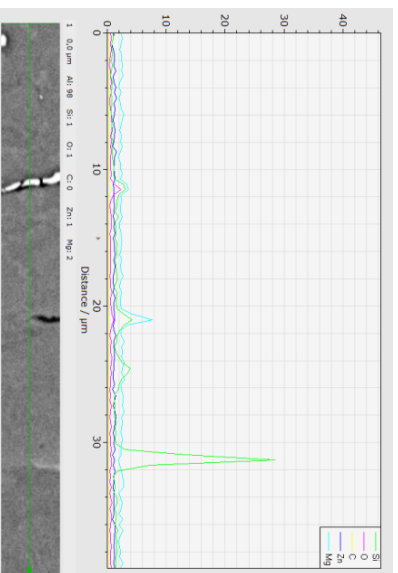
Quantification of spectrum results



EDS line scan results



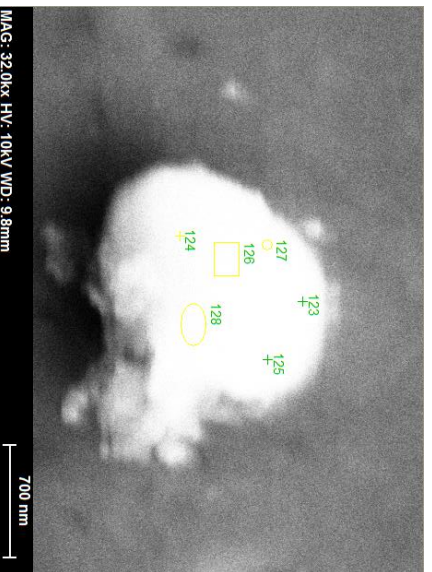
Line scan with logarithmic scale



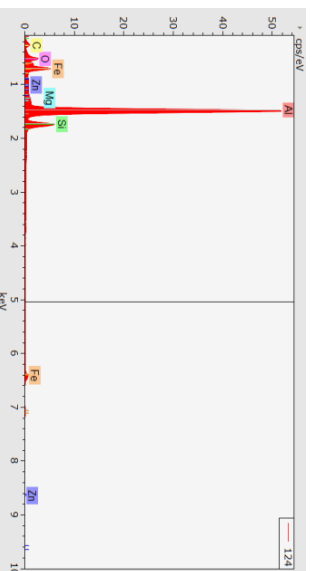
Line scan without aluminium



## Series 2-1, Sample 11



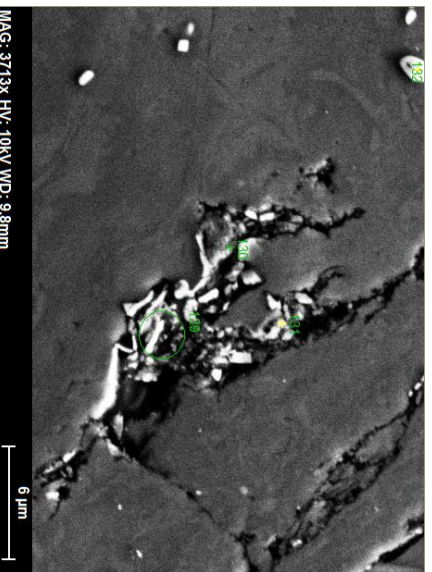
Micrograph with EDS analysis points shown



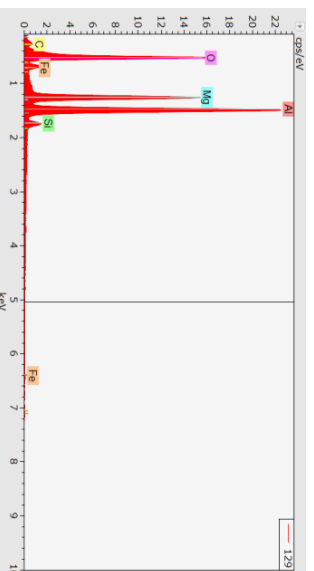
EDS Spectrum

Results table					
Element	AN	Series	Net	Mass C., norm. C. [wt.%]	Atom C., Error (1 Sigma) [at.%, [wt.%]
C	6	K series	7020	6.13	6.34 14.43 0.93
O	8	K series	19699	5.09	5.26 8.99 0.68
Mg	12	K series	6280	0.61	0.63 0.71 0.06
Al	13	K series	542631	51.64	53.44 54.11 2.34
Si	14	K series	63826	10.00	10.35 10.07 0.44
Fe	26	K series	11277	22.54	23.33 11.41 1.05
Zn	30	L series	3030	0.62	0.64 0.27 0.07
<b>Total</b>			<b>96.63</b>	<b>100.00</b>	<b>100.00</b>

Quantification of spectrum results



Micrograph with EDS analysis points shown

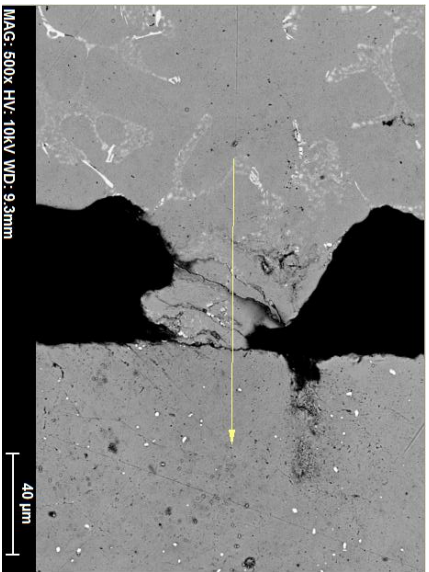


EDS Spectrum

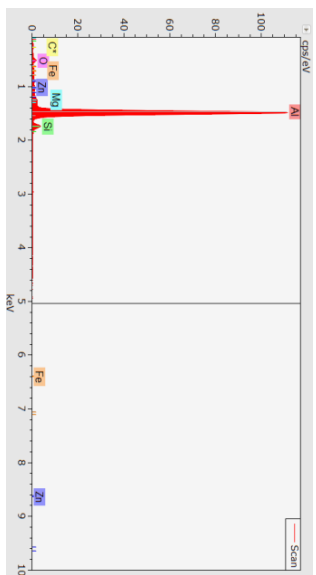
Results table					
Element	AN	Series	Net	Mass C., norm. C. [wt.%]	Atom C., Error (1 Sigma) [at.%, [wt.%]
O	8	K series	16956	46.32	30.61 53.96 5.11
Mg	12	K series	13293	21.55	14.24 16.53 1.12
Br	35	L series	312190	64.49	42.62 15.04 2.93
C	6	K series	3369	2.65	1.75 4.12 0.47
Al	13	K series	45268	5.72	3.78 3.95 0.28
F	9	K series	9734	2.68	1.77 2.63 0.40
Si	14	K series	16647	3.44	2.27 2.28 0.17
Fe	26	K series	1577	4.47	2.95 1.49 0.27
<b>Total</b>			<b>151.32</b>	<b>100.00</b>	<b>100.00</b>

Quantification of spectrum results

## Series 2-1, Sample 12



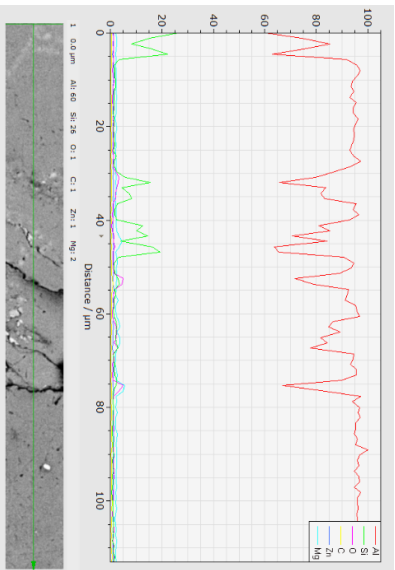
Micrograph with line scan indicated by the arrow



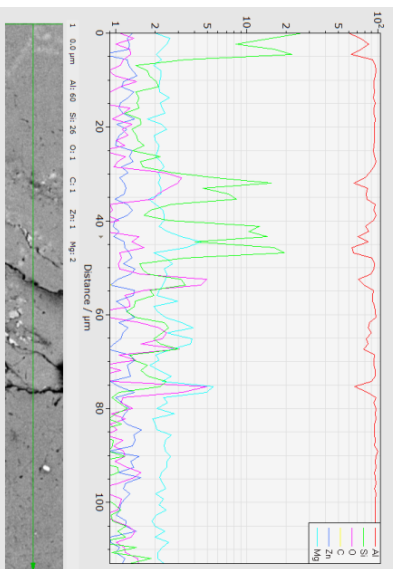
EDS Spectrum

Results table					
Element	AN	Series	Net	Mass C, norm. C, Atom C, Error (1 Sigma)	
			[wt.%]	[wt.%]	[at.%]
C	6	K series	2068	0.00	0.00
O	8	K series	5544	2.61	2.85
Mg	12	K series	7580	1.13	1.23
Al	13	K series	511567	82.03	89.41
Si	14	K series	16314	5.35	5.83
Fe	26	K series	48	0.17	0.19
Zn	30	L series	1592	0.46	0.50
<b>Total</b>			<b>91.75</b>	<b>100.00</b>	<b>100.00</b>

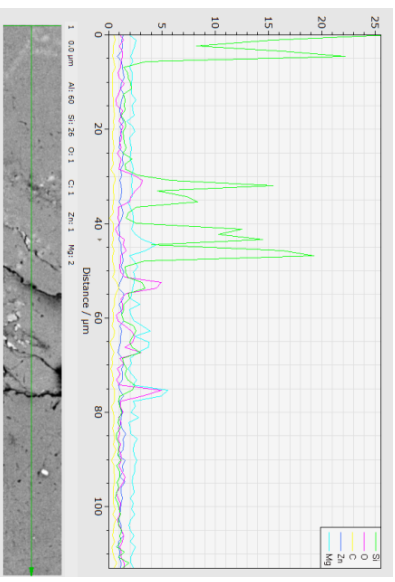
Quantification of spectrum results



EDS line scan results

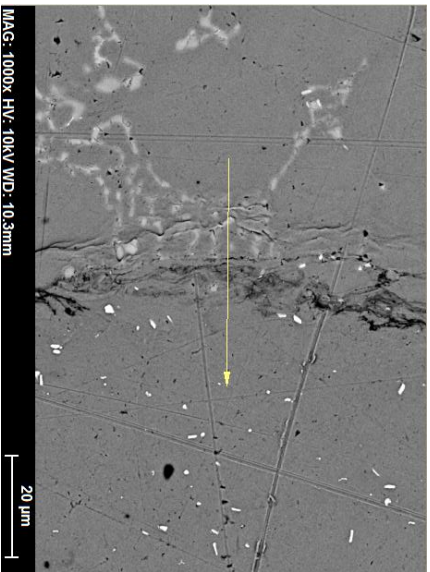


Line scan with logarithmic scale

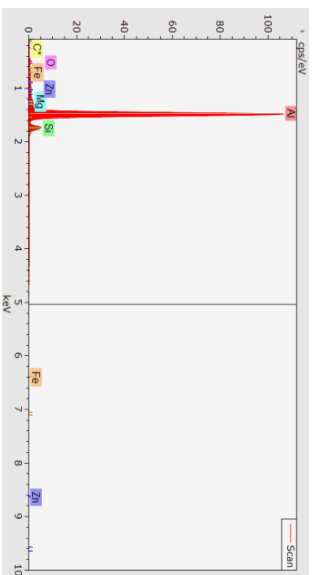


Line scan without aluminium

## Series 2-2, Sample 13



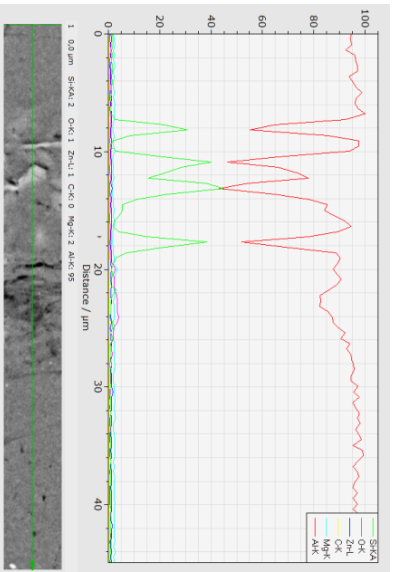
Micrograph with line scan indicated by the arrow



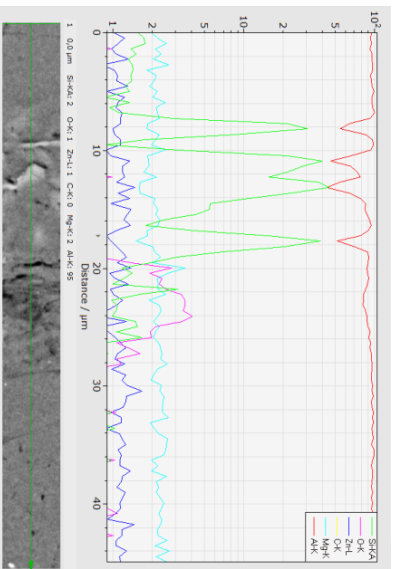
EDS Spectrum

Results table						
Element	AN	Series	Net	Mass C, [wt.%]	norm. C, [wt.%]	Atom C, Error (1 Sigma) [at.%]
C	6	K series	1288	0.00	0.00	0.00
O	8	K series	3340	1.65	1.81	3.02
Mg	12	K series	6177	0.94	1.03	1.14
Al	13	K series	486744	80.24	87.76	87.07
Si	14	K series	24653	8.28	9.05	8.63
Fe	26	K series	0	0.00	0.00	0.00
Zn	30	L series	1072	0.32	0.35	0.14
<b>Total</b>			<b>91.42</b>	<b>100.00</b>	<b>100.00</b>	<b>0.05</b>

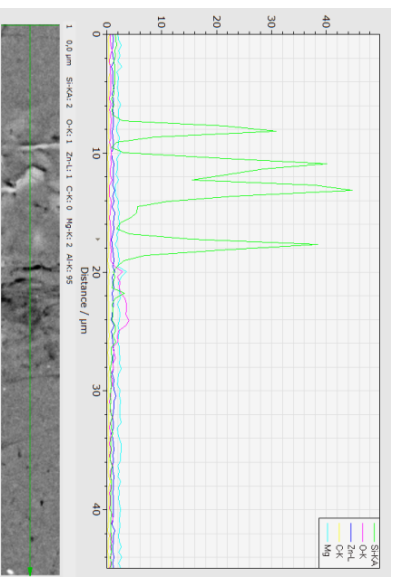
Quantification of spectrum results



EDS line scan results

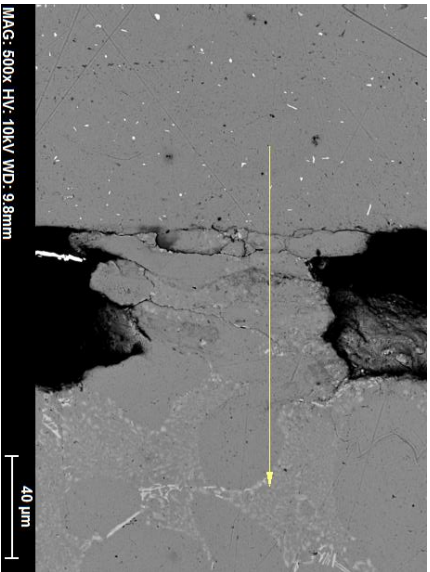


Line scan with logarithmic scale

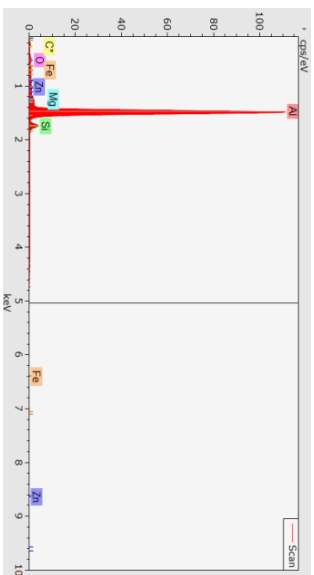


Line scan without aluminium

## Series 2-2, Sample 14



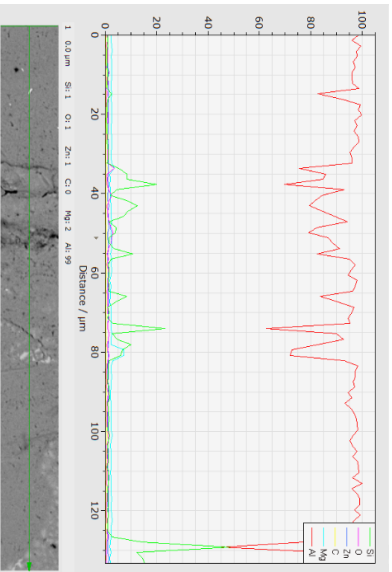
Micrograph with line scan indicated by the arrow



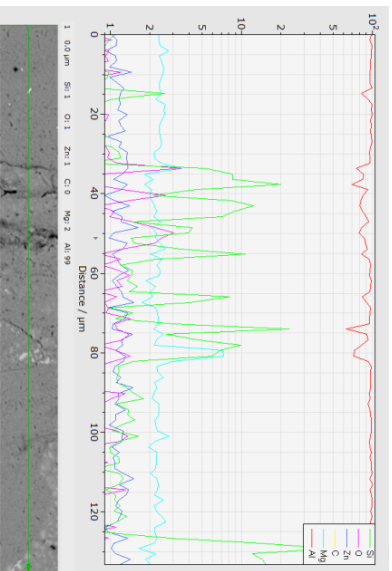
EDS Spectrum

Results table					
Element	AN	Series	Net	Mass C, norm. C, [wt.%]	Atom C, Error (1 Sigma) [at.%]
C	6	K series	1732	0.00	0.00
O	8	K series	3310	1.59	1.73
Mg	12	K series	7313	1.09	1.31
Al	13	K series	511942	82.85	90.10
Si	14	K series	17720	5.88	6.40
Fe	26	K series	28	0.10	0.11
Zn	30	L series	1488	0.43	0.47
<b>Total</b>			<b>91.95</b>	<b>100.00</b>	<b>100.00</b>

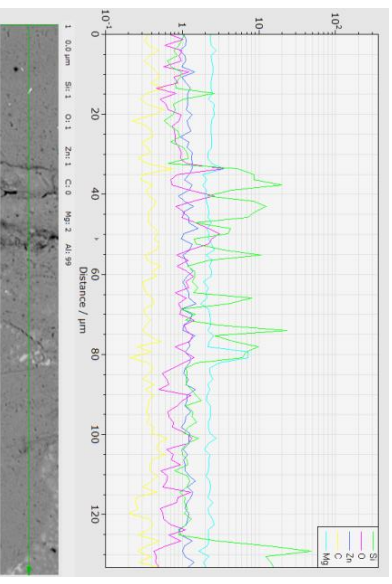
Quantification of spectrum results



EDS line scan results

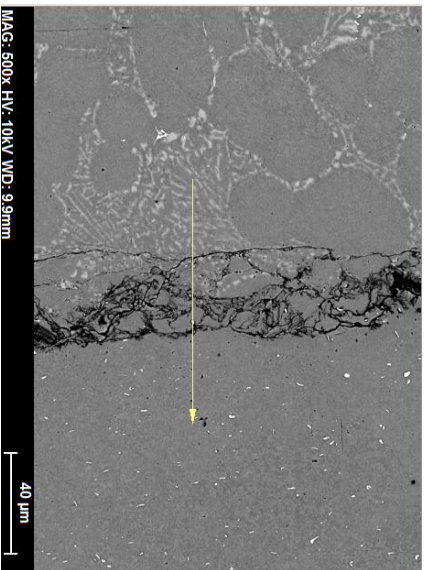


Line scan with logarithmic scale

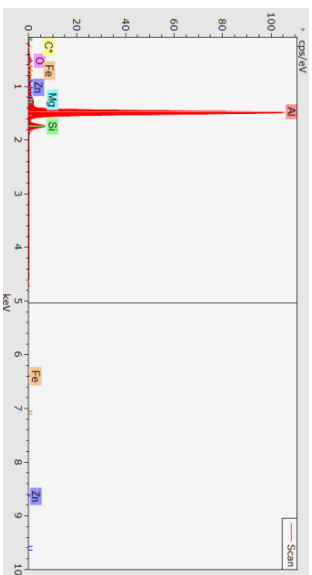


Line scan without aluminium

## Series 2-2, Sample 15



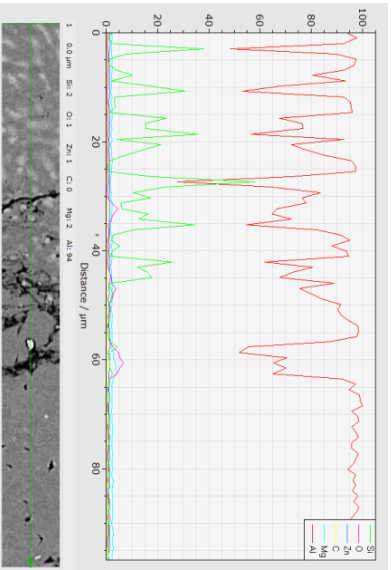
Micrograph with line scan indicated by the arrow



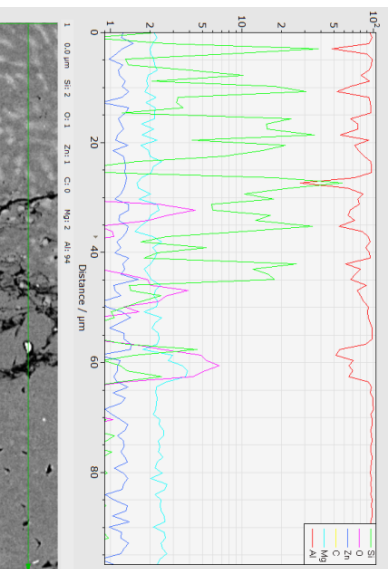
EDS Spectrum

Results table					
Element	AW	Series	Net [wt.%]	Mass C. norm. C. [wt.%]	Atom C. Error (1 Sigma) [wt.%]
C	6	K series	1392	0.00	0.00
O	8	K series	4114	2.02	2.16
Mg	12	K series	6729	1.02	1.09
Al	13	K series	482808	79.80	84.38
Si	14	K series	32829	10.73	11.49
Fe	26	K series	80	0.30	0.32
Zn	30	L series	1772	0.52	0.56
<b>Total</b>			<b>93.38</b>	<b>100.00</b>	<b>100.00</b>

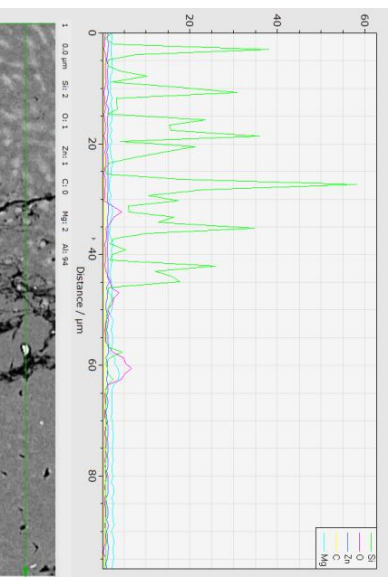
Quantification of spectrum results



EDS line scan results

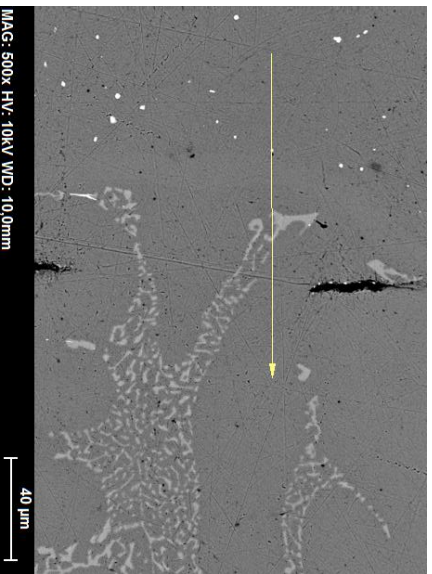


Line scan with logarithmic scale

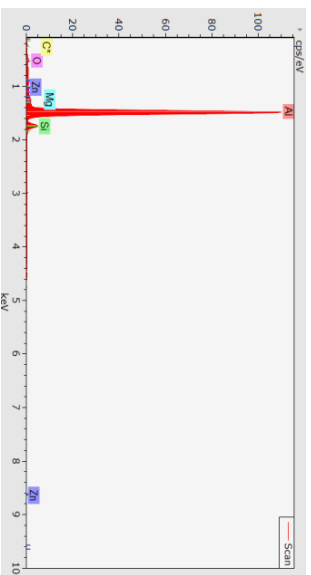


Line scan without aluminium

# Series 3-1, Sample 16



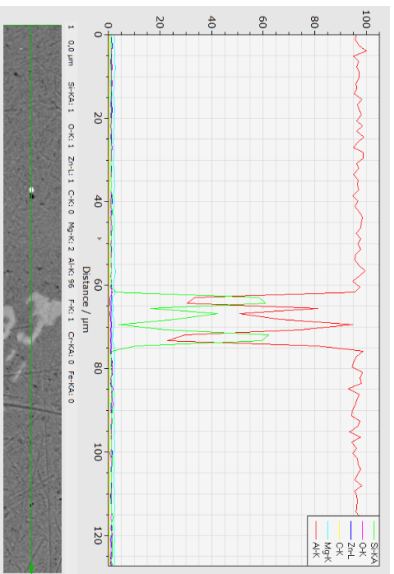
Micrograph with line scan indicated by the arrow



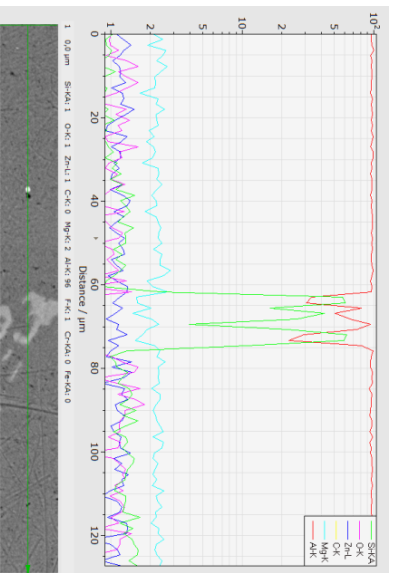
EDS Spectrum

Results table							
Element	Al	Series	Net	Mass C. [wt.%]	norm. C. [wt.%]	Atom C. [at.%]	Error (1 Sigma) [wt.%]
Al	13	K series	505188	83.01	88.12	87.68	3.74
Si	14	K series	22911	7.66	8.13	7.77	0.34
O	8	K series	3249	1.59	1.69	2.84	0.30
Mg	12	K series	6243	0.95	1.01	1.12	0.08
Fe	26	K series	132	0.49	0.52	0.25	0.06
F	9	K series	373	0.12	0.13	0.18	0.05
Zn	30	L series	1362	0.38	0.40	0.16	0.05
C	6	K series	1410	0.00	0.00	0.00	0.00
Cr	24	K series	0	0.00	0.00	0.00	0.00
<b>Total</b>			<b>94,20</b>	<b>100,00</b>	<b>100,00</b>	<b>100,00</b>	

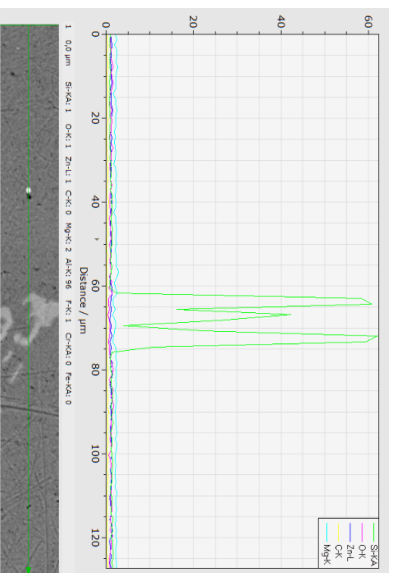
Quantification of spectrum results



EDS line scan results

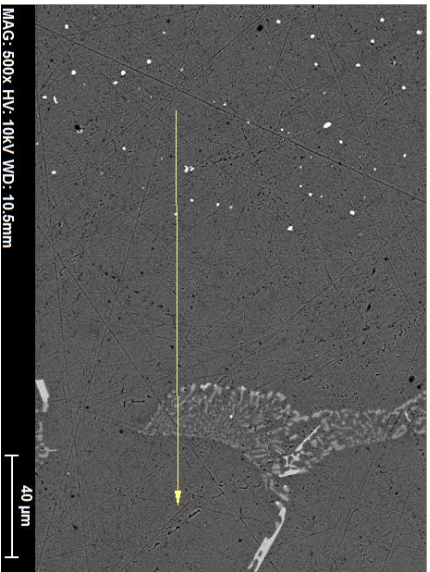


Line scan with logarithmic scale

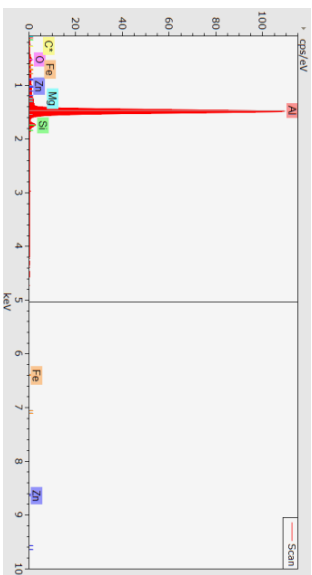


Line scan without aluminium

## Series 3-1, Sample 18



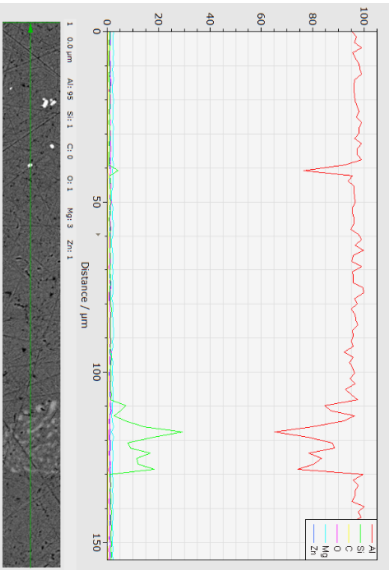
Micrograph with line scan indicated by the arrow



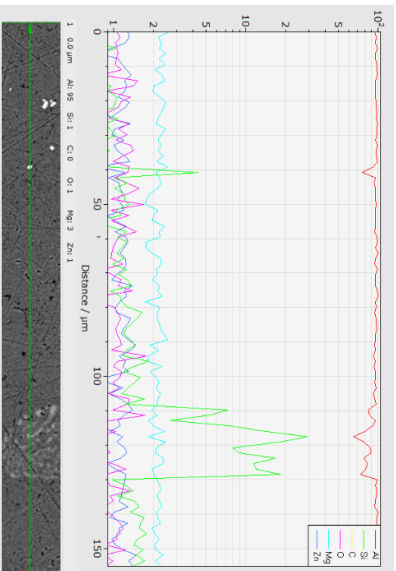
EDS Spectrum

Results table					
Element	AN	Series	Net	Mass C, norm. C, Atom C, Error (1 Sigma)	
			[wt.%]	[wt.%]	[at.%]
C	6	K series	1250	0.00	0.00
O	8	K series	3678	1.84	3.32
Mg	12	K series	5759	0.90	1.07
Al	13	K series	502531	85.15	92.07
Si	14	K series	11425	4.01	4.33
Fe	26	K series	55	0.21	0.23
Zn	30	L series	1223	0.37	0.40
<b>Total</b>			<b>92.48</b>	<b>100.00</b>	<b>100.00</b>

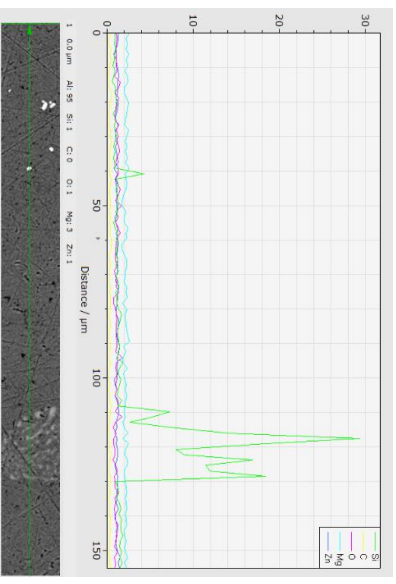
Quantification of spectrum results



EDS line scan results

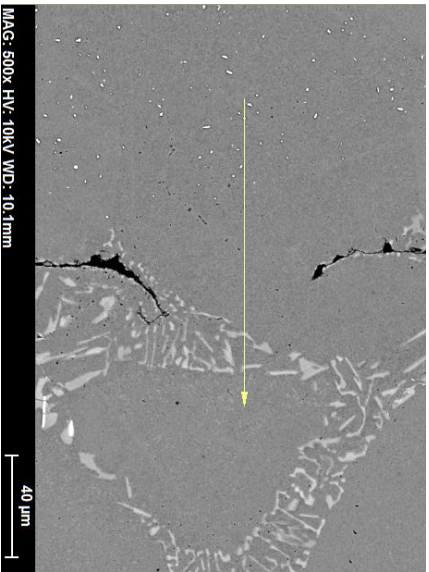


Line scan with logarithmic scale

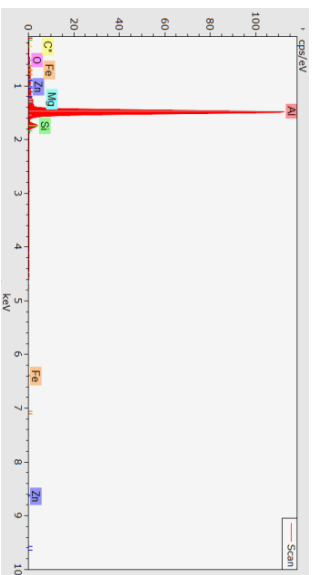


Line scan without aluminium

## Series 3-2, Sample 19



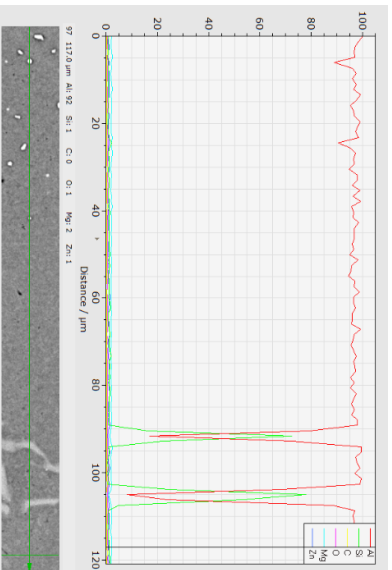
Micrograph with line scan indicated by the arrow



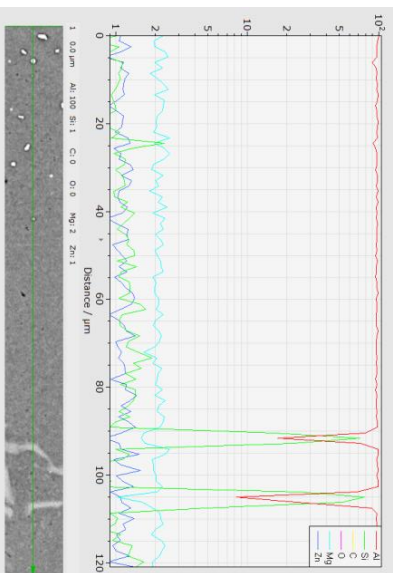
EDS Spectrum

Results table							
Element	AN	Series	Net	Mass C.	norm. C.	Atom C.	Error (1 Sigma)
			[wt.%]	[wt.%]	[wt.%]	[at.%]	[wt.%]
C	6	K series	899	0.00	0.00	0.00	0.13
O	8	K series	962	0.48	0.51	0.86	0.07
Mg	12	K series	5714	0.87	0.93	1.03	3.85
Al	13	K series	519171	85.51	91.30	91.42	0.29
Si	14	K series	18457	6.28	6.71	6.45	0.05
Fe	26	K series	43	0.16	0.17	0.08	0.05
Zn	30	L series	1207	0.36	0.38	0.16	0.05
<b>Total</b>			<b>93.66</b>	<b>100.00</b>	<b>100.00</b>		

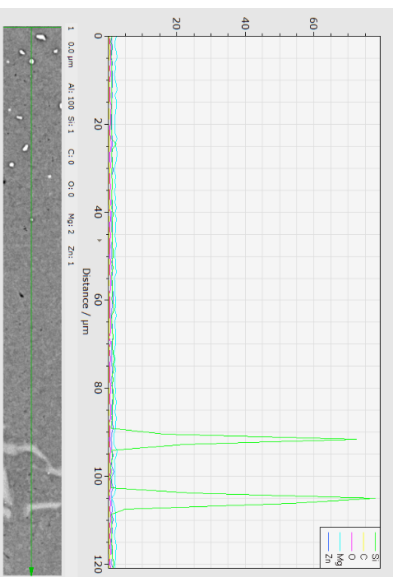
Quantification of spectrum results



EDS line scan results



Line scan with logarithmic scale



Line scan without aluminium



## Appendix C

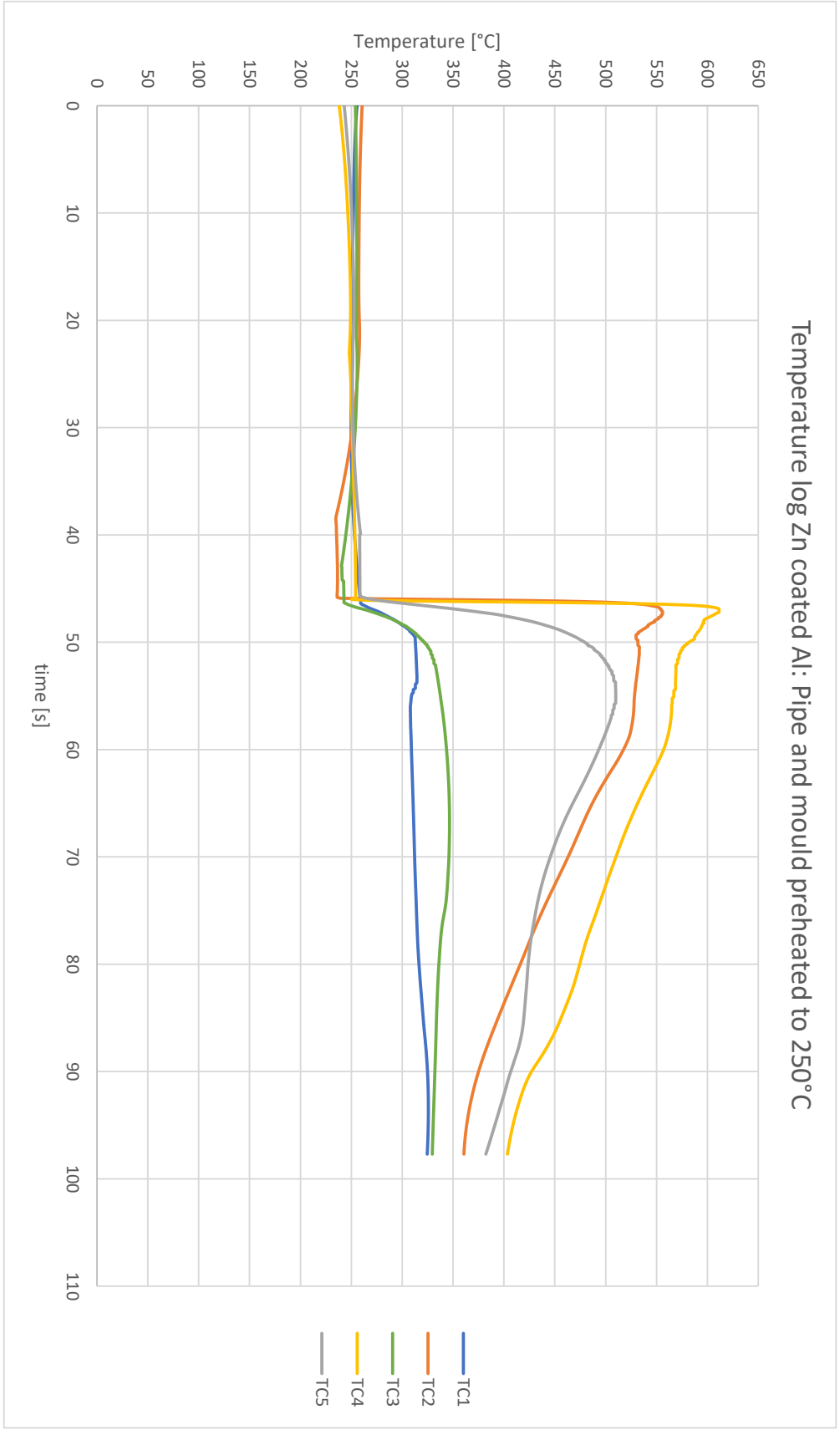
Modified temperature logs obtained during casting are shown in the following pages.

Placements of thermocouples during casting.

Thermocouple	Distance from top [mm]	Placement
TC1	80	Mould wall
TC2	80	Cavity/A356
TC3	65	Mould wall
TC4	65	Cavity/A356
TC5	50	Inside Pipe

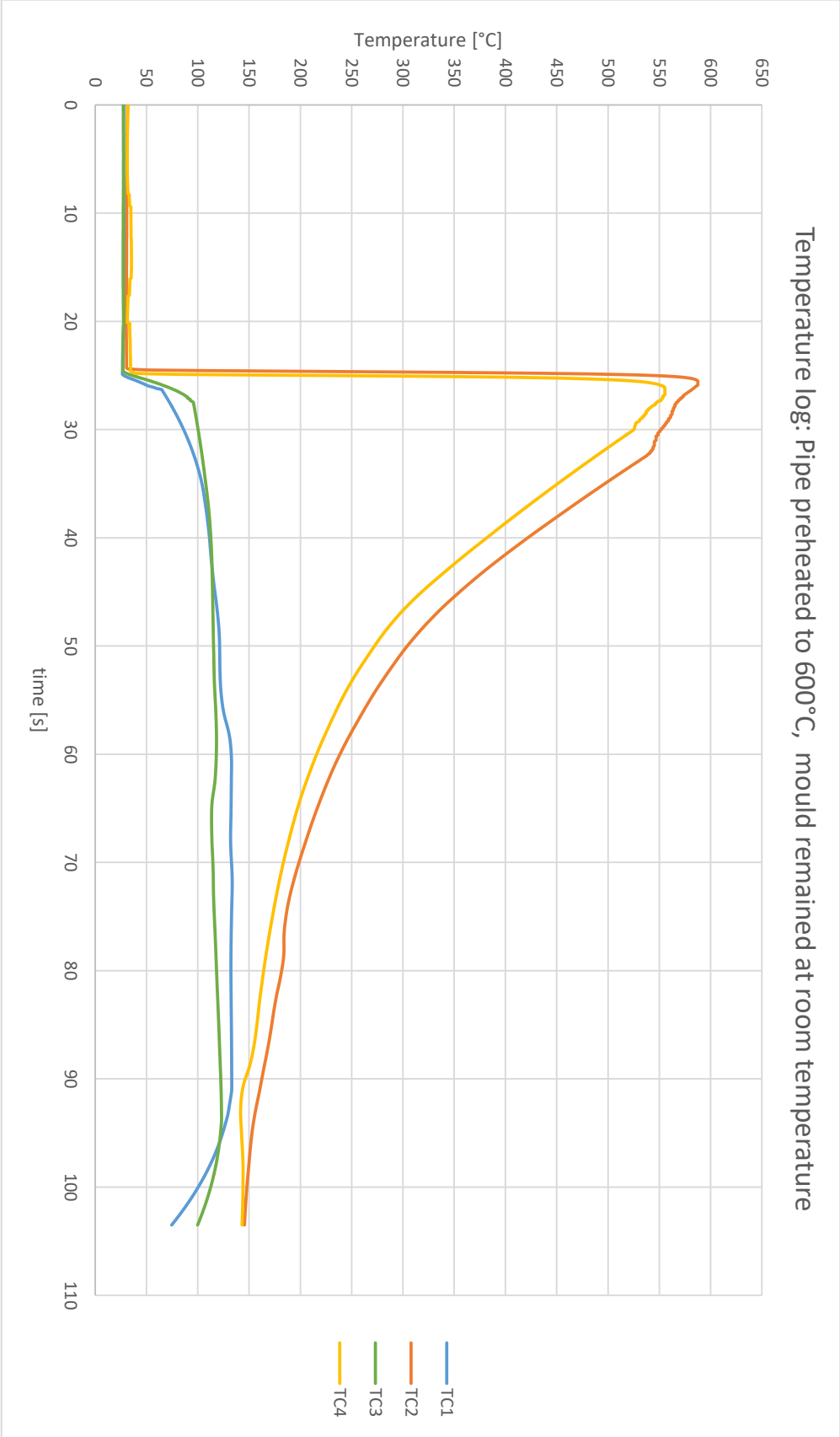
# Experiment 1

Temperature log Zn coated Al: Pipe and mould preheated to 250°C



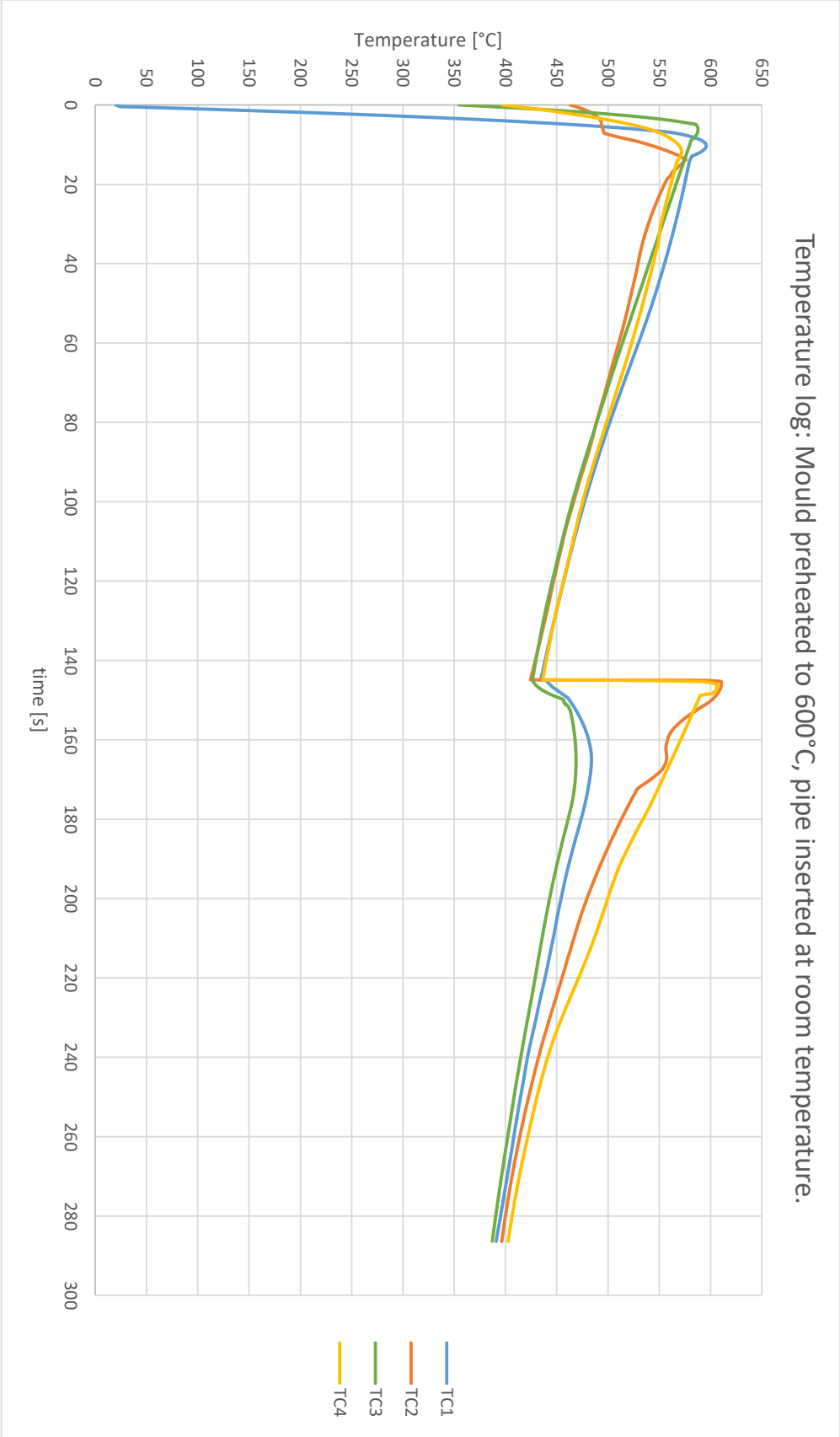
# Experiment 2, Series 1

Temperature log: Pipe preheated to 600°C, mould remained at room temperature



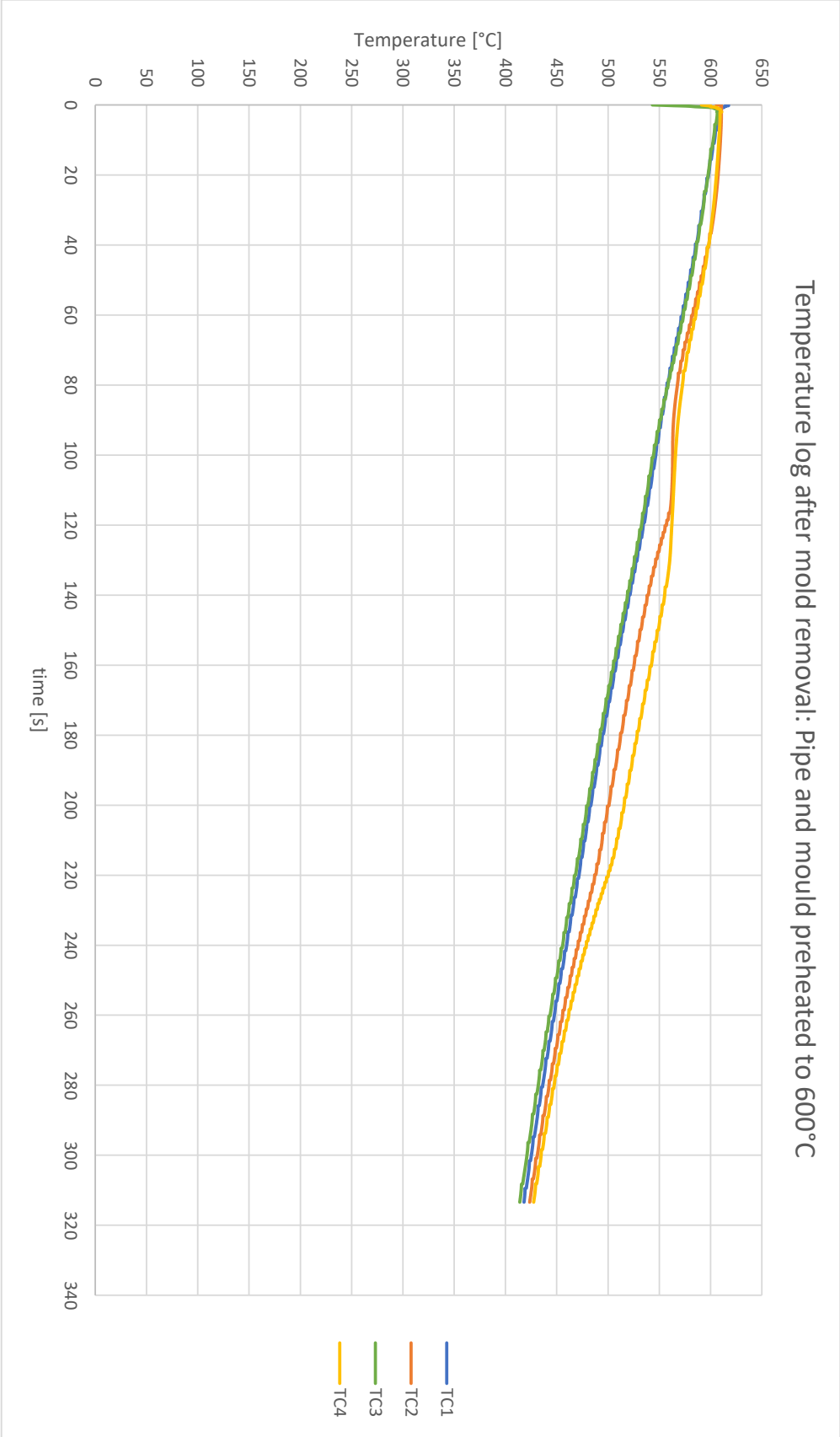
# Experiment 2, Series 2

Temperature log: Mould preheated to 600°C, pipe inserted at room temperature.

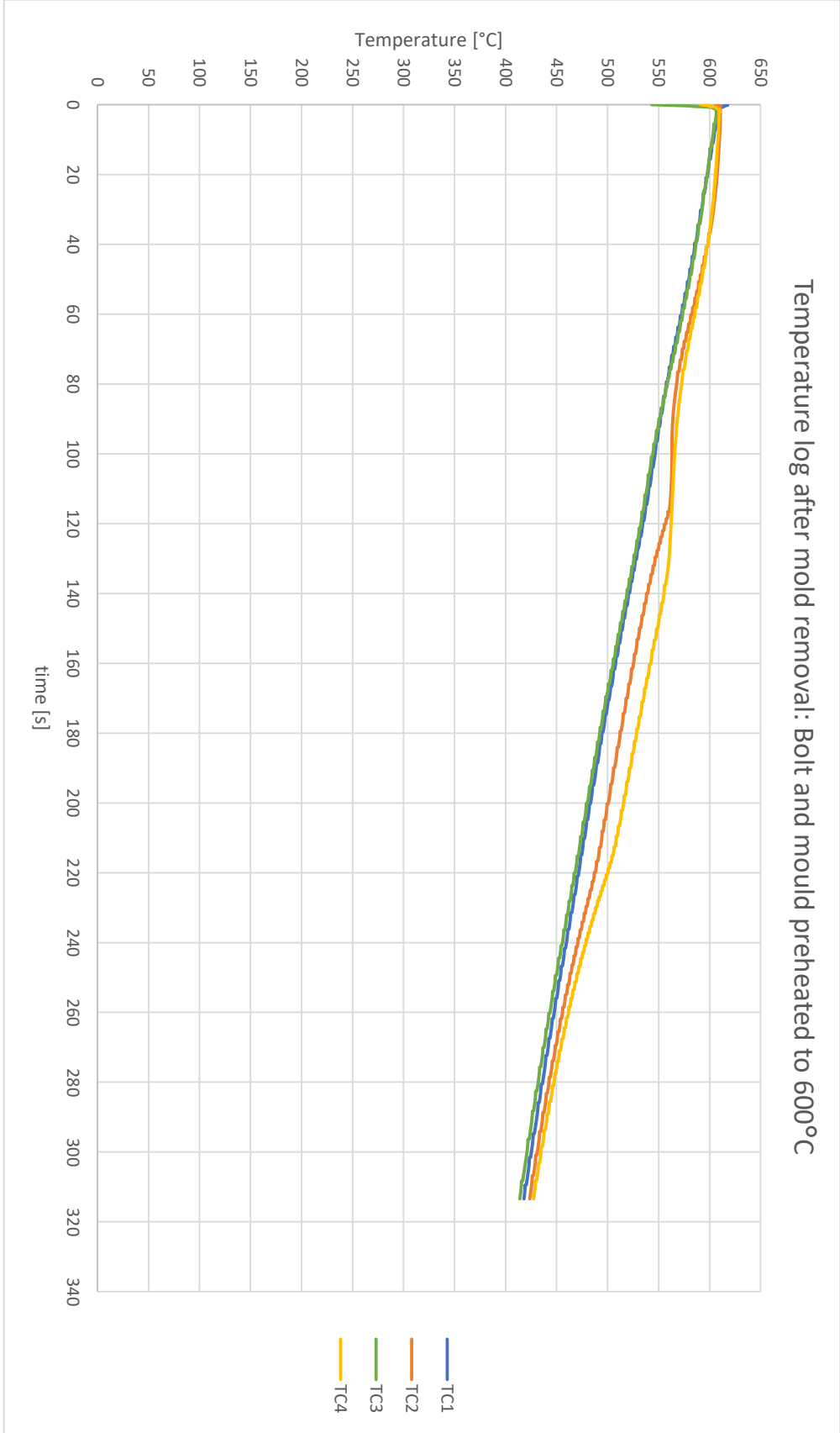


# Experiment 3, Series 1

Temperature log after mold removal: Pipe and mould preheated to 600°C



Experiment 3, Series 2

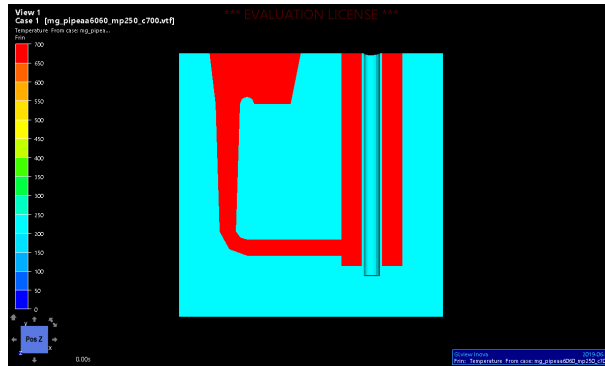


# Appendix D

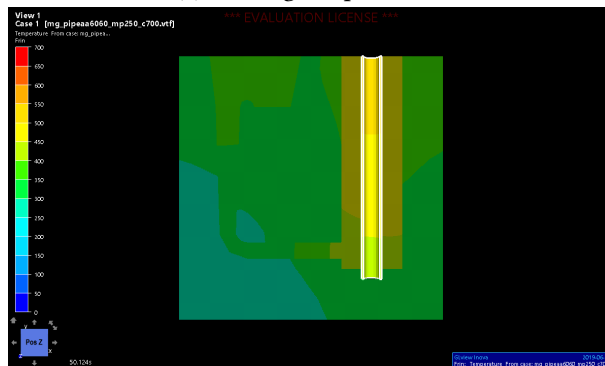
Results of simulation in StaMiSim are presented below.

## Experiment 1

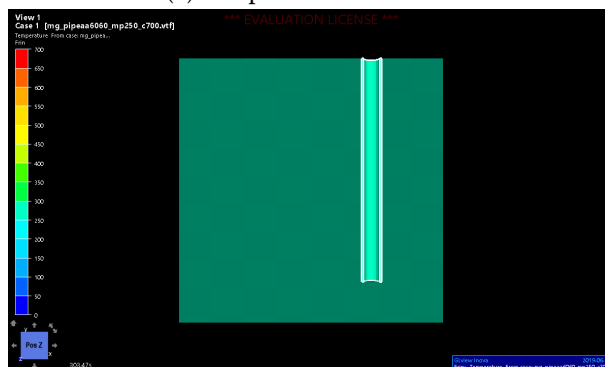
The temperatures were set to 250°C for the pipe and mould, and 700°C for the melt.



(a) Starting temperatures

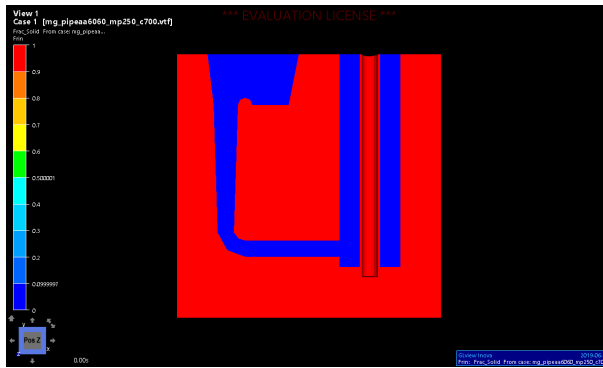


(b) Temperatures after 50 s

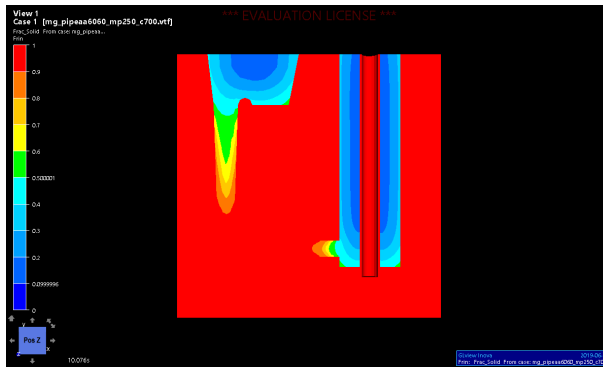


(c) Temperatures after 5 min

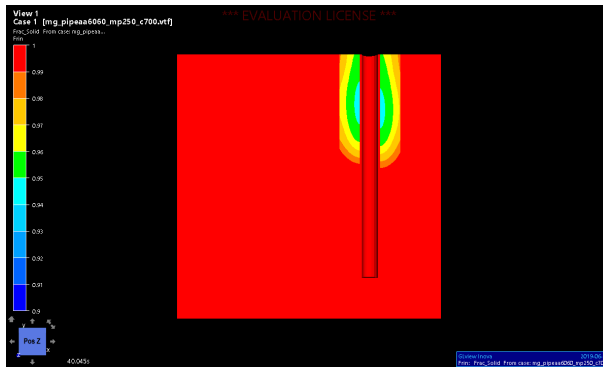
Temperature simulation for Experiment 1



(a) Solid fraction at the start



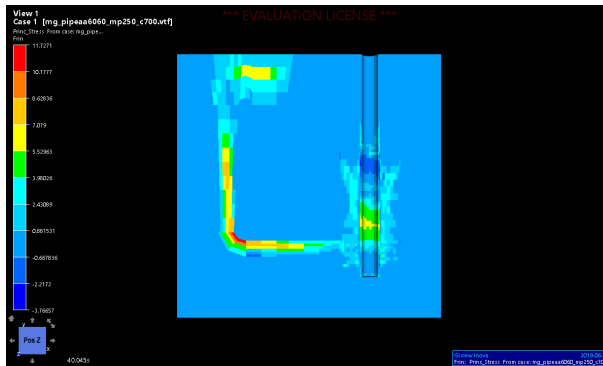
(b) Solid fraction after 10 s.



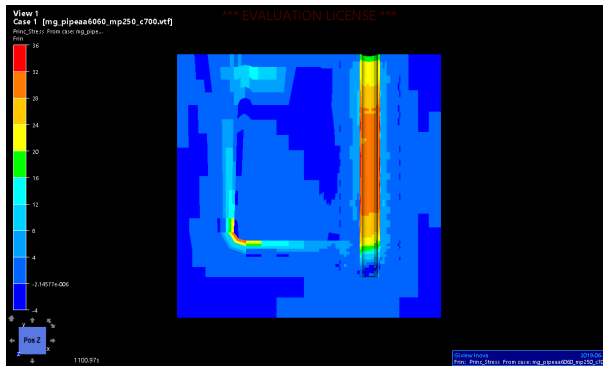
(c) Temperatures after 40 s.

Solid fraction simulation for Experiment 1

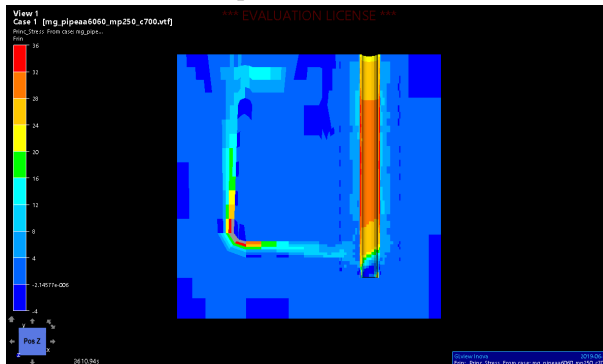




(a) Principal stress after 40 s

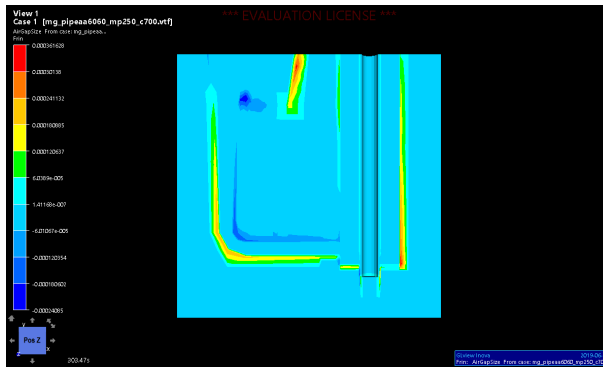


(b) Principal stress after 18 min.



(c) Principal stress after 60 min.

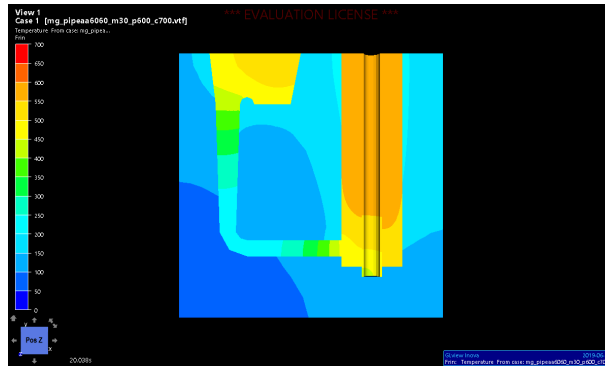
First principal stress simulation for Experiment 1



Air gaps formed after 5 min, simulated for Experiment 1

## Experiment 2, Series 1

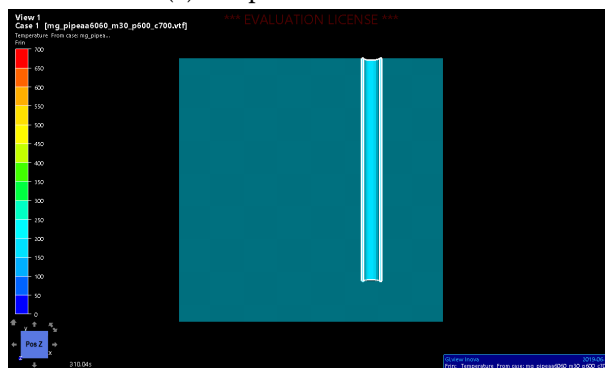
The temperatures were set to 600°C, 30°C and 700°C for the pipe, mould and melt respectively.



(a) Temperatures after 20 s

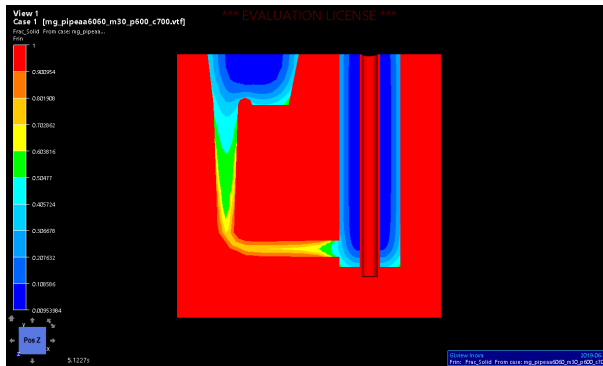


(b) Temperatures after 70 s

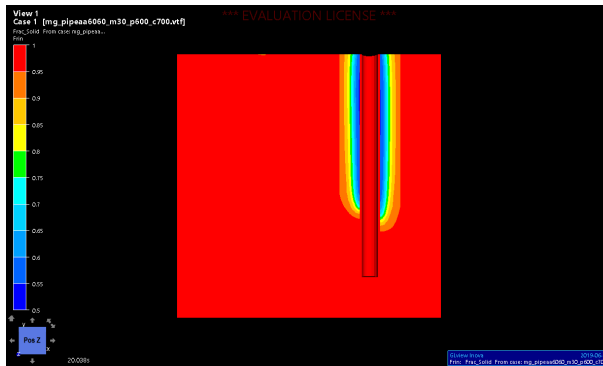


(c) Temperatures after 5 min

Temperature simulation for Series 2-1

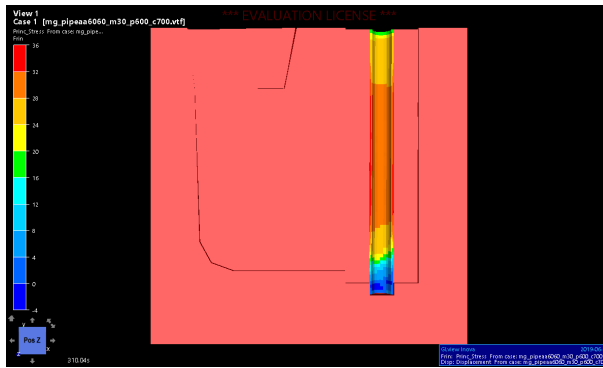


(a) Solid fraction after 5 s

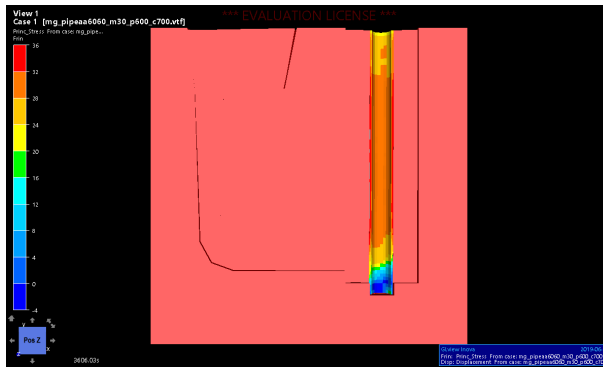


(b) Solid fraction after 20 s

Solid fraction simulation for Series 2-1



(a) Principal stress after 5 min

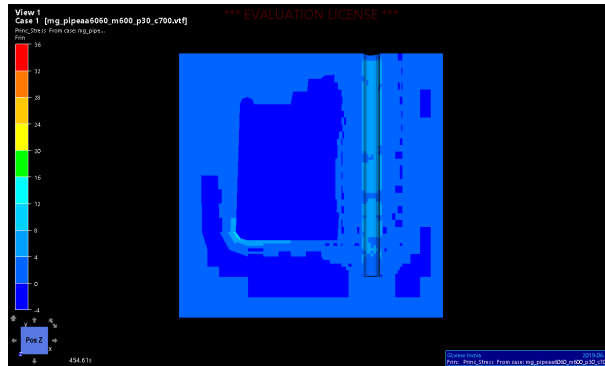


(b) Principal stress after 60 min

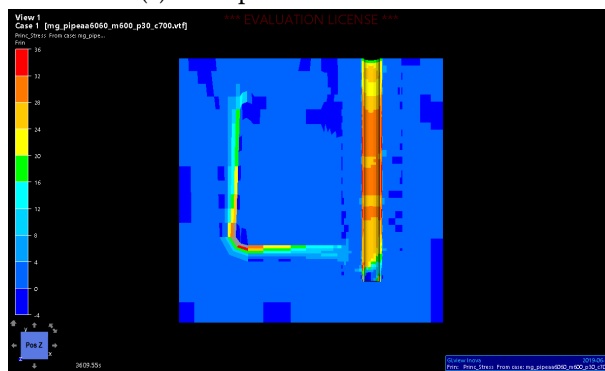
First principal stress simulation for Series 2-1

## Experiment 2, Series 2

The temperatures were set to 30°C, 600°C and 700°C for the pipe, mould and melt respectively.



(a) Principal stress after 7.5 min

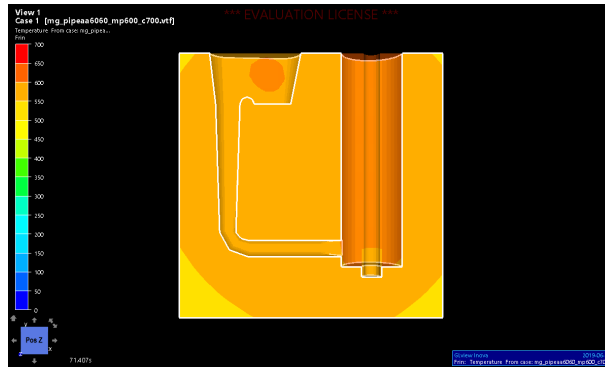


(b) Principal stress after 60 min

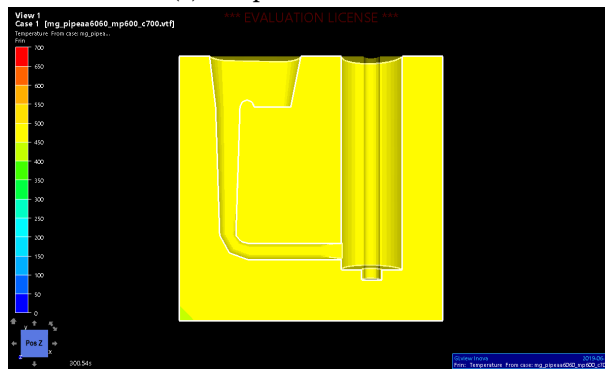
First principal stress simulation for Series 2-2

## Experiment 3, Series 1

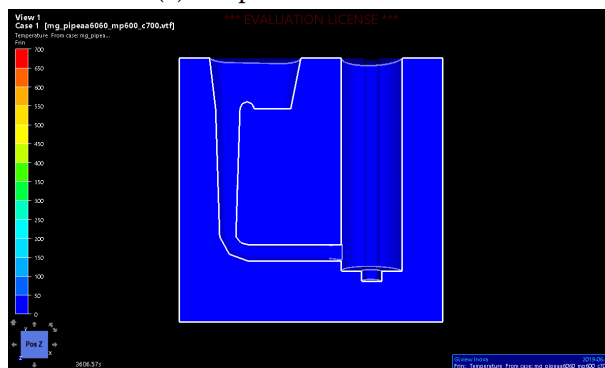
The temperatures were set to 600°C for the pipe and mould, and 700°C for the melt.



(a) Temperature after 70 s

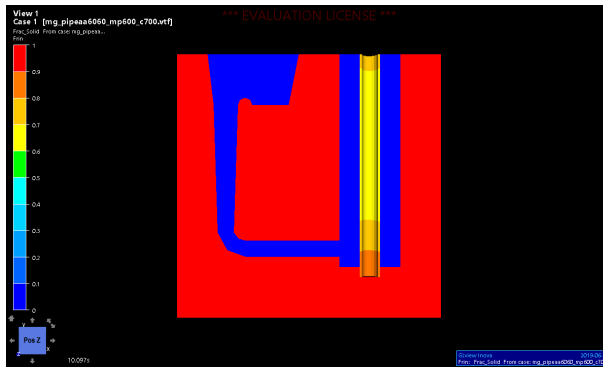


(b) Temperatures after 5 min

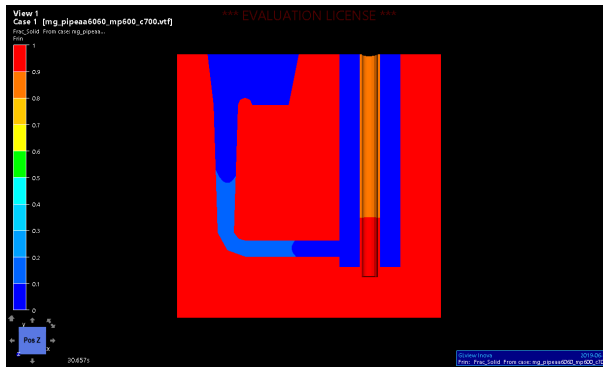


(c) Temperatures after 60 min

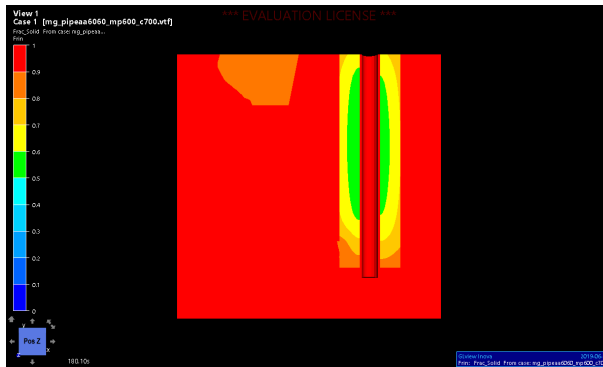
Temperature simulation for Series 3-1



(a) Solid fraction after 10 s



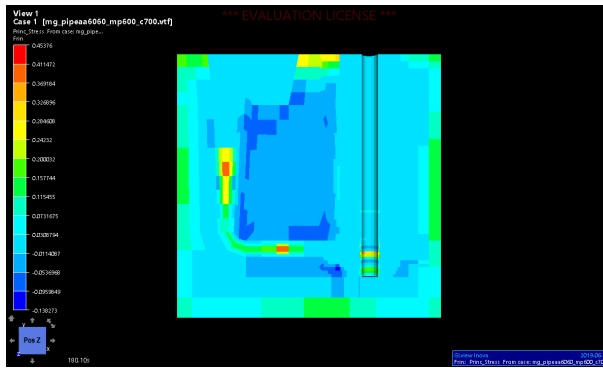
(b) Solid fraction after 30 s



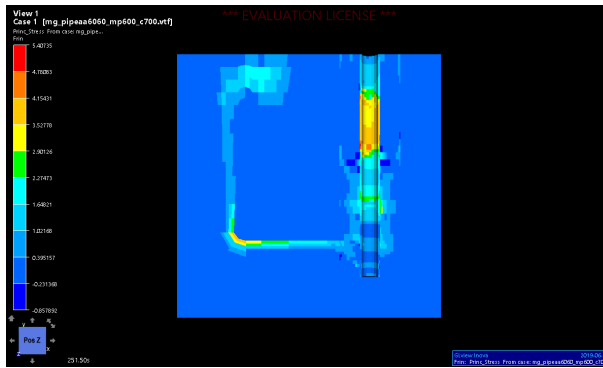
(c) Solid fraction after 3 min

Solid fraction simulation for Series 3-1

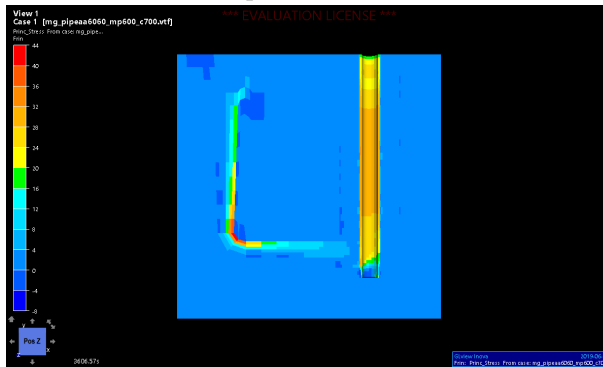




(a) Principal stress after 3 min

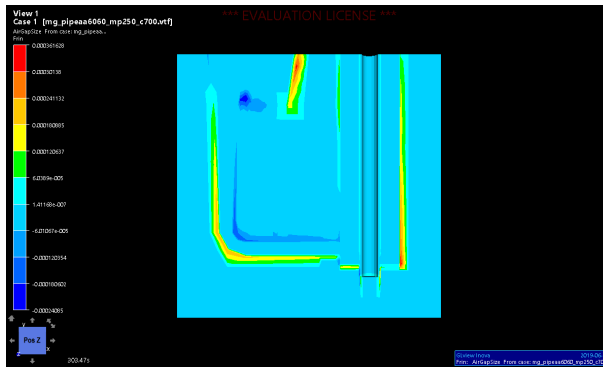


(b) Principal stress after 4 min



(c) Principal stress after 60 min

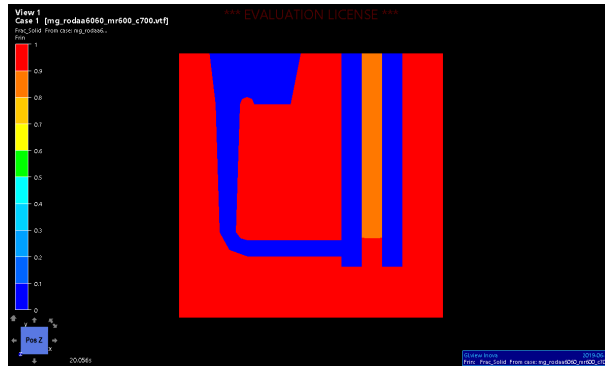
Principal stress simulation for Series 3-1



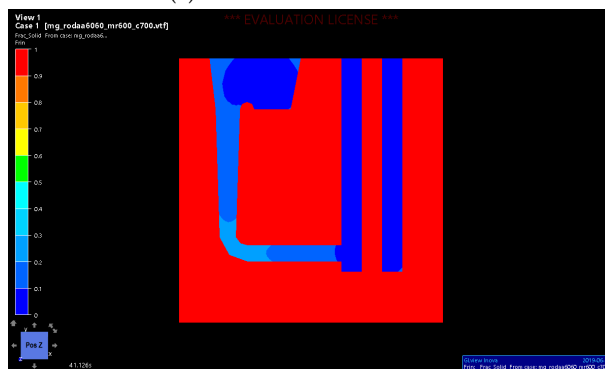
Air gaps formed after 5 min, simulated for Series 3-1

## Experiment 3, Series 2

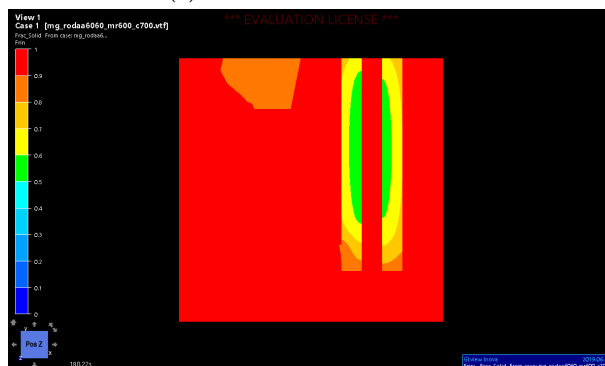
The temperatures were set to 600°C for the rod and mould, and 700°C for the melt.



(a) Solid fraction after 20 s

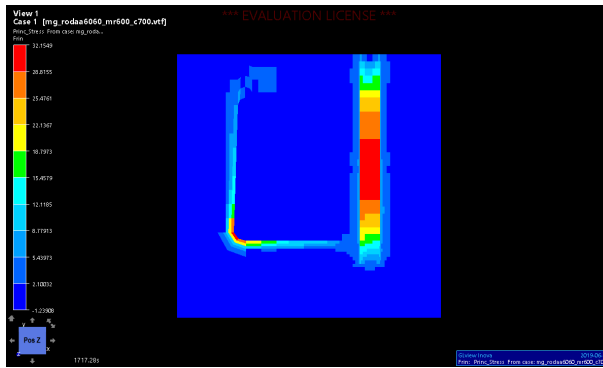


(b) Solid fraction after 41 s

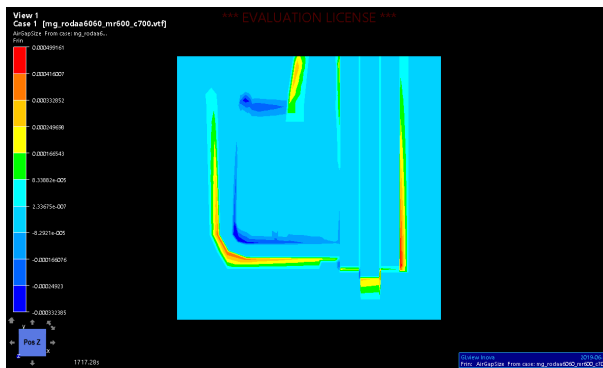


(c) Temperatures after 3 min

Solid fraction simulation for Series 3-2



First principal stress after 28.5 min, simulated for Series 3-2



Air gaps formed after 28.5 min, simulated for Series 3-2

